A Novel Optically Reconfigurable and Conformal Transmitarray

BY

MARCO D. POORT
B.S., California State University Chico, 2015
M.S., University of Illinois at Chicago, 2017

THESIS

Submitted as partial fulfillment of the requirements
for the degree of Doctor of Philosophy in Electrical and Computer Engineering
in the Graduate College of the
University of Illinois at Chicago, 2019

Chicago, Illinois

Defense Committee:

Piergiorgio L.E. Uslenghi, Chair and Advisor
Danilo Erricolo
Roberto D. Graglia, Politechnico di Torino
Vitali Metlushko
Daniel F. Sievenpiper, University of California San Diego
Michael Stroscio

ACKNOWLEDGMENTS

Thank you to my loving wife Nicole Sims, who supported and motivated me throughout my studies and who edited this work. To the rest of my family, especially my parents Elisabetta and Enrico who has always been there for me, and Lynne and Larry who 3D printed portions of the antenna. Also to my pups, Willow and Rowan, who were always there when I needed a break from writing or to take a walk.

I am especially grateful to my advisor, Prof. Piergiorgio Uslenghi, who made this academic journey possible and who has always provided insight and encouragement for this work. Thank you to my committee: Dr. Danilo Erricolo, Dr. Vitali Metlushko, Dr. Micheal Stroscio, Dr. Roberto Graglia, and Dr. Daniel Sievenpiper, who have served a major part in the completion of this dissertation through their feedback and mentorship.

I would like to thank my classmates and friends who were a source of knowledge and camaraderie throughout my studies. Lastly I would like to thank my numerous friends and mentors, particularly Dale Word, Nick McDonnell, and Jing Liang, who have played vital roles in my academic and professional opportunities.

This work is funded by the University of Illinois at Chicago Provost Research Award.

MP

TABLE OF CONTENTS

TABLE OF CONTENTS (Continued)

LIST OF TABLES

LIST OF FIGURES

LIST OF FIGURES (Continued)

FIGURE **PAGE**

LIST OF FIGURES (Continued)

FIGURE **PAGE**

LIST OF FIGURES (Continued)

FIGURE **PAGE**

LIST OF ABBREVIATIONS

$\overline{\overline{\epsilon}}$	Tensor Permittivity
ϵ_0	Vacuum Permittivity
η_0	Vacuum Impedance
$\overline{\overline{\eta}}$	Vector Impedance
λ_0	Free Space Wavelength
$\overline{\overline{\mu}}$	Tensor Permeability
μ_0	Vacuum Permeability
ω	Angular Frequency $= 2\pi f$
$\exp(+j\omega t)$	Time Dependance Omitted Throughout
I	Identity Matrix
$\Im(z)$	Imaginary Part of $z = x + jy$
j	Imaginary Unit $= \sqrt{-1}$
f	Frequency
$\Re(z)$	Real Part of $z = x + jy$
4G	Fourth Generation Cellular Network/Communications
5G	Fifth Generation Cellular Network/Communications
CGA	Compact Genetic Algorithm

LIST OF ABBREVIATIONS (Continued)

CSV	Comma-Separated Value Filetype
DC	Direct Current
HIS	High Impedance Surface
HFX	Magnetic Field Information Export from FEKO
FEM	Finite Element Method
FSS	Frequency Selective Surface
Gbps	Gigabit per second
GHz	Gigahertz
LOS	Line of Sight
LUA	LUA programming language
MRI	Magnetic Resonance Imaging
OT-MS	Optically Tunable Metasurface
MoM	Method of Moments
PEC	Perfect electrical conductor
PMC	Perfect magnetic conductor
RA	Reflectarray
RBW	Resolution Bandwidth
SAR	Synthetic Aperture Radar

LIST OF ABBREVIATIONS (Continued)

STAR	Simultaneous Transmit and Receive
SNR	Signal-to-Noise Ratio
TA	Transmitarray
THz	Terahertz
TIS	Tunable Impedance Surface
UIC	University of Illinois at Chicago
VNA	Vector Network Analyzer

SUMMARY

Reconfigurable antennas that can adapt to changes in their environment are gaining importance in a number of fields such as mobile communications, vehicular radar, and electromagnetic imaging. Beam steering antennas are one form of reconfigurable antenna that are becoming critical for advanced applications such 5G cellular networks because of their ability to target specific users which can increase signal to noise ratios and spectral recycling which will allow for more users to be reached with a broad band channels that increase connection speeds. 5G networks will also have access to a broader range of the electromagnetic spectrum than 4G networks because they will utilize the mm-wave frequency range which was previously not allocated for cellular systems.

A major downside to these mm-wave antennas is that they require a denser network of antennas, sometimes even with a direct line of sight to the target user. This may often not be feasible in environments such as historic places or parks where a large number of visible antennas may detract from the original purpose of the location and create aesthetic problems. Conformal antennas are a way to mitigate the aesthetic impacts of the antenna because it may be curved and hidden inside a structure already present in the existing surroundings. Conformal design can also be important in vehicular antennas, where drag is a concern, or security antennas, where the system may need to be low profile to avoid detection. This work aims to present a conformal beam-steering antenna which utilizes an optical switching method and heuristic design approach to allow for a flexible system that can be utilized in a wide number of applications.

The chapter on the theoretical design considerations examines the system model and the compact genetic algorithm that is used to design the antenna array patterns. Heuristic algorithms such as genetic algorithms require a model that accurately describes the overall system but can be rapidly computed such that multiple patterns may be rapidly iterated to find promising results. As such this work develops a simplified transmitarray model that stores critical values and computes pattern data using only standard matrix operations. This chapter also examines the compact genetic algorithm that is used in conjunction with this model to design antenna array patterns for this system.

The next chapter focuses on the physical realization of the system and demonstrates how most techniques for constructing the antenna. This chapter also demonstrates the optically tunable surface which is used to alter the transmitarray pattern and steer the main beam. This work shows the techniques to construct the horn antenna using a frame that is 3D printed and laser cut with light weight and low cost plastics that are then coated with copper tape to create the mechanical foundation of the structure. Lastly the system of designing optical masks that can be reliably projected onto the curved system is introduced in this chapter.

The final chapter presents an experimental validation of the system and extraction of several key parameters. First this chapter shows that the optically tunable surface may be utilized in a singly periodic fashion such as the current antenna and demonstrates that the antenna is still broadly tunable. The experiment also extracts antenna impedance measurements which are important for impedance matching systems. This chapter concludes by showing the systems ability to steer a radiation beam and create a connection with a narrow bandwidth to a remote target.

CHAPTER 1

INTRODUCTION

The demand for novel and dynamic antennas is growing as electromgnetic systems expand to an ever increasing number of applications and environments. Fields such as cellular communications and autonomous vehicles have grown rapidly over the past decades and are requiring a growing number of antennas spread throughout the globe. As these systems spread and become mobile, the antennas must be adapted to fit the diverse and changing needs of these systems. Conformal and reconfigurable antenna systems are designed to adapt to these changing environments and fit in a way that is unobtrusive and does not interfere with non-electromagnetic design considerations such as drag or visibility.

1.1 Summary of Conformal Antennas

A conformal antenna or array is defined as "an antenna that conforms to a surface whose shape is determined by considerations other than electromagnetic; for example, aerodynamic or hydrodynamic" [4]. The development of conformal antennas began in the 1930s with the study of circular arrays [5], which drew interest in direction finding and radar applications due to its relatively simple design and symmetry [6–8]. Conformal antennas began garnering large amounts of interest in the 1960s and 70s as aerospace applications demanded an ever increasing number of antennas without creating excessive drag. The topic even garnered a special issue of the *IEEE Transactions on Antennas and Propagation* in 1974 [9–14]. This field experienced a resurgence again in the early 2000's with several international workshops dedicated to the topic [15–18].

Conformal antennas fit into three main categories: single antennas, conformal radomes, and conformal arrays. Single antenna systems consist of one feed and radiator and are the simplest to implement. They are often utilized to fit electrically large antennas onto a structure such as planes or helicopters [19]. A variation of the single antenna is the conformal radome, in which a curved radome is placed over the antenna and designed with specific electromagnetic properties such as to filter unwanted radiation or focus the radiation pattern [20]. The last major group of conformal antennas are conformal arrays, in which multiple antennas are placed over a curved surface. These antenna arrays have been developed for a number of surfaces and applications such as satellite communications, where conformal arrays can increase the scanning range of the antenna system [21].

1.2 Summary of Reconfigurable Antennas

Most modern systems depend on reconfigurable antennas for applications such as beam steering, direction finding, and channel tuning. These dynamic systems are often altered through a number of electronic or electromechanical techniques such as PIN diodes, veractors, and microelectromechanical (MeM) switches in order to adapt to changing demands of various environments. Reconfigurable antennas can alter a number of parameters such as frequency, polarization, and radiation characteristics to improve system performance [22,23]. The ability to change parameters is very important in mobile systems where spectrum availability, data needs, and even the way a phone is held can dramatically affect the system.

Changing the frequency of an antenna is an important form of dynamic system that is used in cell communications. Frequency dynamic systems are critical in cell antennas because modern cellular communications must cover a wide range of the frequency spectrum that would be difficult and costly to design in a static antenna. The design difficulty is further compounded by the fact that cell phone antennas are usually electrically small and thus have a limited instantaneous bandwidth [24]. Frequency tuning is an important tool in antenna design to mitigate this bandwidth limitation because it allows the broadband frequency range to be separated into multiple tuning states that account for small portions of the overall required bandwidth [25]. The ability to tune the antenna among multiple possible channels also improves the system efficiency and performance as it allows a radio to select operating channels with the least amount of unwanted noise.

The next common form of reconfigurable antenna is a dynamic radiation pattern. Radiation patterns can be changed in a number of ways, the most common of which are beam and null steering. Altering an antenna pattern in either of these ways allow either a beam to be steered towards a desired target or a null to be steered to an unwanted noise source. Both of these methods improve the signal to noise ratio (SNR) of a system, which improves channel bandwidth and reliability. As the number of cell phones and other communications devices increase, so too does unwanted noise, which makes steering technology increasingly important in 5G and other future communications devices.

The final common form of dynamic antenna is polarization reconfigurable antennas. Polarization is becoming increasingly important as the frequency spectrum becomes more crowded.

The polarization states allow for an additional degree of freedom which may be used to encode data through polarization division duplexing (PDD) in Simultaneous Transmit and Receive (STAR) systems [26, 27]. However, PDD is difficult to achieve practically in mobile systems because obstacles and the way a device is held can alter the polarization of an antenna, creating interference between the polarization states. By altering polarization to account for these changes, the interference can be mitigated. Polarization tuning also mitigates polarization mismatch, which is a source of loss in wireless communications [28].

1.3 Applications of Reconfigurable and Conformal Antennas

Research in conformal and reconfigurable antennas has expanded as the uses for them have increased. The demand for these adaptable systems has been fueled by a number of new and growing fields such as vehicle antennas, cellular communications, and electromagnetic imaging. All of these fields need dynamic antennas that can adapt to an ever changing environment. The field of vehicle antennas is especially dependent on conformal antennas to reduce drag while other fields such as cellular communications and electromagnetic imaging benefit from conformal antennas to reduce visibility.

1.3.1 Vehicle Antennas

Many of the early developments in conformal antennas were developed for vehicle applications, particularly aircrafts where drag and stealth are central concerns. The number of antennas mounted to vehicles is also growing rapidly as antennas are required for communications, radar, and global positioning systems. This growth is expected to continue as autonomous and remote vehicles demand more complex mmWave radar systems and vehicle to vehicle com-

(a)

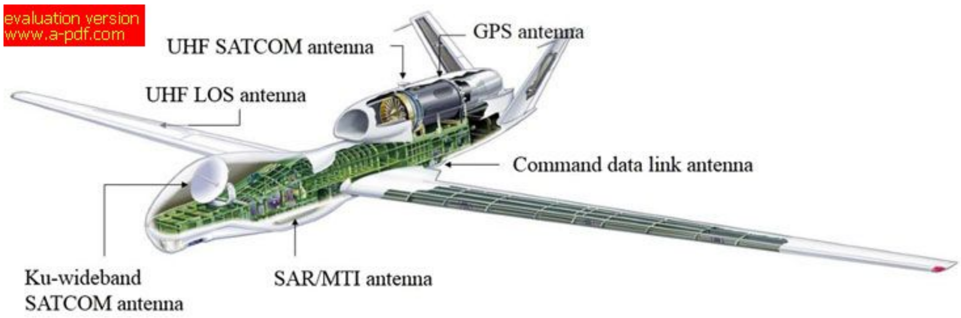

(b)

Figure 1. Vehicle antenna systems on (a) driverless cars [1], (b) military drones [2].

munications [1, 2]. These antennas are placed throughout the body of the vehicle as shown in Figure 1.

Vehicle antennas are designed for a wide range of frequencies from around 1000 kHz for simple AM antennas to 24 GHz for vehicle radar systems, and up to optical frequencies for Lidar systems. The multitude of radar and communications systems leads to a large number of antennas. An example of this phenomenon is found in most commercial aircrafts which carry dozens of antennas on the body of the plane [4]. If these antennas are not designed with aerodynamics in mind, they can create increased drag which leads to slower flights and increased fuel consumption.

1.3.2 Cellular Communications

Similar to how vehicular antennas drove much of the research in conformal antenna design, cellular communications have been a major focus of reconfigurable antenna systems. Both base station and cell phones antennas must be dynamic to adapt to hundreds or even thousands of users within a service area that can request cellular data. Cell phone antennas often use dynamic impedance matching because they need to operate in a number of conditions, such as on desks or near a user's head, which can change the antenna impedance and radiation pattern [25]. If the phone were not able to adapt to the changing conditions, it could lead to decreased data rate and dropped calls.

Dynamic impedance matching is also very important in cellular antennas because of the frequency range that they must cover. 5G communications systems use dozens of frequency bands ranging from 600 MHz up to 90 GHz and the antenna systems must be compact in order to fit into a usable cell phone size. Electrically small antennas face tradeoffs among size, bandwidth, and efficiency that makes designing for the broad range of frequencies with static impedance matching nearly impossible. Dynamic tuning mitigates the bandwidth limitations by tuning the antenna to a needed frequency band, rather than the entire spectrum.

5G communications rely heavily on beam steering arrays and multiple input multiple output (MIMO) systems to further improve data rates and phone performance. These pattern reconfigurable systems can adapt to noisy environments and find configurations to increase the strength of the signal while canceling unwanted noise. At high frequencies above 6 GHz, narrow radiation beams with relatively large bandwidths can be steered by base station antennas to create strong connections between the cell and a nearby user with extremely high Gigabit per second (Gbps) data rates. These high frequency signals are highly attenuated in the earths atmosphere, meaning that some base stations can require line of sight (LOS) or near LOS paths between the station and the user. A large number of cell towers placed in visible areas can be obtrusive and may slow the adoption of new cellular networks in places such as museums or parks where the asthetics of the location must be preserved. Adapting an antenna system to conform to an environment allows the system to be easily concealed, meaningthat more antennas can spread throughout an environment to improve network performance and user experience.

1.3.3 Electromagnetic Imaging and Sensing

Electromagnetic imaging as a field benefits from pattern reconfigurable antenna systems and increased computational power, which allows for scatterers to be identified in a manner that is remote and unobtrusive. One of the earliest major uses of electromagnetic imaging was magnetic resonance imaging (MRI) which mechanically scans antennas around a patient and uses the varying field data to take internal images [29]. As computing power has improved, electromagnetic systems are also being developed for real time applications such as gesture recogniztion or remote imaging [30, 31]. Remote imaging has also become more precise with the introduction of mm wave technologies for airport and homeland security.

Electronic pattern switching methods have been introduced to synthetic aperture radar (SAR) systems because they are able to create a large variety of patterns faster than a mechanical steering method would. Scattering information from these multiple patterns is then used to compute the locations and sizes of scatterers in the radars field of view [32]. Another major benefit of electronic pattern diversity is that the absence of moving parts makes the antenna system easier to conceal in an urban environment or consumer electronics. This concealability can be further improved by conformal antennas which would allow SAR systems to be placed on car bodies or other objects with complex shapes.

1.4 System Overview

The work in this dissertation demonstrates the feasibility of a system that combines the benefits of a reconfigurable and conformal antenna system, using a novel optcal tuning method. This antenna design utilizes a compact genetic algorithm (CGA) to determine the antenna configuration pattern in a way that can readily be adapted to new shapes and design requirements. The physical antenna is altered using an optically tunable surface which removes the need to run multiple feed lines along the surface that could harm the system efficiency and radiation pattern. An example of the proposed system is shown in Figure 2 to demonstrate the potential integration of the conformal antenna into a system.

The body of the antenna system consists of a cavity which is placed inside a larger structure such as a car or building. The edge of the cavity that is along the exterior wall of the structure is covered with a flexible optically tunable metasurface that is curved to match the shape of the outer wall. The cavity is excited by a radio frequency (RF) feed source and a projector is placed on the back side of the cavity to select which portions of the surface will radiate. This optical tunability allows a computer or microcontroller to control the radiation pattern and adjust the antenna to steer a radiation beam or scan multiple patterns. This versatile and unobtrusive design may find a number of uses in fields that utilize antennas such as those detailed in section 1.3.

1.4.1 Summary of Chapters

The details of the designed antenna system are described in four major chapters. Chapter 2 provides a literature review of foundational concepts for the system design. Chapter 3 develops the theoretical foundation behind the antenna system, including the methods of modeling the antenna and the CGA that is used to configure the system. Chapter 4 details the physical construction of a working prototype and the optically tunable surface that forms the foundation of this system. Lastly, chapter 5 details several tests carried out on the antenna system to confirm that the system is tunable and can be used for beam steering applications.

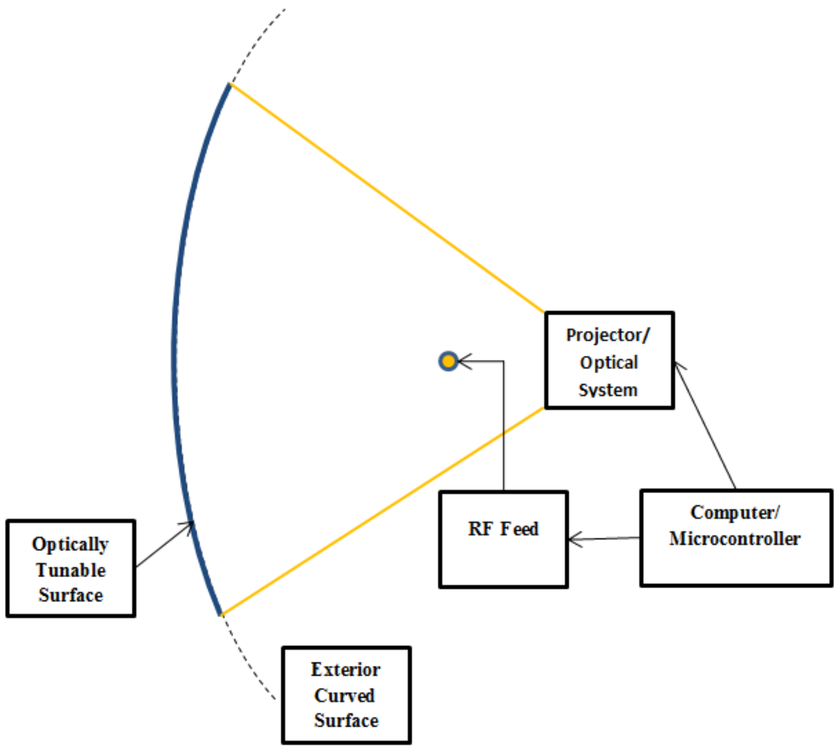

Figure 2. Overview of proposed antenna design.

CHAPTER 2

FUNDAMENTAL CONCEPTS OF RECONFIGURABLE TRANSMITARRAYS

2.1 Antenna Arrays

The design of the pattern reconfigurable antenna requires a working knowledge of antenna array design. A phased antenna array consists of a number of individual antennas or elements placed over a space and excited with varying amplitudes and phases. The individual antenna patterns then interfere constructively and destructively to alter the total far field radiation pattern. Phased antenna arrays have a wide number of benefits which include an increased gain with respect to an individual radiator and the ability to steer the main lobe of the radiation pattern towards a desired target. These benefits are important in antenna design and because of them phased arrays are utilized in numerous applications including but not limited to radio astronomy, cell phone towers, and radar systems.

For an array with N equal elements with the n^{th} element located at the the spherical coordinate (r_n, θ_n, ϕ_n) and excited with amplitude A_n, the array factor for the antenna in the far field may be calculated through the equation

$$AF(\theta, \phi) = \sum_{n=0}^{N-1} A_n e^{-jkr_n(\sin\theta \sin\theta_n \cos(\phi - \phi_n) + \cos\theta \cos\theta_n)}, \tag{2.1}$$

where $k = 2\pi/\lambda_0$ is the wavenumber in free space. If all the antenna elements are identical with a far field pattern $G(\theta, \phi)$, the total radiation pattern $F(\theta, \phi)$ for the system is then found through simple multiplication as

$$F(\theta, \phi) = G(\theta, \phi) AF(\theta, \phi) \tag{2.2}$$

Often times only the plane $z = Constant$ is considered for simplicity and in this case the array factor may be simplified using $\theta = \theta_n = \pi/2$ to

$$AF(\phi) = \sum_{n=1}^{N} A_n e^{-jkr_n \cos(\phi - \phi_n)}. \tag{2.3}$$

One of the earliest applications of phased arrays and a demonstration of their utility is to place all of the elements along a line with an even spacing Δr and exciting them with an even magnitude and progressive phase $\Delta\phi$. For this case, the key variables become $r_n = (n-1)\Delta r$, $\phi_n = 0$, and $A_n = e^{j(n-1)\Delta\phi}$. With these variables, Equation 2.3 becomes

$$AF(\phi) = \sum_{n=0}^{N-1} e^{jn(\Delta\phi - 2\pi\frac{\Delta r}{\lambda_0}\cos\phi)} = \frac{1 - e^{jN(\Delta\phi - 2\pi\frac{\Delta r}{\lambda_0}\cos\phi)}}{1 - e^{j(\Delta\phi - 2\pi\frac{\Delta r}{\lambda_0}\cos\phi)}}. \tag{2.4}$$

This equation then simplifies to

$$AF(\phi) = e^{\frac{jN}{2}(\Delta\phi - 2\pi\frac{\Delta r}{\lambda_0}\cos\phi)} \frac{\sin(\frac{N}{2}(\Delta\phi - 2\pi\frac{\Delta r}{\lambda_0}\cos\phi))}{\sin(\frac{1}{2}(\Delta\phi - 2\pi\frac{\Delta r}{\lambda_0}\cos\phi))}. \tag{2.5}$$

If all the elements of the array are isotropic elements (i.e. $G(\phi) = 1$), the radiation pattern of the total system has a maximum magnitude of N at $2\pi\frac{\Delta r}{\lambda_0}\cos\phi = \Delta\phi + 2\pi k$ where k is an integer. Therefore, the normalized pattern $f(\phi)$ may be written as

$$f(\phi) = \frac{\sin(\frac{N}{2}(2\pi\frac{\Delta r}{\lambda_0}\cos\phi - \Delta\phi))}{N\sin(\frac{1}{2}(2\pi\frac{\Delta r}{\lambda_0}\cos\phi - \Delta\phi))}. \tag{2.6}$$

This simple example shows the key benefits of a phased array system. Plots for variations of the key variables and their effects are shown in Figure 3 with only the angles $0 < \phi < 180°$ shown due to the symmetry of the pattern. The main beam may be made more narrow and thus increase the directivity by increasing either the variables N or Δr. It should be noted that if spacing $r > \lambda_0/2$ is used, then the equation $2\pi\frac{\Delta r}{\lambda_0}\cos\phi = \Delta\phi + 2\pi k$ may gain additional solutions within the range $0 < \phi < 2\pi$. This spacing results in additional beams known as grating lobes which appear in the radiation pattern and have equal magnitudes as the main beam. The main beam can also be steered to have a maximum radiated power at different values of ϕ by changing the parameter $\Delta\phi$.

Further patterns may be obtained by using unevenly excited or spaced elements. These additional degrees of freedom may be utilized to optimize a number of additional design parameters other than the main beam width and direction. Examples of this optimization include using unevenly spaced elements to reduce side lobe levels or weighting the elements to steer a null in the pattern to reject a source of interference [33, 34].

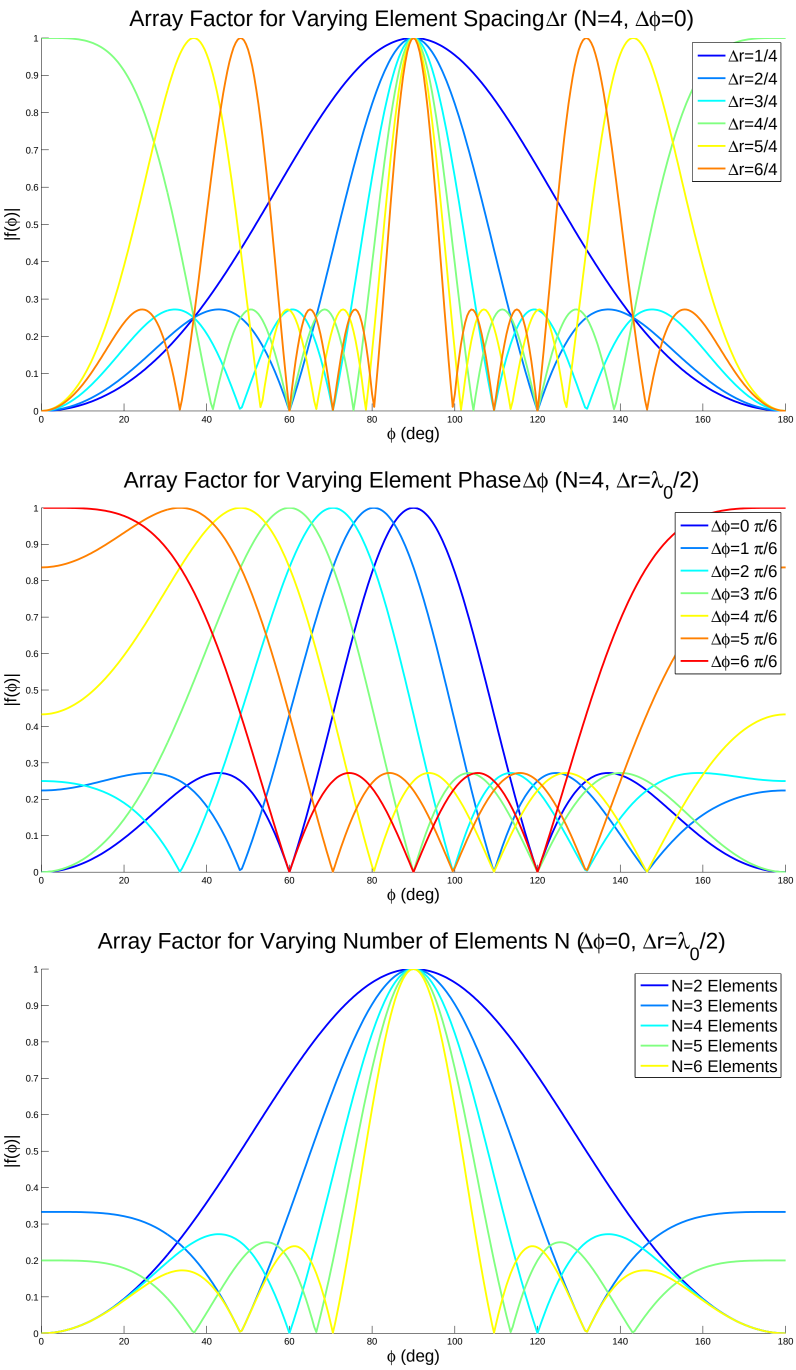

Figure 3. Array factor for varying parameters of a uniformly excited and equally spaced linear array.

2.1.1 Transmitarrays

Transmitarrays (TA) are a subset of antenna arrays that have gained popularity in recent years due to advances in metasurface design. In these arrays, a surface is illuminated by one or more feed sources and the surface is patterned to modulate this incident field into the desired radiation pattern. This form of antenna array is often ideal for a single feed source and may be implemented without complex phase shifters. An example of how a TA may be realized physically is shown in Figure 4.

For design purposes, the feed horn is placed at a sufficiently large distance from the surface such that the incident waves on the surface are nearly planar and the far field pattern of the horn may be used for the incident field pattern. A common field approximation to use for the horn is the pattern

$$F_{FS}(r,\theta,\phi) = \frac{e^{-jkr}}{kr}\frac{n+1}{2\pi}\cos^n(\theta), \tag{2.7}$$

where the integer n is selected based on the particular horn antenna used. Computational solvers, however, may be used for more complex systems or systems where the feed is near the surface of the TA. Assuming that the antenna elements are sufficiently uniform with a far field pattern $g(\theta,\phi)$, the radiation pattern for the TA may then be computed through

$$F(\theta,\phi) = g(\theta,\phi)\sum_{i=1}^{N} F_{FS}(r_i,\theta_i,\phi_i)G_i e^{-jkr_i(\sin\theta\sin\theta_i\cos(\phi-\phi_i)+\cos\theta\cos\theta_i)}, \tag{2.8}$$

where G_i is the gain associated with the i^{th} element. For simple surfaces, G_i may be simply a function of the direction of incidence of the incident wave. Alternatively, the surface may

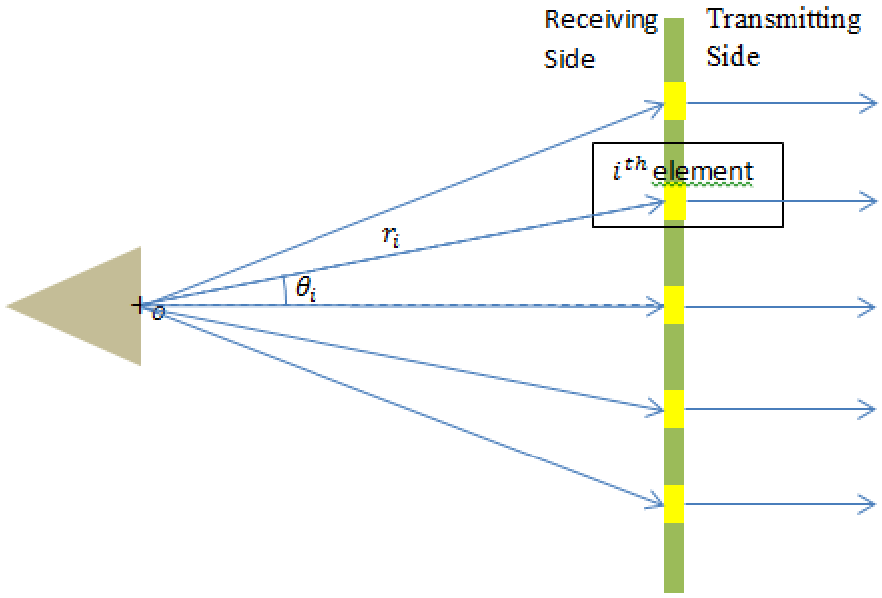

Figure 4. Simple view of a transmitarray.

be designed with non-uniform elements in order to modulate the behavior of G_i and obtain a desired pattern. For reconfigurable surfaces, the gain and phase of G_i may also be altered in order to vary the antenna pattern.

One additional parameter which must be accounted for in arrays generally and particularly for transmitarrays, is the mutual coupling between two adjacent elements. For aperture antennas such as gaps or surfaces without additional coupling through the feeding structure, the mutual coupling may be modeled through calculated parameters. The coupling between elements i and j is calculated through

$$Y_{i,j} = \frac{1}{V_i V_j} \int_{S_i} \overline{E}_i \times \overline{H}_i(\overline{E}_j) d\overline{S_i}, \tag{2.9}$$

where S_i is the i^{th} aperture, $\overline{E}_i$ is the electric field over the aperture i, $\overline{H}_i(\overline{E}_j)$ is the magnetic field induced on the aperture i due to the excitation of aperture j, and $V_{i,j}$ are modal amplitudes which equal 1 when normalized [35]. Generally, these fields are too cumbersome to calculate analytically and as a result are computed using a computational solver.

Once the fields are obtained, Equation 2.9 is used to populate the admittance matrix Y which may be used to calculate the scattering matrix S through

$$S = (I - Y)(I + Y)^{-1}. \tag{2.10}$$

This scattering matrix is then linked to the mutual coupling between two elements ($C_{i,j}$) through the relationship

$$C_{i,j} = 20 \log |S_{i,j}|. \tag{2.11}$$

This mutual coupling must be accounted for in order to find the exact radiation pattern, particularly if elements are placed close together. However, a number of techniques and designs may be used to mitigate this coupling effect [36].

2.2 Conformal Antenna Design

In addition to planar antennas and arrays, it is also possible to realize conformal systems, designed to follow a desired curvature. These types of antennas are of particular interest in aeronautical and vehicular applications because otherwise the antenna may lead to increased drag or act as an unwanted scatterer. In the most three-dimensional cases, these surfaces are doubly curved such as in the case of a sphere or cone. For a number of applications such as airline fuselages, singly curved surfaces such as cylinders can be used to reduce the design complexity. Matching an antenna or array to a curved surface may however introduce a number of additional complexities to the antenna design.

One key factor when designing arrays on a conformal surface is that the elements may have a non-uniform pattern due to different scattering interactions between the antenna and the surface as well as different orientations when the elements are mounted on the surface. This variety of patterns has a significant effect on the total radiation pattern, since the total pattern may no longer be obtained through simply multiplying the array factor and the element factor. The new antenna pattern is then calculated through the equation

$$F(r,\theta,\phi) = \sum_{i=1}^{N} g_i(\theta,\phi) e^{-jkr_i(\sin\theta\sin\theta_i\cos(\phi-\phi_i)+\cos\theta\cos\theta_i)}, \tag{2.12}$$

where g_i is the radiation pattern associated with the i^{th} element.

This varying pattern factor is particularly important for gap fed antennas. These gap elements are useful for conformal antennas because they can be easily spread over a surface, but they are often directional and point toward the unit normal to the surface where they are placed. This directional pattern creates a number of trade-offs. The directionality these gaps can be very useful in steering the beam over a wider scan region if the surface is suitably curved. The effective aperture however is greatly reduced due to elements not being useful if they are not pointing in the desired direction. The former benefit outweighs the costs for antenna designs such as the ones presented in this dissertation which emphasize versatility and re-configurability, but in order to realize this benefit a good model must be developed for the pattern of the radiating element and also for the magnitude with which it is excited. More details will be presented in the design specifications given in section 3.1.

2.3 Pattern Synthesis

Pattern synthesis is a common problem in antenna design in which the designer wishes to best approximate a desired radiation pattern with a given set of constraints, such as bandwidth or antenna dimensions. This issue is important for antenna designers because antennas can be useful in a wide range of environments. These environments and applications require any number of different radiation patterns which may radiate a signal towards a number of different targets or have a radiation pattern which avoids jamming from an unwanted noise source. The most commmon cases of pattern synthesis aim to approximate an arbitrary pattern using methods such as those developed by Rhodes or Cheng et. al. [37, 38]. These methods lead to analytical results, but are limited to few cases, such as when the radiator is a line source or a prolate spheroid. Further methods have since been employed to tackle increasingly complex sets of radiation patterns and radiating bodies.

One of the most common problems in pattern synthesis are related to geosynchronous satellite reflector antennas where an ideal pattern covers only a section of the earth such as a single continent [39]. The satellite orbit then allows for a signal to be transmitted only over the desired coverage area without wasting power or generating noise over unwanted regions such as oceans. Pattern synthesis approaches that use these more complex structures and patterns require more complex models which can sometimes be solved analytically, but are also being approached using heuristic methods such as genetic or social network algorithms, which will be discussed in a later section [40].

The introduction of reconfigurable surfaces and elements to these reflectarray systems has increased the interest in heuristic methods because dynamic systems are often more constrained due to the nature of the unit cells or the tunability of the structure. The heuristic methods also require a larger number of patterns to be computed since the system is dynamic in nature. Furthermre, these heuristic methods are preferred because they can rapidly be adapted to new designs by simply altering the cost function. The consequence of heuristic methods is that they require a large number of computations which can potentially be time consuming and costly.

Both analytical and heuristic approaches often consider simplified models for obtaining results. The simplified or analytic models are required for the necessary mathematical operations to reach meaningful results, whereas the simplified models for heuristic methods are necessary in order to reduce the computational cost. Using simplified models of electromagnetic systems may, however, introduce inaccuracies to the optimization method. For this reason electromagnetic optimization methods often need to be carried out in conjunction with and verified through full wave simulations or experiments.

2.3.1 Beam Steering

Beam steering and beam forming are a major subset of pattern synthesis in which a narrow radiation pattern is steered towards a desired target. Beam steering is ideal because it focuses a strong signal towards only a desired target without wasting excess power or generating noise in undesirable directions. Beam forming began to excite research in the early $20^{\mathbf{th}}$ century for use in radar systems. This research led to the pivotal work of W.W. Hansen and J.R. Woodyard which continues to be prevalent in the teaching of antenna analysis [41].

Beam steering is often desirable for a wide range of antenna applications such as radar systems, satellite communications, and 5G cell towers. Beam steering is becoming increasingly attractive in micro and mm-wave systems where high gain antennas can be realized in relatively small systems. This high gain may also be critical in order to transmit the signal between two points using a reasonable amount of power, despite high attenuation rates in micro and mm-wave propagation.

In these high frequency ranges, traditional phased array systems which require multiple feeding systems may be costly, which has led to a wide range of research into novel methods of antenna switching to find more cost effective solutions for the process. One of these methods is to switch the feed point of a Rotman lense antenna [42, 43], which has the benefit of being relatively simple to steer and low loss, but is also limited in that it can only provide a discrete number of target directions based on the number and complexity of the feeds used.

Another common design technique is to utilize a leaky wave antenna with gaps or discontinuities along a waveguide surface. A number of steering methods have been designed for these systems. One of them utilizes variations in the source frequency to steer the main beam of a leaky wave antenna based on the frequency of the transmitted field [44]. This method is especially useful for high frequency radar applications because it is able to convert angle of arrival information to the spectral domain. This application is less ideal for a communications antenna because target angle and channel information are not necessarily related. Additional beam steering methods have been developed for surface and leaky wave systems that utilize variations in a tunable surface to alter the radiation pattern. These variations may be tuned either electrically or mechanically in order to vary the radiation direction of the main beam [45, 46]. These surface wave systems have the benefit of a low profile and can be mounted on planar systems, but they are often highly lossy or suffer from a low effective aperture.

Transmit or reflectarrays (RA) are also common for beam steering applications. RA antennas consist of two key components, a feeding antenna such as a simple horn antenna, and a surface which reflects the incident field resulting from the feed antenna. RAs are especially common in satellite dish antennas because they are relatively easy to design and deploy and drag is not a concern so the feed element can be placed in front of the surface. The deployability in satellite applications can further be improved by folding the antenna for launch and then deploying the antenna once the satellite is in orbit [47]. The surfaces are then designed to maximize directivity or obtain a desired radiation pattern that may then be modulated using similar methods to those employed in leaky wave systems to alter the direction of the main beam of the radiation pattern [48].

Transmitarrays (TA) are similar to RAs in that the system consists of a feed antenna and modulating surface, but TAs are often more useful for applications where drag is a concern because the feeding antenna may be located behind the surface to further reduce the drag of the antenna. The ability to conceal the feed structure may also be preferred in applications where the antenna needs to be concealed or contained within a structure. The downside of these antennas is that unit cells may be harder to design because they must allow the wave to pass through the surface, which often requires a larger unit cell size than an RA surface which simply needs to reflect the field. Similar to reflectarrays these surfaces offer a wide range of freedom in designing desired radiation patterns and can be tuned mechanically or electronically [49]. More details on the theory behind RA and TA antennas are found in sec. 2.1.

2.4 Summary of Metasurfaces and Metamaterials

Many recent designs of reconfigurable TA or RA antennas utilize modern advances in reconfigurable metasurfaces or metamaterials in order to change the electrical characteristics of the antenna surface or structure. These tunable surfaces or materials begin with a conventional metasurface design such as a frequency selective surface (FSS) or high impedance surface (HIS) and as such it is important to analyze some of these structures before proceeding with the tunable surface design.

Metamaterials are any structure with a three-dimensional periodicity which is much smaller than the wavelength of the electromagnetic field. These unit cells may take on a wide variety of forms, including but not limited to, ring resonators or fishnet structures [50, 51]. This small periodicity of the structure, however, allows for the material to then be utilized in larger applications as if it were a normal bulk material and analyzed with Mawell's equations in a bulk material without imposing additional boundary conditions:

$$\nabla \cdot \overline{E} = 0, \tag{2.13}$$

$$\nabla \cdot \overline{H} = 0, \tag{2.14}$$

$$\nabla \times \overline{E} = -j\omega\overline{\overline{\mu}}(\omega)\overline{H}, \tag{2.15}$$

$$\nabla \times \overline{H} = j\omega\overline{\overline{\epsilon}}(\omega)\overline{E}. \tag{2.16}$$

These materials, however, allow for a wide range of properties not usually found in nature, such as a double negative refractive index [52].

Metasurfaces are often considered to be the two-dimensional version of metamaterials and are classified as an array of two-dimensionally periodic unit cells where the periodicity and the thickness are electrically small compared to the frequency of interest. As with the case of metamaterials, the electrically small nature of the unit cells and the thin nature of the structure allow for various mathematical simplifications to be made. Generally, the surfaces can be modeled through sheet impedance boundary condition

$$\hat{n} \times (\overline{H}_1 - \overline{H}_2) = \frac{1}{2}\overline{\overline{\eta}}(\omega) \cdot (\overline{E}_1 + \overline{E}_2), \tag{2.17}$$

where $\hat{n}$ is the outward facing unit normal of the surface, the subscript 1 denotes the fields outside of the surface, and the subscript 2 denotes the fields inside the surface.

For analysis, most metasurfaces can be categorized into either metafilms or metascreens [53]. Metascreens consist of an array of gaps in an otherwise reflective surface such as a metal sheet. This type of surface is often easy to fabricate and as such has seen a wide range of applications such as parabolic dish reflectors where the small gaps reduce the force on the surface due to wind or on microwave oven doors where the perforations are sized to allow light to pass through but remain reflective at 2.4 GHz [54].

The complement to the metascreen is the metafilm, which consists of a periodic array of reflective structures over an otherwise translucent surface such as a thin dielectric substrate or film. Many common frequency selective surfaces (FSS) such as Jerusalem crosses or patch arrays fall in this category [55]. These FSS's are designed to be translucent at a desired frequency range while reflecting unwanted signals.

These frequency selective surfaces are often used as the basis for tunable metasurfaces of which the surfaces may be tuned or detuned in a variety of ways, including but not limited to, biasing a nonlinear components [56], reconfiguring MEMS switches [57], or altering material properties with an optical source [58]. These surfaces are gaining popularity in reconfigurable antennas due to their ability to rapidly alter an antenna resonance or pattern.

2.4.1 Tunable High Impedance Surfaces

A large body of work on tunable high impedance surfaces (HIS) and their applications in reconfigurable antenna design has been generated by Daniel Sievenpiper, stemming from a corrugated surface that is shown in Figure 5 and Figure 6 [3]. One of the key properties of a HIS is that it reflects an incident electromagnetic field in such a way that the reflected wave interferes constructively with the incident field (i.e. is in phase) on the surface. An ideal HIS where the reflected field is perfectly in phase with the incident field and of the same magnitude can be mathematically modeled as a perfect magnetic conductor (PMC), which is the dual of a perfect electrical conductor (PEC) surface which reflects a wave that interferes destructively (i.e. out of phase) on the PEC surface. HISs such as the corrugated surface have a number of potential benefits including bandwidth and efficiency improvements for electrically small antennas.

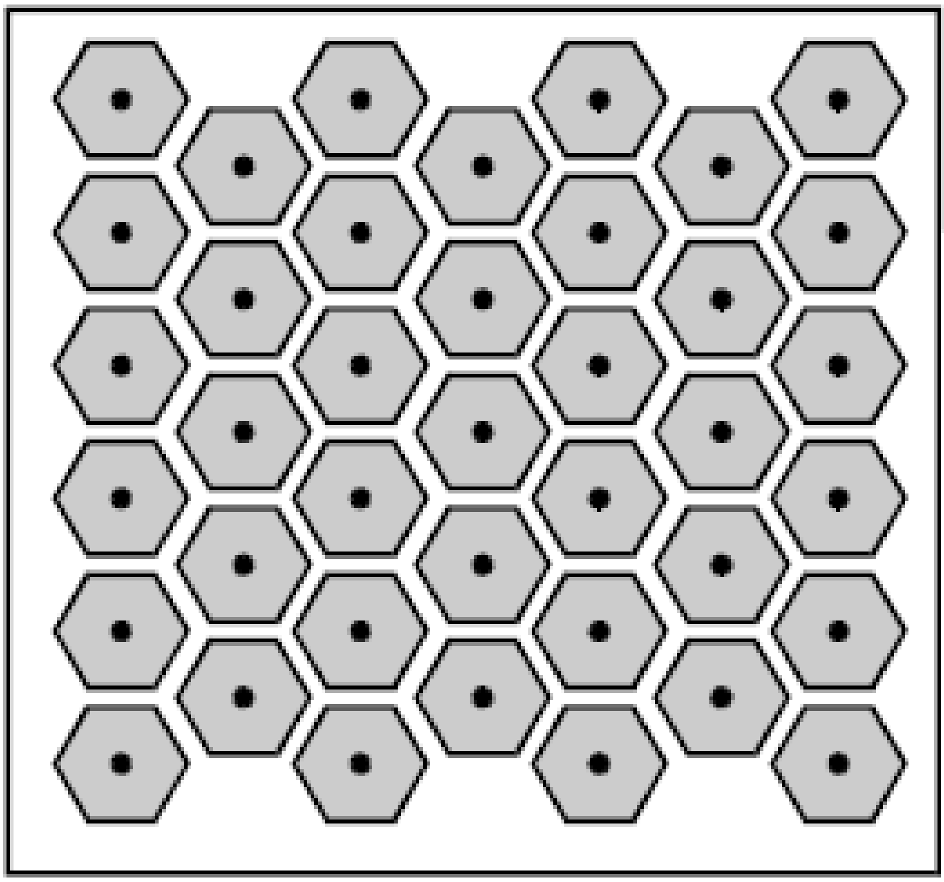

Figure 5. Top view of a corrugated high impedance surface [3].

Figure 6. Cross sectional view of a corrugated high impedance surface [3].

Due to the electrically small nature of the unit cells, the bulk behavior of metasurfaces such as this HIS developed by Sievenpiper, can be modeled using lumped elements such as the equivalent circuit shown in Figure 7. The lumped element model for this specific surface is viewed as first, an equivalent capacitance between the patches on the surface, and then, an equivalent inductance due to the separation between the patches and the metallic backing of the structure. There is also a small equivalent inductance along the back plane of the surface due to the electrical length between the elements. This lumped element model can be useful for design purposes and for visualizing potential methods for tuning the resonance of the circuit. As with most equivalent circuits, this model may be updated as more precision or additional levels of complexity are added to the structure. A similar lumped element may be used for other surfaces as well, provided that the unit cells are much smaller than the wavelengths of interest.

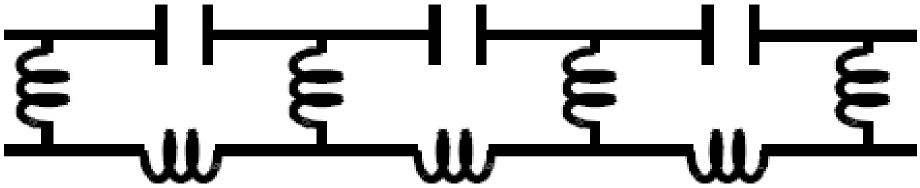

Figure 7. Equivalent circuit model for corrugated HIS [3].

One particular method of realizing a tunable impedance surface (TIS) from the structure shown in Figure 7 is to place varactor diodes between the patches in the unit cells. This element allows the equivalent capacitance between the elements to be altered based on a DC bias voltage which in turn, shifts the frequency at which the structure behaves as a HIS. Another method that has been employed to tune the surface is to place pin diodes between the unit cells and to use a square shape for the patch elements. This allows for the patches to be shorted together and behave as unit cells with varying periodicity. For example, shorting every other element switches from a 1x1 periodicity to a 2x2 periodicity which cuts the resonance frequency of the structure roughly in half and allows for the TIS to be implemented over a broad frequency range [59]. These tuning methods can then be transferred to leaky wave, frequency reconfigurable, and/or reflectarray antennas [48].

2.4.2 High Frequency Tunable Transmission Surfaces Using PIN Diodes

Tunable transmission surfaces are also possible in addition to the tunable HIS cells such as those developed by Sievenpier et. al. These tunable transmission surfaces can be realized through a number of methods, but this section will focus primarily on the use of PIN diodes to realize the reconfigurable elements. Generally, the surface is designed to consider two states, one in which the diode is unbiased and the surface transmits the incident field with very little modulation, and a second where the PIN diode is biased and the gain and phase of the transmitted field changes through the surface. This method has been used successfully by Dr. DiPalma in his work on a tunable TA system in the Ka-band of roughly 30 GHz [60].

Dr. DiPalma's work details the importance of generating an effective model for the PIN diode, particularly at high frequencies where the non-ideal effects of the lumped element may have a significant impact on the circuit behavior. An ideal PIN diode transitions between either an open or short circuit depending upon a DC bias voltage, but a physical diode often has an associated inductance and capacitance. This non-ideal behavior leads to an equivalent circuit such as those given in Figure 8 and Figure 9.

These equivalent parameters determine the upper operating frequency of the PIN diode and can significantly effect the isolation of the diode in the OFF state as well as the insertion loss in the ON state. This section uses the SMP1320-079LF PIN diode from Skyworks as an example. For the SMP diode, the manufacturer gives the values $L_{on} = 0.7nH$, $R_{on} \approx 0.75\Omega$, $C_{off} \approx 0.33pF$, and $R_{off} = 10M\Omega$. An example of the reflection (S_{11}) and Insertion Loss or Isolation (S_{12})are shown in Figure 10 and Figure 11, respectively. These figures show that the

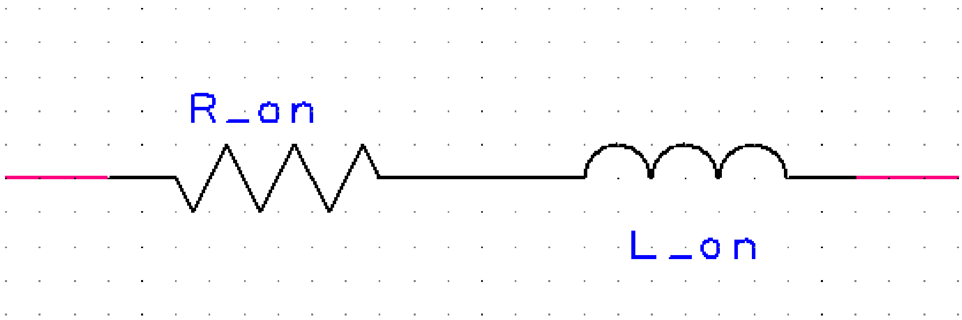

Figure 8. Equivalent circuit for PIN diode biased in ON state.

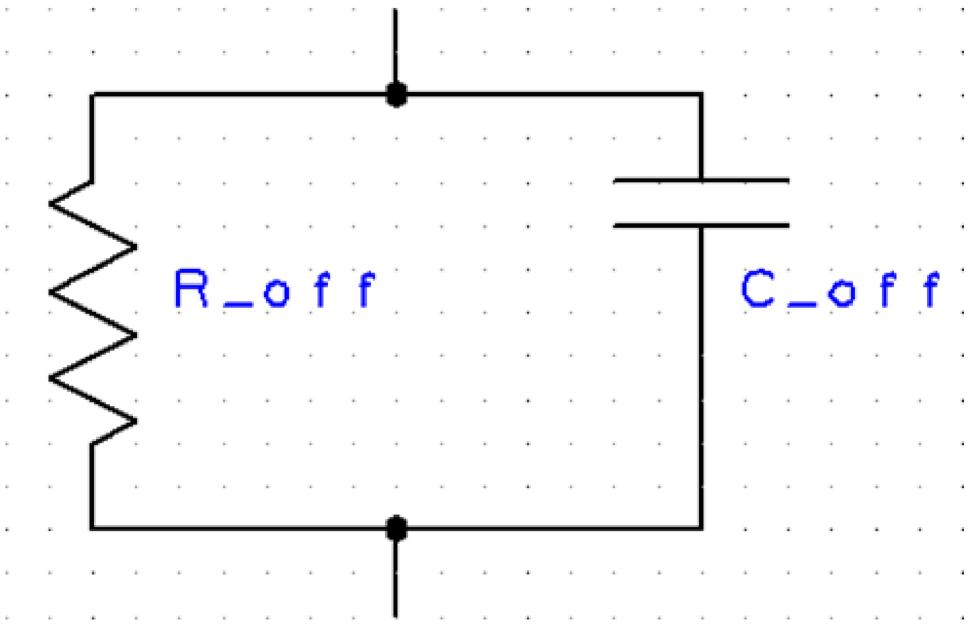

Figure 9. Equivalent circuit for PIN diode biased in OFF state.

diode has a significant difference between the ON/OFF states below 3 GHz, but between 3 and 10 GHz, this difference is less pronounced. At 10 GHz, there is almost no difference between the ON and OFF state as the transmission coefficient or isolation of the diode at 10 GHz is roughly 3 dB. The transmission and isolation is very important when selecting PIN diodes for a tunable surface as it effects the overall tunability and performance of the structure.

2.4.3 Optically Tunable Surfaces

A notable form of tunable metasurface that has garnered an increasing amount of attention in recent years is the concept of an optically tunable metasurface (OT-MS). These surfaces alter their electrical properties based on the presence of a light source that is used to illuminate the surface. The antenna designed in this work will utilize a tunable transmission surface which either allows or blocks an incident electromagnetic field, based on a light source which is used as a switching mechanism. Optical switching removes the need for wires and transmission lines to be integrated in the structure, which are present for conventional electronic switching methods. This reduces the losses due to the wires, which may be significant at higher frequencies.

Optically tunable metasurfaces are often designed for THz frequency applications and begin with a resonant structure [61]. A number of optical tuning mechanisms integrate a semiconductor such as AlGaAs or silicon into the structure which react to the incident light [62, 63]. Researchers often select THz frequencies for optical tuning designs because the skin depth of the incident light is electrically small at lower frequencies. The penetration depth of the light source must be notable for the transmission to be tuned by altering the dielectric properties of the integrated semiconductor. The alteration in the semiconductor is primarily due to photon

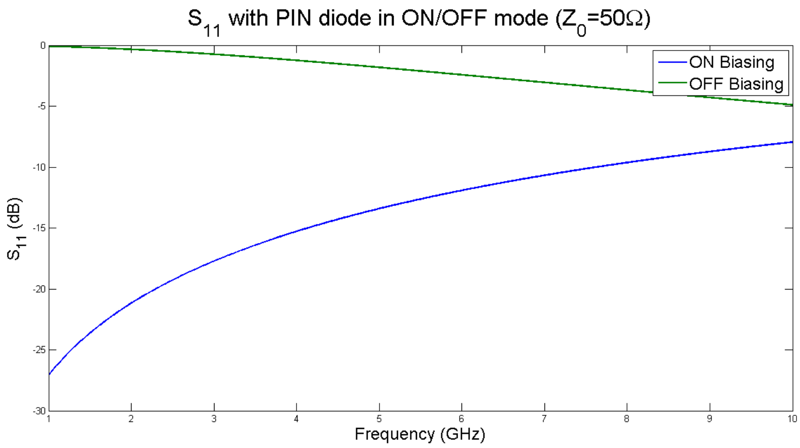

Figure 10. SMP-1320 reflection coefficient in different bias states.

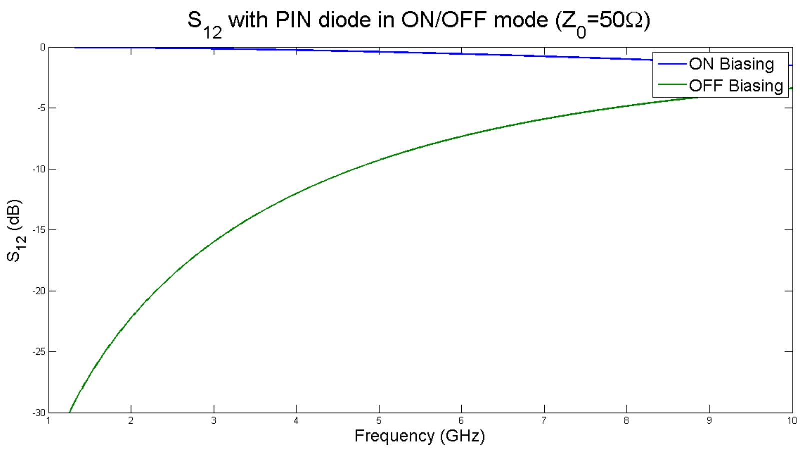

Figure 11. SMP-1320 transmission coefficient in different bias states.

absorption which creates an electron-hole pair that increases the conductivity of the material. The change in conductivity may be modeled through the Drude model and has been utilized to construct a broadly tunable and flexible OT-MS in the THz frequency range [64].

A major drawback of THz designs, however, is that they often require high precision equipment to fabricate and costly test equipment. In order to reduce the costs associated with construction, the novel antenna considered herein will require a surface that is operational at a lower frequency range. The new surface will utilize lumped element components in order to realize the benefits associated with an optically tunable surface.

CHAPTER 3

THEORY AND DESIGN CONSIDERATIONS

3.1 Radiating Element

The first step of antenna array design must begin with an accurate model of the radiation element. For this purpose, it is best to begin with a simplistic model and increase the complexity as needed in order to accurately capture the bulk behavior of the structure to the level of detail required. To this end, the simplest model to demonstrate the tunability of the system and the behavior of the electrically small radiating elements is a simple gap in a PEC plate [65]. This geometry is shown in Figure 12.

The gap struture consists of a PEC plate along the plane $x = 0$ with a gap located along the strip $-d/2 < x < d/2$ that is covered with an impedance sheet with variable conductivity $\sigma(x)$. The structure is surrounded by a linear, homogenous, isotropic medium (e.g. air) that is characterized by a wavenumber k and characteristic admittance $Y = Z^{-1}$. This gap is then excited by an E-polarized plane wave with a direction of propagation vector that lies in the x, y plane and forms the angle ϕ_0 with the negative x-axis. The incident electric and magnetic fields may then be written as

$$\overline{E}^i = \hat{z}e^{-jk(x\cos\phi_0 + y\sin\phi_0)}, \tag{3.1}$$

$$\overline{H}^i = Y(-\hat{x}\sin\phi_0 + \hat{y}\cos\phi_0)e^{-jk(x\cos\phi_0 + y\sin\phi_0)}. \tag{3.2}$$

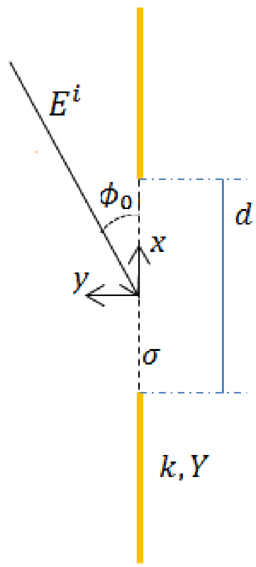

Figure 12. Geometry of gap in PEC plate.

For the gap structure, the incident field is both the original plane wave and its reflection due to the PEC plane, which transforms this expression to

$$\overline{E}^{i*} = \hat{z}2j\sin(y\sin\phi_0)e^{-jkx\cos\phi_0}. \tag{3.3}$$

From here, the geometry is analyzed in the elliptic cylindrical coordinate system (u, v, z) that is related to the rectangular coordinates by the series of equations

$$\begin{cases} x = \frac{d}{2}\cosh u\cos v \\ y = \frac{d}{2}\sinh u\sin v \\ z = z \end{cases}, \tag{3.4}$$

where $0 \le u < \infty,\ 0 \le v < 2\pi,\ -\infty < z < \infty$, and d is the interfocal distance of the coordinate system. Alternatively, the coordinates $\xi = \cosh u$ and $\eta = \cos v$ are sometimes used, though, particular attention must be paid to the fact that there is not a one to one relation between v and η. In elliptic cylindrical coordinates the incident field can be decomposed into a series of Mathieu functions as

$$\overline{E}^{i*}(u, v) = \hat{z}\sqrt{32\pi}\sum_{m=1}^{\infty}\frac{j^m}{N_m^o}\mathrm{Ro}_m^{(1)}(\gamma, u)\mathrm{So}_m(\gamma, v)\mathrm{So}_m(\gamma, \phi_0), \tag{3.5}$$

where $\mathrm{Ro}_m^{(1)}$ is the odd radial Mathieu function of the first kind and order m, So_m is the odd angular Mathieu function of order m, $\gamma = \frac{kd}{2}$, and N_m^o is a normalization factor defined in Stratton's reference text [66] as

$$N_m^o = \int_0^{2\pi} |\mathrm{So}_m(\gamma, v)|^2 dv. \tag{3.6}$$

Once the incident field is identified in the elliptic-cylindrical coordinates, the scattered field can be obtained through separation of variables. The condition that the scattered field must satisfy the Sommerfeld radiation condition results in the expression

$$\overline{E}^s(u,v) = \hat{z} \begin{cases} \sum\limits_{m=1}^{\infty} \frac{j^m}{N_m^o} a_m \mathrm{Ro}_m^{(4)}(\gamma, u)\mathrm{So}_m(\gamma, v)\mathrm{So}_m(\gamma, \phi_0) & 0 \leq v \leq \pi \\ \sum\limits_{m=1}^{\infty} \frac{j^m}{N_m^o} b_m \mathrm{Ro}_m^{(4)}(\gamma, u)\mathrm{So}_m(\gamma, v)\mathrm{So}_m(\gamma, \phi_0) & \pi \leq v \leq 2\pi \end{cases}, \tag{3.7}$$

where $\mathrm{Ro}_m^{(4)}$ is the odd radial Mathieu function of the fourth kind and order m and a_m and b_m are the modal expansion coefficients. Furthermore, the relationship

$$b_m = -a_m \tag{3.8}$$

is obtained due to the continuity of the electric field across the gap. The expansion coefficients a_m must then be solved based on the tangential magnetic field present along the gap, using the curl operator in the elliptic-cylindrical coordinates in conjunction with Maxwell's equations yielding

$$H_v^{i*}(u,v) = \begin{cases} \frac{Y\sqrt{32\pi}}{\gamma\sqrt{\xi^2-\eta^2}} \sum\limits_{m=1}^{\infty} \frac{j^m}{N_m^o} \mathrm{Ro}_m^{(1)\prime}(\gamma,u)\mathrm{So}_m(\gamma,v)\mathrm{So}_m(\gamma,\phi_0), & 0 < v < \pi \\ 0, & \pi < v < 2\pi \end{cases}, \tag{3.9}$$

$$H_v^{s}(u,v) = \begin{cases} \frac{Y\sqrt{32\pi}}{\gamma\sqrt{\xi^2-\eta^2}} \sum\limits_{m=1}^{\infty} \frac{j^m}{N_m^o} a_m \mathrm{Ro}_m^{(4)\prime}(\gamma,u)\mathrm{So}_m(\gamma,v)\mathrm{So}_m(\gamma,\phi_0), & 0 < v < \pi \\ -\frac{Y\sqrt{32\pi}}{\gamma\sqrt{\xi^2-\eta^2}} \sum\limits_{m=1}^{\infty} \frac{j^m}{N_m^o} a_m \mathrm{Ro}_m^{(4)\prime}(\gamma,u)\mathrm{So}_m(\gamma,v)\mathrm{So}_m(\gamma,\phi_0), & \pi < v < 2\pi \end{cases}, \tag{3.10}$$

where $\prime$ denotes the derivative with respect to u and the total tangential magnetic field is

$$H_v(u,v) = H_v^{i*}(u,v) + H_v^{s}(u,v). \tag{3.11}$$

Due to the surface current present on the conducting strip, the boundary condition along the gap becomes

$$\overline{J}_s = \hat{z}\sigma E_z(0,v) = \hat{u} \times (\overline{H}(0,v) - \overline{H}(0,2\pi - v)). \tag{3.12}$$

Substituting the expanded fields into Equation 3.12 yields

$$\begin{aligned} \frac{Y\sqrt{32\pi}}{\gamma\sin v} \sum_{m=1}^{\infty} \frac{j^m}{N_m^o} \left(2a_m\mathrm{Ro}_m^{(4)\prime}(\gamma,0) + \mathrm{Ro}_m^{(1)\prime}(\gamma,0)\right) \mathrm{So}_m(\gamma,v)\mathrm{So}_m(\gamma,\phi_0) \\ = \sigma(v) \sum_{m=1}^{\infty} \frac{j^m}{N_m^o} a_m \mathrm{Ro}_m^{(4)}(\gamma,0)\mathrm{So}_m(\gamma,v)\mathrm{So}_m(\gamma,\phi_0). \end{aligned} \tag{3.13}$$

Algebraic manipulation then leads to

$$\sum_{m=1}^{\infty} a_m \frac{j^m}{N_m^o}\left(\mathrm{Ro}_m^{(4)\prime}(\gamma,0) - \frac{\gamma\sigma(v)\sin v}{2Y\sqrt{32\pi}}\mathrm{Ro}_m^{(4)}(\gamma,0)\right)\mathrm{So}_m(\gamma,v)\mathrm{So}_m(\gamma,\phi_0)$$
$$= -\sum_{m=1}^{\infty}\frac{j^m}{N_m^o}\frac{1}{2}\mathrm{Ro}_m^{(1)\prime}(\gamma,0)\mathrm{So}_m(\gamma,v)\mathrm{So}_m(\gamma,\phi_0). \quad (3.14)$$

Since this equation holds along the gap from $0 < v < \pi$, Equation 3.14 may be multiplied by $\mathrm{So}_n(\gamma, v)$ for any $n \in \mathbb{N}$, and integrated from 0 to π which yields

$$\sum_{m=1}^{\infty} a_m \frac{j^m}{N_m^o}\left(\mathrm{Ro}_m^{(4)\prime}(\gamma,0)N_m^o\delta_{m,n} - \frac{\gamma}{2Y\sqrt{32\pi}}\mathrm{Ro}_m^{(4)}(\gamma,0)\Delta_{n,m}\right)\mathrm{So}_m(\gamma,\phi_0)$$
$$= -\frac{j^n}{2}\mathrm{Ro}_n^{(1)\prime}(\gamma,0)\mathrm{So}_n(\gamma,\phi_0), \quad (3.15)$$

where

$$\Delta_{n,m} = \int_0^{\pi}\sigma(v)\sin v\,\mathrm{So}_m(\gamma,v)\mathrm{So}_n^*(\gamma,v)dv, \quad (3.16)$$

$\delta_{m,n}$ is the Kroenecker delta function and $*$ denotes the complex conjugate. Multiplying both sides of Equation 3.15 by $\frac{j^{-n}}{\mathrm{Ro}_n^{(4)\prime}\mathrm{So}_n(\gamma,\phi_0)}$ gives

$$a_n - \sum_{m=1}^{\infty} a_m \frac{j^{m-n}}{N_m^o}\frac{\gamma}{2Y\sqrt{32\pi}}\frac{\mathrm{Ro}_m^{(4)}(\gamma,0)}{\mathrm{Ro}_n^{(4)\prime}(\gamma,0)}\Delta_{n,m}\frac{\mathrm{So}_m(\gamma,\phi_0)}{\mathrm{So}_n(\gamma,\phi_0)} = -\frac{\mathrm{Ro}_n^{(1)\prime}(\gamma,0)}{2\mathrm{Ro}_n^{(4)\prime}(\gamma,0)}. \quad (3.17)$$

This expansion in theory, leads to an infinite series of equations unless $\sigma(v) = \frac{C}{\sin v} = C \csc v$ where C is a constant, but for analysis the series may be truncated to a finite number N of terms where $N > 2kd$. This then leads to a matrix equation

$$[I - D][A] = [B], \tag{3.18}$$

where A is a column vector of the expansion coefficients a_m, B is a column vector with elements

$$B_n = -\frac{\mathrm{Ro}_n^{(1)\prime}(\gamma, 0)}{2\mathrm{Ro}_n^{(4)\prime}(\gamma, 0)}, \tag{3.19}$$

I is an $N \times N$ identity matrix, and D is an $N \times N$ matrix with elements

$$D_{n,m} = \frac{j^{m-n}}{N_m^o} \frac{\gamma}{2Y\sqrt{32\pi}} \frac{\mathrm{Ro}_m^{(4)}(\gamma, 0)}{\mathrm{Ro}_n^{(4)\prime}(\gamma, 0)} \Delta_{n,m} \frac{\mathrm{So}_m(\gamma, \phi_0)}{\mathrm{So}_n(\gamma, \phi_0)}. \tag{3.20}$$

This series of equations leads to a matrix equation which must be inverted to solve for the expansion coefficients. Analytic closed form solutions for the expansion coefficients are, however, available for the case where

$$\sigma(v) = \frac{\sigma_0}{\sin v}, \tag{3.21}$$

in which case

$$\Delta_{m,n} = \sigma_0 N_m^o \delta_{m,n}. \tag{3.22}$$

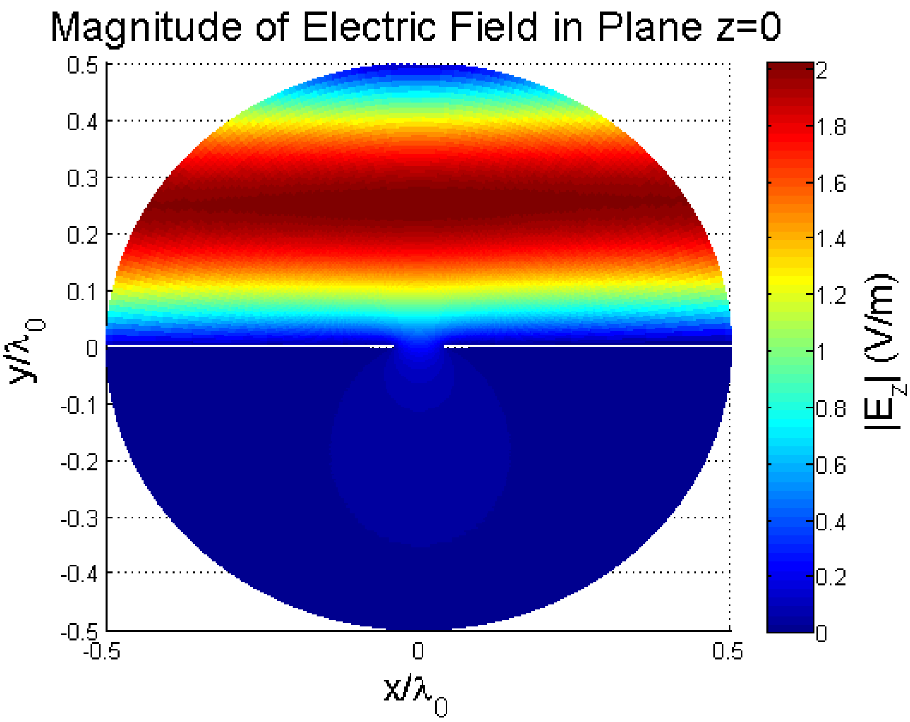

Figure 13. Magnitude of the electric field scattered by the gap in the PEC surface.

This identity then leads to

$$a_n = \frac{B_n}{1 - D_{n,n}}. \tag{3.23}$$

Numerical results are also convenient for the case where $2kd < 1$ (i.e. $d < \lambda_0/4\pi \approx \lambda_0/12$) and the primary scattered fields may be approximated using only a single term. Figure 13 shows the magnitude of the E_z for the case of $\phi_0 = \pi/2$, $d = \lambda_0/12$, and $\sigma(v) = 0$. In this figure the electric field is expanded to 7 terms in order to accurately plot the electric field in the entire region of the $0.5\lambda_0$ elliptic cylinder cenetered on the gap and computed using Matlab [67]. This result shows that the solution satisfies the continuity condition along the gap as well as the condition that the electric field vanishes along the PEC plate. The results also demonstrate that there is a strong standing wave pattern in the region above the gap where the incident and reflected field are present and then there is a radiated field that propagates below the gap.

3.1.1 Far Field Radiation

It is possible to extract a far field radiation pattern from thie previously examined gap using the asymptotic behavior of the radial Mathieu function of the fourth kind which is given as [68]

$$\mathrm{Ro}_m^{(4)} \sim \frac{j^m}{\sqrt{\gamma\xi}} e^{-j\gamma\xi + \frac{j\pi}{4}} \sim \frac{j^m}{\sqrt{k\rho}} e^{-jk\rho + \frac{j\pi}{4}}, \tag{3.24}$$

where $\rho = \sqrt{x^2+y^2}$ is the radius of a circular cylindrical coordinate system. This then results in the asymptotic field behavior

$$E_z(u \to \infty, \pi < v < 2\pi) \sim -\sqrt{\frac{32\pi}{k\rho}} e^{-jk\rho + \frac{j\pi}{4}} \sum_{m=1}^{\infty} \frac{(-1)^m}{N_m^o} a_m \mathrm{So}_m(\gamma, v) \mathrm{So}_m(\gamma, \phi_0) = f(v) \frac{e^{-jk\rho}}{\sqrt{k\rho}}, \tag{3.25}$$

where

$$f(v) = -\sqrt{32\pi} e^{\frac{j\pi}{4}} \sum_{m=1}^{\infty} \frac{(-1)^m}{N_m^o} a_m \mathrm{So}_m(\gamma, v) \mathrm{So}_m(\gamma, \phi_0), \tag{3.26}$$

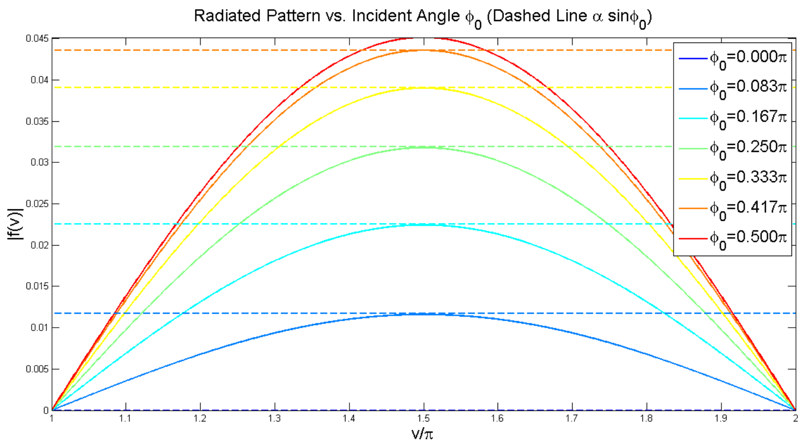

Figure 14. Far field pattern vs. angle of incidence ϕ_0.

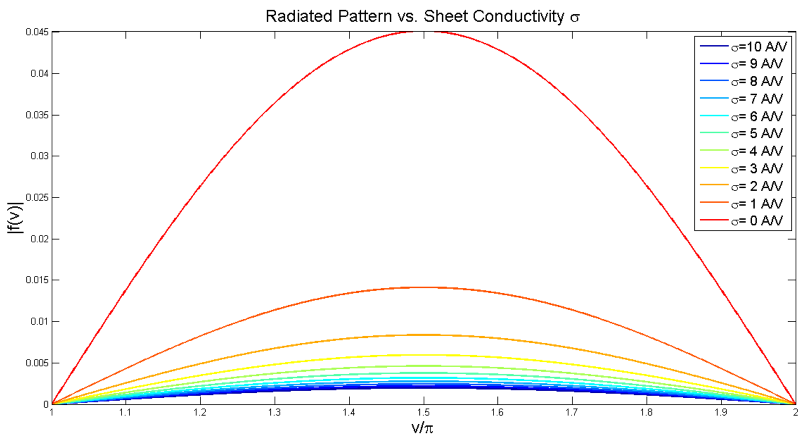

Figure 15. Far field pattern vs. sheet impedance σ.

is the far field pattern. Two key factors can effect the far field pattern, the angle of incidence ϕ_0 or the sheet conductivity $\sigma(v)$. Figure 14 shows the magnitude of the far field pattern as ϕ_0 is varied from 0 to $\pi/2$ for a gap of $d = \lambda_0/12$ with no sheet impedance. For the case of a small gap the odd angular Mathieu function behaves roughly as a sinusoid and results in

$$|f(v)|\alpha \mathrm{So}_1(\gamma, v) \sim \sin(v)\alpha H_x^i, \ \pi < v < 2\pi, \tag{3.27}$$

which is also roughly proportional to the incident x directed magnetic field for the case of an electrically small gap which we expect to behave similar to a small dipole. The relationship to $\sigma(v)$ is slightly more complex, but for the case of $d = \lambda_0/12$ the relationship can be obtained using a single term for the series expansion. Figure 15 shows the variation in the radiated field for varying constant sheet conductivities from 0 to 10 A/V, with $\phi_0 = \pi/2$. From Figure 15 it can be observed that increasing the conductivity provides a method to modulate the radiated field. Using a finite conductivity does, however, allow for some of the field to still be transmitted, which must be accounted for in the overall antenna design which will be completed in the following sections.

3.2 Faceting Algorithm

One key limitation of the gap structure for conformal antenna design is that the PEC plate is a planar structure, while a conformal surface is smoothly curved. To tackle this problem, a faceting algorithm is developed to best approximate an arbitrary continuous convex curve $\Gamma(x)$ that is defined on $x_s \leq x \leq x_f$ with a faceted planar surface $\Gamma^*(x)$ which satisfies the conditions

$$\Gamma^*(x_n) = \Gamma(x_n), \tag{3.28}$$

$$\Gamma^*(x) \leq \Gamma(x), \tag{3.29}$$

$$(\Gamma^*(x_n) - \Gamma^*(x_{n-1}))^2 + (x_n - x_{n-1})^2 = L^2 > 0, \tag{3.30}$$

$$\Gamma^{*\prime\prime}(x) = 0,\ \ x \in \mathbb{R} \setminus \{x_1, x_2, ...x_n\}, \tag{3.31}$$

where L is the size of the gap and the series $\{x_1, x_2, ...x_n\}$ is a finite number of junction points for the facets. The resulting curve Γ^* is a piecewise linear function where each line segment has a length L and the curve may be covered with a relatively thin radome over the surface $\Gamma(x)$ if the smoothness of the surface is a key concern.

It is best to start at the location $x = 0$ and facet the surface once in the increasing direction and once in the decreasing directio as to maintain even symmetry if $\Gamma(x)$ is even. To keep this balance, the surface is faceted once in the region $x_s \leq x \leq 0$ and once on the region $0 \leq x \leq x_f$. This section will focus on the region $0 \leq x \leq x_f$ for simplicity, however, the algorithm for the second region is very similar except that the series of points x_n will be forced to decrease rather than increase. The line segments that act as tiles between the points are placed along Γ^* by beginning at the point $x_1 = 0$, $y_1 = \Gamma(0)$ and then solving for Equation 3.30 using

$$\Gamma(x_n) - \sqrt{L^2 - (x_n - x_{n+1})^2} = \Gamma(x_{n+1}) = y_{n+1}, \tag{3.32}$$

until $x_N > x_f$. Γ^* is then found by linear iterpolation using

$$\Gamma^*(x) = y_n + \frac{y_{n+1} - y_n}{x_{n-1} - x_n},\ x_n \leq x \leq x_{n+1}, \tag{3.33}$$

which satisfies Equation 3.31 due to the concavity of Γ. A pictorial illustration of this method is shown in Figure 16.

Once the curve is faceted, it is also necessary to define the rest of antenna geometry in order for the system to be analyzed through simulations. To this end, the edges of the surface that is connected to the points $(\pm a, 0)$ which are also connected to each other by a wall that creates a cavity behind the surface that is used to excite the structure. The outer walls are then extended by adding walls parallel to the left and right end facets and continuing the walls until they reach the x axis.

This algorithm is implemented using Matlab [69] and the following fiures show results for the case of a circular cylindrical surface with a vertical translation. The dimensions are chosen

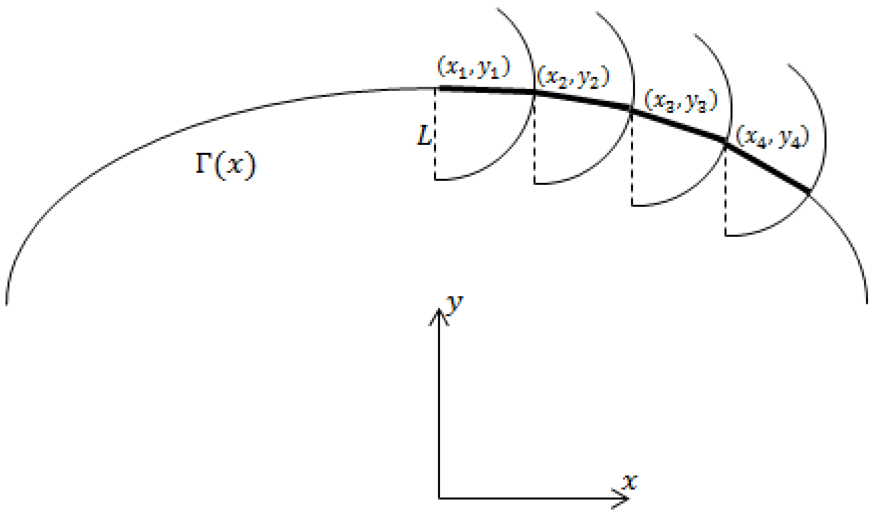

Figure 16. Method of facetting curved surface.

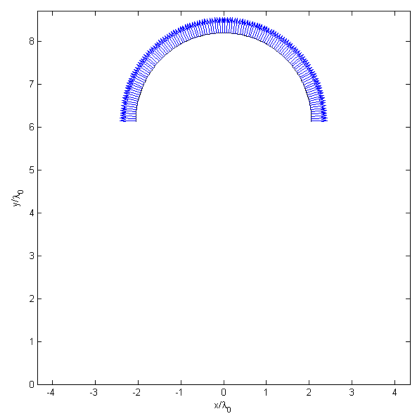

Figure 17. Faceted circular cylindrical surface.

such that $f_0 = 8\ GHz \rightarrow \lambda_0 \approx 37.5\ mm$ and the facet length is $1.9mm$. The surface of interest is then defined on $2.05\lambda_0 \leq x \leq 2.05\lambda_0$ by the equation

$$\Gamma(x) = 2.05\lambda_0(s(x/2.05\lambda_0) + 3), \tag{3.34}$$

where

$$s(x) = \Re(\sqrt{1 - x^2}) - 1000 * \Im(\sqrt{1 - x^2}). \tag{3.35}$$

The resulting facets along with the unit normal vectors pointing away from the facets are shown in Figure 17. The reasons for the offset and the specific values chosen will be discussed in later sections.

3.3 Simulation Construction

Because of the complex shape of the cavity behind the surface, the excitation magnitudes of the slots are computed through a method of moments (MoM) solver such as FEKO. The generated geometry may be exported from Matlab to FEKO using LUA scripts that are generated in Matlab. The first step is to generate the excitation of the model which will be fed by a wire placed along the $x = 0$ plane with an offset spacing deltaV. The following is an example of the LUA script to generate this excitation.

```
deltaV = project.Variables:Add("deltaV", "5.00")
PinSpacing = project.Variables:Add("PinSpacing", "0.05")
PinSpacing = project.Variables:Add("Rwire", "0.01")
```

```
properties = cf.Line.GetDefaultProperties()
properties.End.N = "0.2032"
properties.End.U = "0"
properties.End.V = "DeltaV"
properties.Label = "Line1"
properties.Start.N = "PinSpacing"
properties.Start.U = "0"
properties.Start.V = "DeltaV"
Line1 = project.Geometry:AddLine(properties)
properties = cf.WirePort.GetDefaultProperties()
properties.Label = "Port1"
properties.Location = cf.Enums.WirePortLocationEnum.End
Line1 = project.Geometry["Line1"]
Wire5 = Line1.Wires["Wire5"]
properties.Wire = Wire5
Port1 = project.Ports:AddWirePort(properties)
properties = cf.VoltageSource.GetDefaultProperties()
properties.Label = "VoltageSource1"
properties.Terminal = project.Ports["Port1"].Terminal
VoltageSource1 = ...
project.SolutionConfigurations["StandardConfiguration1"].Sources:AddVoltageSource(properties)
```

In addition to defining the excitation source, the LUA script must also define the polygons that make up the geometry. An example of this is shown below for a simple rectangle.

```
properties = cf.Polygon.GetDefaultProperties()
properties.Corners[1] = {}
properties.Corners[1].U = "-0.30480"
properties.Corners[1].V = "0.00000"
properties.Corners[1].N = "0.00000"
properties.Corners[2] = {}
properties.Corners[2].U = "0.30480"
properties.Corners[2].V = "0.00000"
properties.Corners[2].N = "0.00000"
properties.Corners[3] = {}
properties.Corners[3].U = "0.30480"
properties.Corners[3].V = "0.00000"
properties.Corners[3].N = "0.27147"
properties.Corners[4] = {}
properties.Corners[4].U = "-0.30480"
properties.Corners[4].V = "0.00000"
```

properties.Corners[4].N = "0.27147"

properties.Label = "feed_polygon"

feed_polygon = project.Geometry:AddPolygon(properties)

The LUA script may be generated from Matlab using the fprintf function since the LUA script is stored in a simple ASCII text file. The LUA script is then executed in CAD FEKO to generate a CAD model of the horn structure using PEC polygons. This structure is shown in Figure 18 with a coarse triangular mesh, where the PEC plane is utilized to take advantage of the symmetry of the structure and reduce the polygon count. From this model the values of the magnetic field along the plane $z = 0$ are then extracted to determine the relative excitation magnitudes using the near field request in Figure 19 and the method discussed in 3.3.1.

3.3.1 Excitation Magnitudes

The simulation to determine the surface current on the structure is then run using the FEKO Student edition on a Lenovo Z40 laptop with an Intel core i7 processor and 8 GB of RAM. The coarse mesh option in FEKO is selected in order to keep the polygon count below the allowable amount for the student edition. Once the simulation runs, FEKO is able to extract the magnetic field and as a result the surface current magnitude on the plane. The resulting fields for this specific configuration is shown in Figure 20 and the phase of the x directed component is shown in Figure 21. It should be noted that since the magnetic field ia shown for the plane $z = 0$, the normal magnetic field vanishes and thus this image shows the magnitude of the tangential magnetic field and therefore the resulting surface currents. The phase of the field is either in

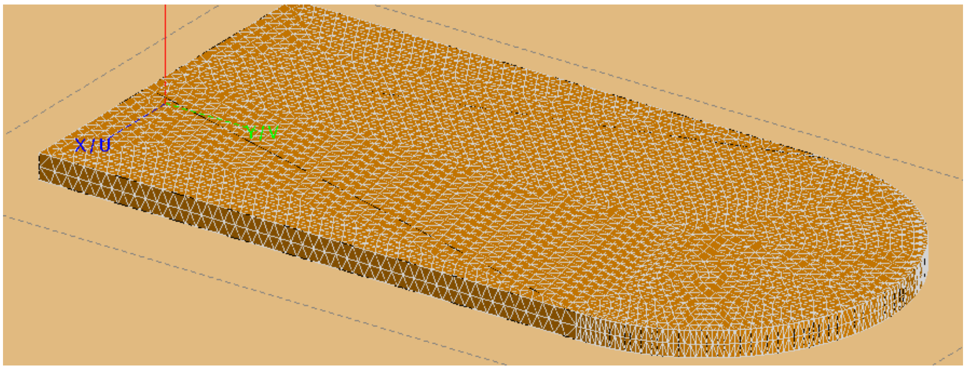

Figure 18. LUA generated model of conformal structure covered with a PEC surface.

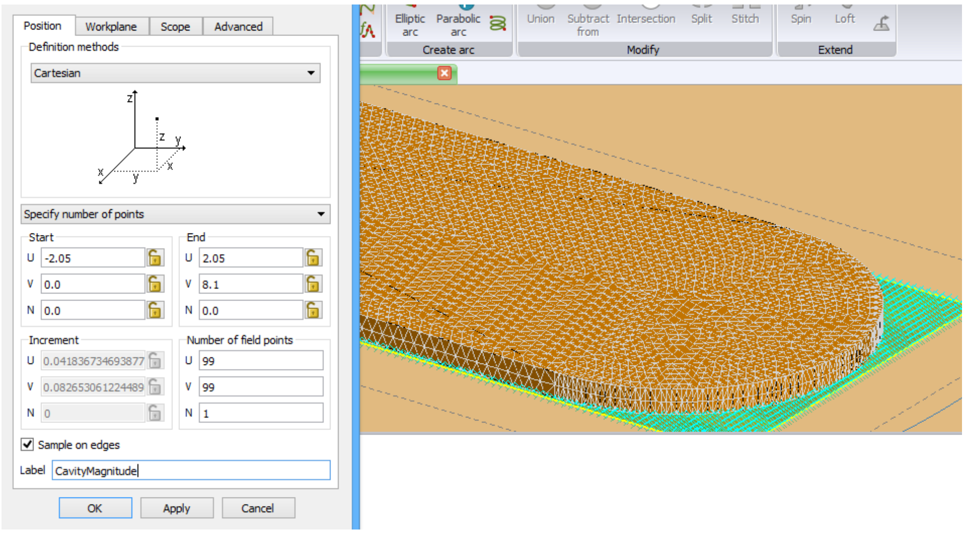

Figure 19. Near field request to determine excitation magnitudes.

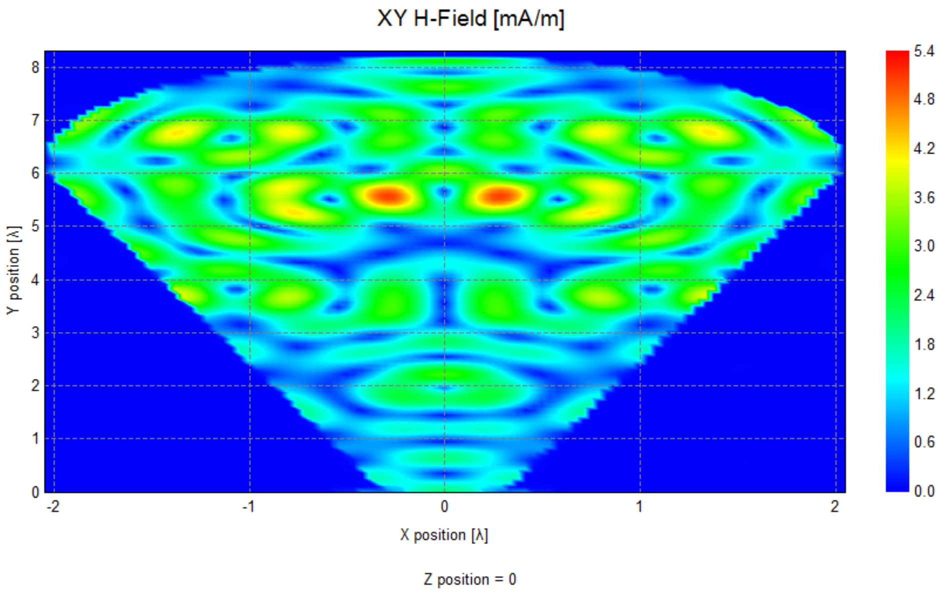

Figure 20. Magnetic field magnitude along plane $z = 0$ inside the structure.

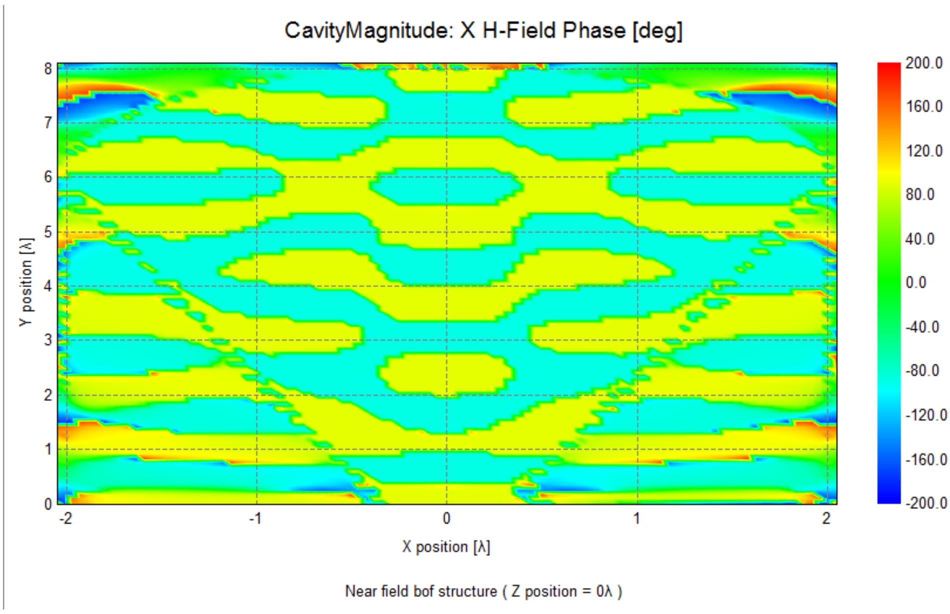

Figure 21. X directed magnetic field phase along plane $z = 0$ inside the structure.

phase or 180° out of phase due to the fact that the internal structure forms a closed cavity. It can be seen from this figure that the curved surface is illuminated relatively evenly with the exception of the far corners, which is important in order for the beam to be steerable over a broad range of angles.

The magnetic field information is then exported to a HFX text file from FEKO which can easily be converted to a CSV file using excel or automated script. The CSV format is important because it can then be imported into Matlab through the CSV read function. This table then contains information about the magnitude of the tangential magnetic field at the $X - Y$ coordinates which Matlab can use to determine the excitation magnitude of the elements on the surface, and thus, their comparative weights when computing the total radiated fields.

It can be seen from Figure 20 that the field at grid elements which straddle the PEC wall are ambiguous in their magnitude because of the discontinuity in their region so the Matlab script reads from the element immediately inside the wall. This magnetic field is then proportional to the radiated field by the element on the surface due to the relationship between the incident tangential magnetic field and the radiated field in Equation 3.27.

3.4 Compact Genetic Algorithm

The excitation magnitudes and faceted surface of the antennna structure are used to inform the compact genetic algorithm (CGA) which will be utilized to design the excitation patterns for the antenna [70]. The CGA is utilized because of its ability to converge relatively quickly, similar to conventional genetic algorithm (GA) methods. Additionally, the CGA utilizes a randomization method to determine the individual genes or, in this case, excitation magnitudes

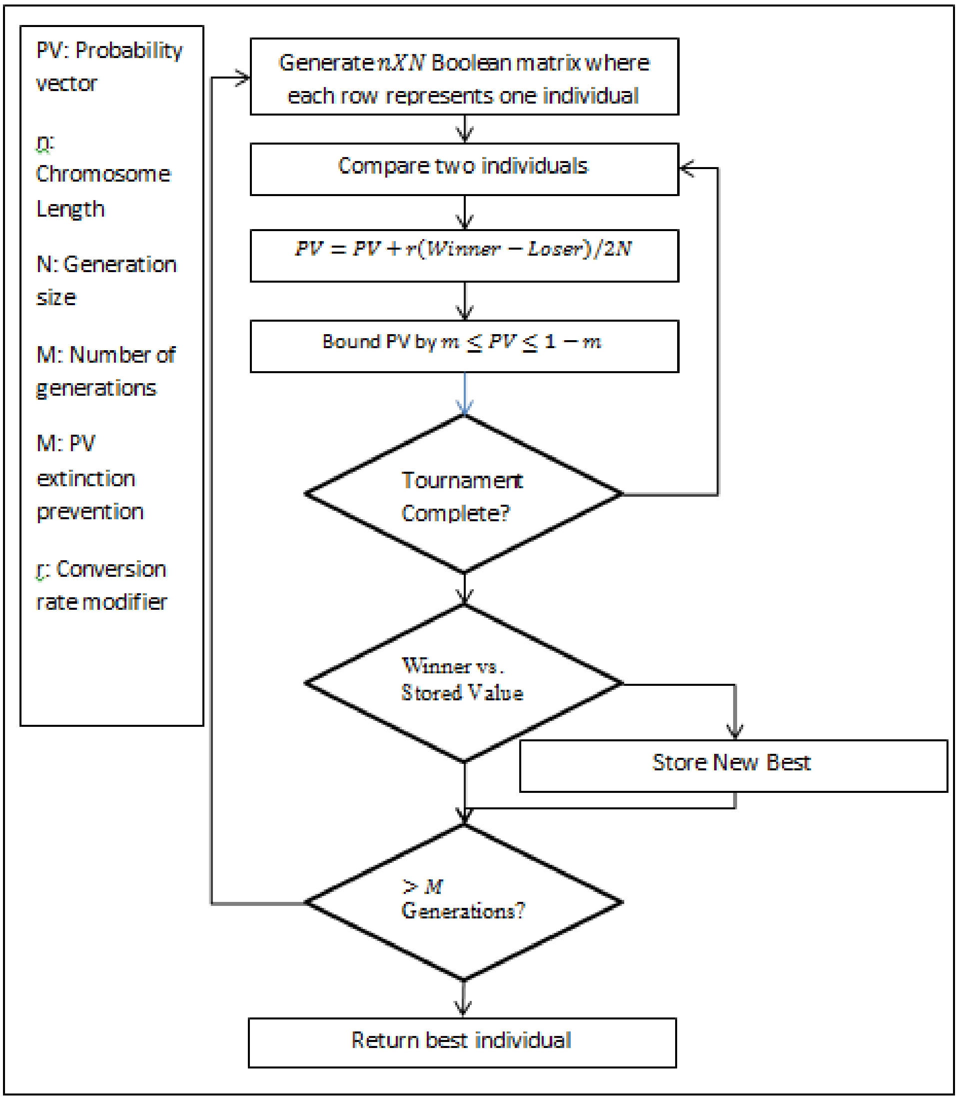

Figure 22. Overview of the compact genetic algorithm.

in order to simulate a larger diverse population size such as the one generated through particle swarm optimization (PSO). Large diverse populations have the advantage of reducing the likelihood of converging to a local minimum or maximum of the cost function.

The method of the CGA is shown in Figure 22. The algorithm begins by first initializing a probability vector which is utilized to assign a 0 or 1 to the various excitation magnitudes. The computational process forms a $M \times N$ matrix in which each row represents the excitation pattern for an individual mask. The directivities of these individual rows are then calculated using a cost function, described in 3.4.1, and the costs are compared in a tournament style with $\log_2 M$ rounds to determine the best score and is then compared to a previously stored best score from past generations. While the tournament occurs the probability vector (PV) is updated to increase its likelihood to generate individual rows similar to the winner of each comparison so that future generations will excite gaps that are more prevalent in the higher gain configurations.

Every element of the PV is also bounded by $m < PV(n) < 1-m$, where m is the extinction bound, to prevent the extinction of any individual genes. This is because if the PV vector was allowed to reach 0 or 1, it would result in all individuals past a certain generation have a given gap either on of off which would reduce the degrees of freedom of the problem. Once the prescribed number of generations are completed, the best individual row is returned for the given design direction. The CGA is a very powerful heuristic optimization tool for complex problems, but as with other heuristic models it requires an accurate cost function that can be quickly computed which requires a sufficient, but simplified model for the overall system.

3.4.1 Cost Function

The cost function for the CGA is used to quickly compute the directivity of each mask pattern. The cost function computation is primarily done by pre-computing the radiation pattern associated with each gap and using this data to compute the conformal array using matrix operations to compute Equation 2.12. The first step in this process is to compute the radiation pattern associated with the N gaps from the faeting function that is computed for M angles equally spaced from $0 \leq \phi \leq 360°$. The weighted element of the excitation matrix $Ex_{n,m}$ is computed for the element n in the direction ϕ_m by using

$$Ex_{n,m} = g_n(\phi_m)e^{-jkR_n(\cos(\phi_m - P_n)}, \tag{3.36}$$

where (R_n, P_n) is the location of the n^{th} element in polar coordinates and

$$g_n(\phi_m) = J_n \sin(\phi_m - N_n)\Theta(\sin(\phi_m - N_n)), \tag{3.37}$$

is obtained by rotating an scaling Equation 3.26 for a small gap, where J_n is the relative excitation magnitude of the n^{th} element extracted from the FEKO simulation, N_n is the angle that the unit normal vector that the n^{th} gap forms with the y axis, and Θ is the unit step function. This process is repeated for all the gaps resulting in a $N \times M$ matrix where M is the number of radiation directions sampled and N is half the number of facets generates by the faceting algorithm since due to the physical construction needs of the surface which will be discussed in further sections.

Equation 2.12 can then be rapidly computed for a $1 \times N$ excitation vector Msk through simple matrix multiplication.

$$F(\phi) = Msk * Ex. \tag{3.38}$$

The excitation mask vector is assigned one of two distinct values (ideally 0 or 1) based on whether the gap is ON or OFF. Furthermore in order to better approximate the physical surface, a leakage factor is introduced to model the tunability ratio of the surface. This leakage is implemented such that gaps that are OFF have a reduced magnitude rather than a perfect zero when computing Equation 3.38.

Two key assumptions of the cost function model are that the gap radiation over the conformal surface is similar to that of a gap in a PEC plate and that the mutual coupling between gaps is negligible. The first assumption can be verified by simulating the case of a single gap being open in FEKO and comparing it to the theoretical model. These simulated radiation patterns are shown for the case of the center gap and the far right gap in the surface in Figure 23. As expected, the forward radiation from each gap behaves similarly to the sinusoidal function, while the radiation patterns in the rear differ with the cost function pattern because the back lobes are not modeled. This variation, however, is less of a concern because the antenna will generally be mounted on an electrically large structure which would further reduces the rear lobes. In order to fully verify that these assumptions are met the theoretical patterns will be compared with simulation results to verify their accuracy.

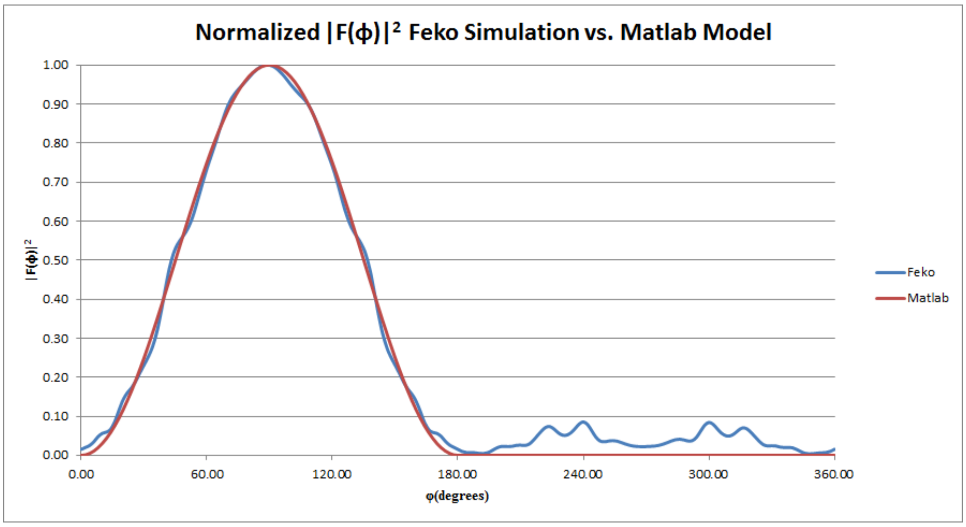

(a)

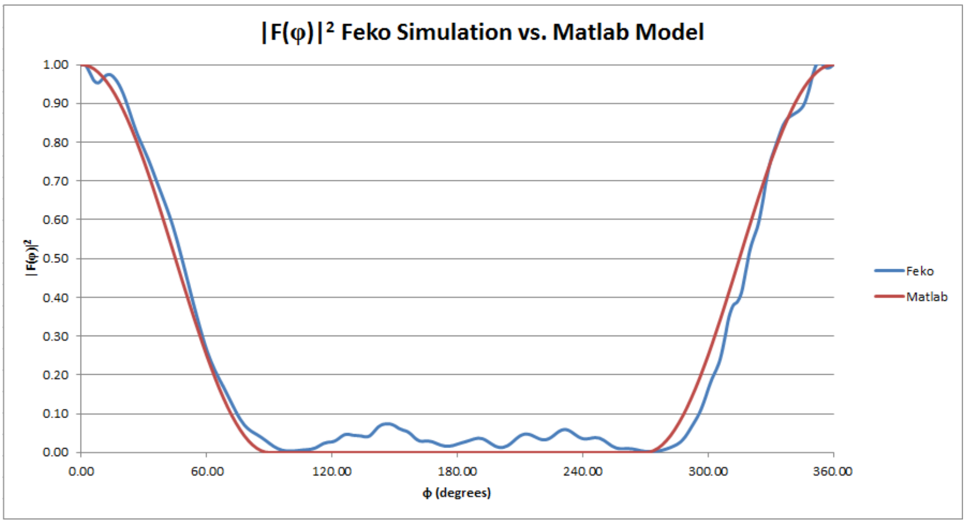

(b)

Figure 23. Theoretical and simulated radiation pattern of gap on (a) front of conformal surface (b) far right of conformal surface.

3.5 Simulation Correlation

The generated radiation patterns may be correlated with MoM simulations by setting the leakage value to 0 and generating masks for a number of target angles. By setting the leakage to zero it allows for the mask to be implemented by either leaving the gap open or covering the surface with a PEC. Since the radiation patterns for the gaps have already been verified, the primary aim of this correlation is to confirm that the coupling between adjacent gaps will not significantly alter the radiation pattern.

To this end, the CGA is run for beam steering in the sector $\phi = 90 \pm 60°$with a resolution of 10°. The CGA is run for 500 generations with a population size of 2^9, the convergence rate multiplier is set to 0.5, and the extinction prevention bound is set to 0.1. It should be noted that due to the fact that a gap is only placed on every other facet, the structure is not symmetric. The resulting patterns are shown in Figure 24 along with the resulting directivities and computation time in Table I.

The optimized directivities are accompanied by associated masks and generational information to ensure the convergence of the CGA. The mask associated with a beam steered towards $\phi = 0°$ is shown in Figure 25 as well as the generation data in Figure 26. It can be seen from Figure 26 that the CGA converges near the optimal pattern after roughly 150 generations however successive generations are included in case the randomization may obtain a better result which occurred around the 450^{th} generation in this run. Figure 25 also confirms common intuition that the pattern to obtain maximum directivity results from primarily exciting gaps pointing

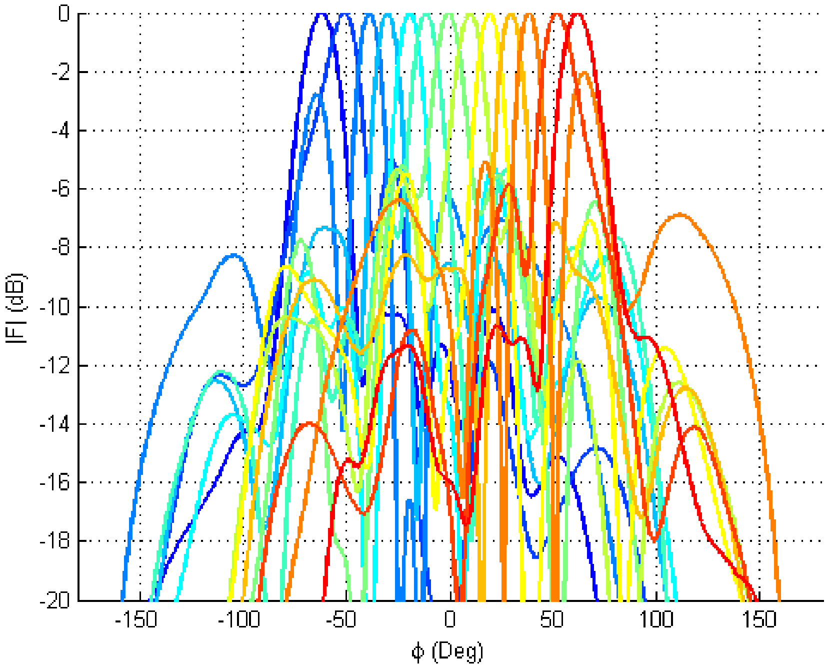

Figure 24. Radiation patterns computed by the CGA.

Target Angle	Directivity	Computation Time
-60°	13.84 dBi	121.2 s
-50°	13.39 dBi	115.6 s
-40°	12.47 dBi	114.7 s
-30°	13.28 dBi	116.6 s
-20°	13.81 dBi	118.0 s
-10°	12.97 dBi	123.8 s
0°	13.13 dBi	117.0 s
10°	13.36 dBi	112.2 s
20°	13.55 dBi	114.4 s
30°	13.60 dBi	116.9 s
40°	11.70 dBi	112.3 s
50°	13.47 dBi	118.8 s
60°	13.96 dBi	118.0 s

TABLE I

DIRECTIVITIES AND COMPUTATION TIME OF CGA.

towards the target direction in addition to a number of the side gaps to further trim the main beam.

The optimized pattern is then compared to simulation information in order to verify it's accuracy. This is done by exporting the horn information and the associated mask to CAD FEKO resulting in the structure shown in Figure 27. The results in Figure 28 show that the Matlab model accurately predicts the shape of the main beam as well as the locations of the side lobes. The magnitude of the side lobes does vary between the model and the simulation as well as the presence of the back lobes which are not included in the model. These back lobes have a minimal effect on the overall directivity of the system since this is primarily determined

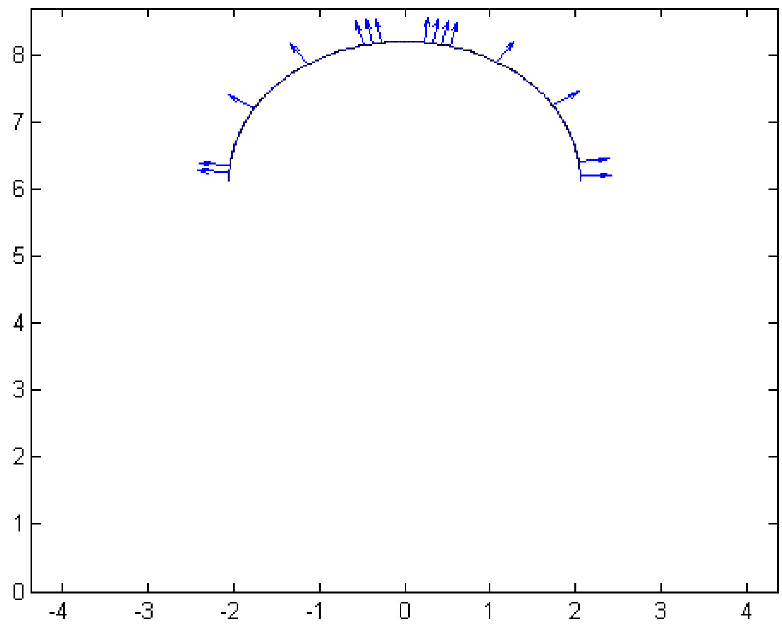

Figure 25. Theoretical mask on front of conformal surface for 0° target angle.

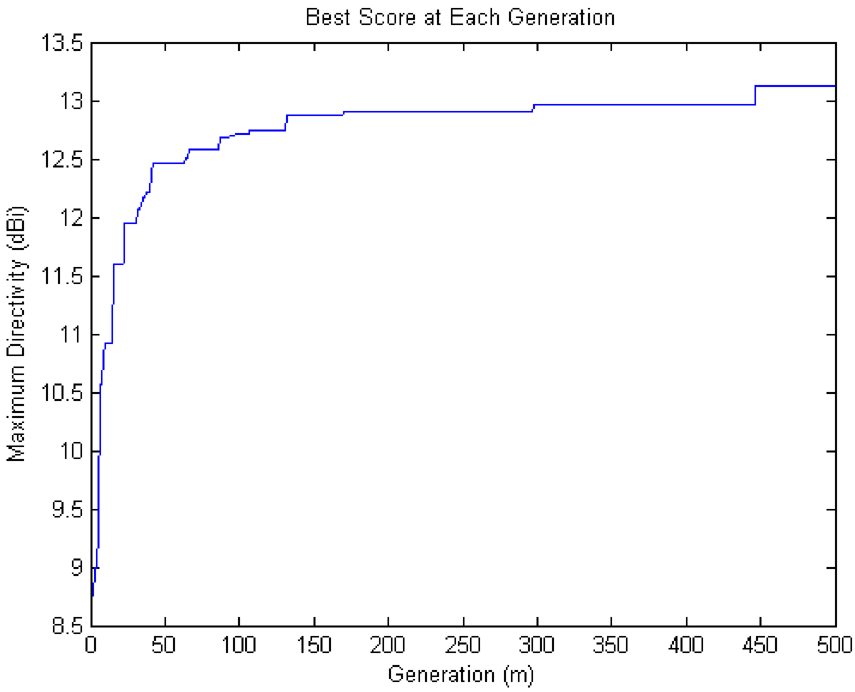

Figure 26. Convergence of CGA for 0° target angle.

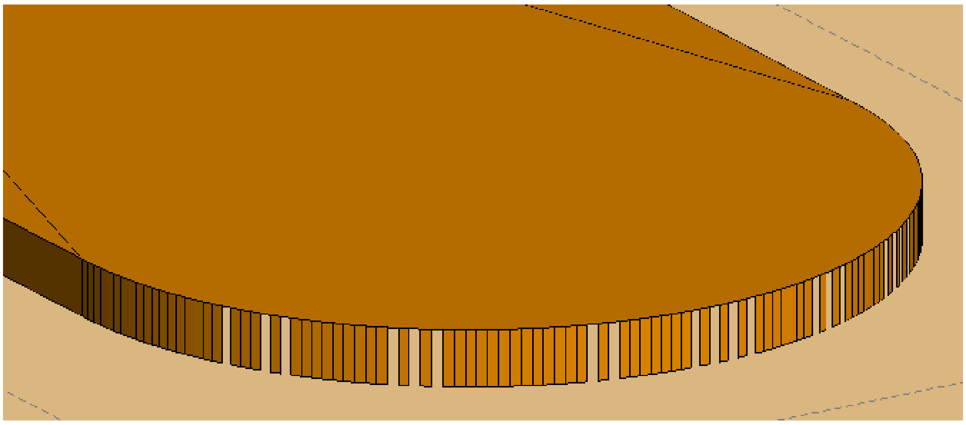

Figure 27. FEKO model of front radiation mask for 0°steering.

by the width of the main beam. The side lobe levels do, however, suggest that a more accurate model needs to be implemented for more advanced applications such as side lobe reduction or null steering.

In addition to verifying the accuracy for the broadside beam, it is also important to check that the model may also account for the case of a steered beam. This is done by importing the mask for a target angle of $-60°$ which is shown in Figure 29 to FEKO. The comparison shown in Figure 30 once again confirms that the model captures the primary facets of the main beam

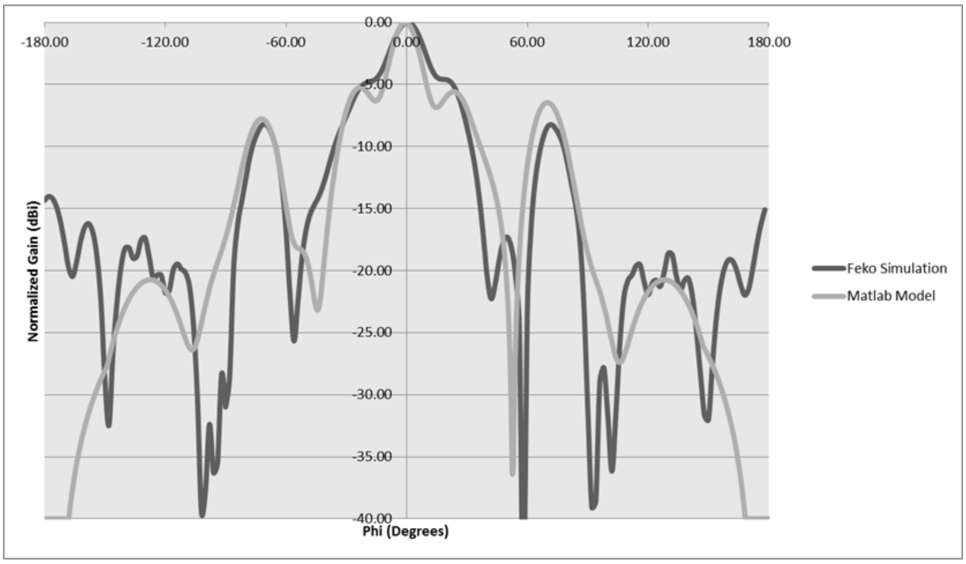

Figure 28. Comparison of Matlab model and FEKO simulation for 0°steering.

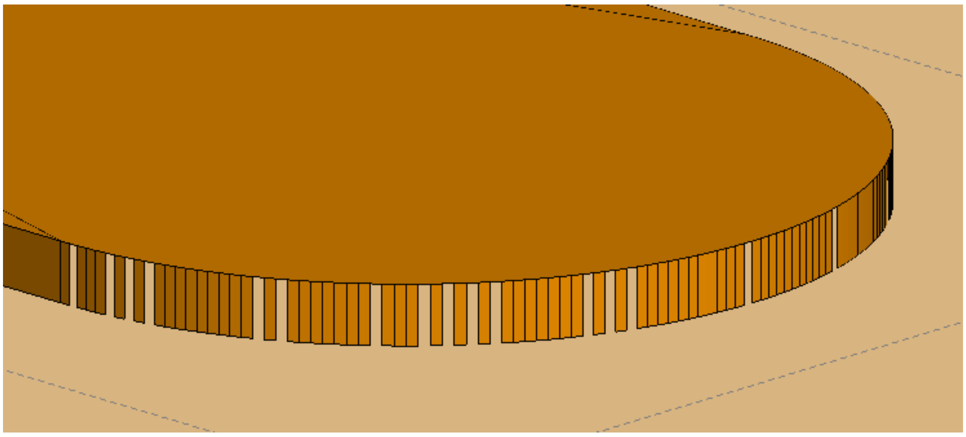

Figure 29. FEKO model of front radiation mask for -60°steering.

even as it is steered away from the broadside. As expected, the directivity and resolution does decay slightly as the beam is steered towards the edges.

3.6 Additional Curvatures

One of the key benefits of the CGA is that very few assumptions are made on the overall structure and thus it can be readily translated to additional curvatures. This translation is done by simply defining the curve, $\Gamma(x)$, associated with a given surface and then faceting surface and exporting the polygons to FEKO. FEKO then informs the surface currents that excite

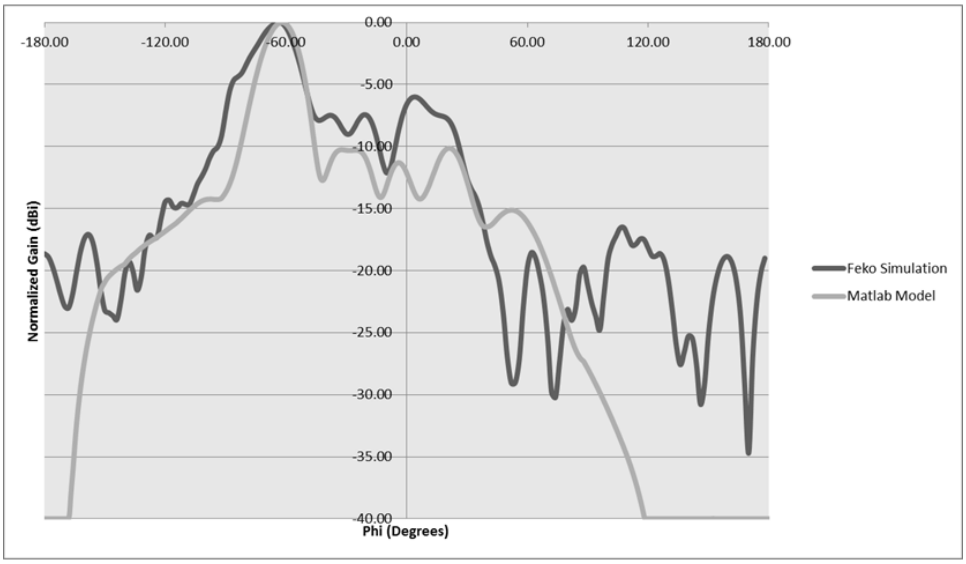

Figure 30. Comparison of Matlab model and FEKO simulation for -60°steering.

the structure which are translated back to Matlab. With the surface current information, the CGA can be repeated and additional surfaces modeled. The results of this process are shown in subsequent sections.

3.6.1 is also intended to show that the CGA may be utilized for shorter structures which are often preferred for conformal design. This preference is due to the compact nature of the structure being able to occupy tighter spaces and leave room for additional systems. Because the radiation of this conformal system is located on the front surface, this shorter structure does not hinder the overall directivity of the system as long as the width is maintained. These structures, however, would require short throw or specialized projection systems which can be built, but require specialized manufacturing ability, which is why the longer structure detailed in the previous sections will be built as a proof of concept.

3.6.1 Parabolic Cylinder

One structure of interest is a parabolic cylinder with the feed located at the focal point of the surface. To this end, the conformal surface

$$\Gamma(x) = 2\left[\frac{1}{4}\left(1 - \frac{x^2}{4}\right) + 0.1\right], \tag{3.39}$$

for $-2\lambda_0 < x < 2\lambda_0$, is selected and the feed point is placed at the point $(0, 0.1\lambda_0)$. This set up allows for a relatively even geometric optics contribution from the source current with the exception of on the edges of the structure. The resulting magnetic field and corresponding

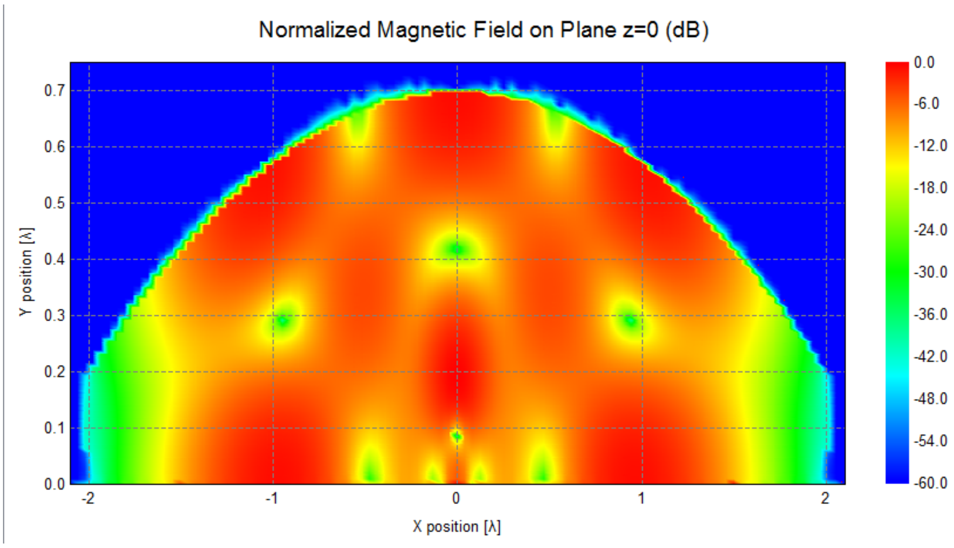

Figure 31. Normalized magnetic field for parabolic cavity ($z = 0$).

Target Angle	Directivity	Computation Time
-60°	8.24 dBi	23.10 s
-50°	9.74 dBi	23.3 s
-40°	12.04 dBi	23.4 s
-30°	13.57 dBi	23.2 s
-20°	14.32 dBi	23.3 s
-10°	13.27 dBi	23.5 s
0°	13.75 dBi	24.4 s
10°	13.11 dBi	24.4 s
20°	14.45 dBi	23.8 s
30°	13.49 dBi	23.6 s
40°	11.94 dBi	23.9 s
50°	9.84 dBi	23.5 s
60°	8.25 dBi	24.2 s

TABLE II

DIRECTIVITIES AND COMPUTATION TIME OF CGA FOR PARABOLIC SURFACE.

surface currents are shown in Figure 31 and verify that the illumination is indeed relatively even.

These surface currents are once again exported to a CSV file for the CGA to be run in Matlab. The resulting directivities and runtimes are shown in Table II which demonstrates that the surface has a significantly reduced gain past ±30°, which is expected because the parabolic surface does not have any faces in those directions unlike the circular cylinder. The resulting patterns are shown in Figure 32 which confirms the inability to steer much past 30 degrees, but clearly shows main beams within this range.

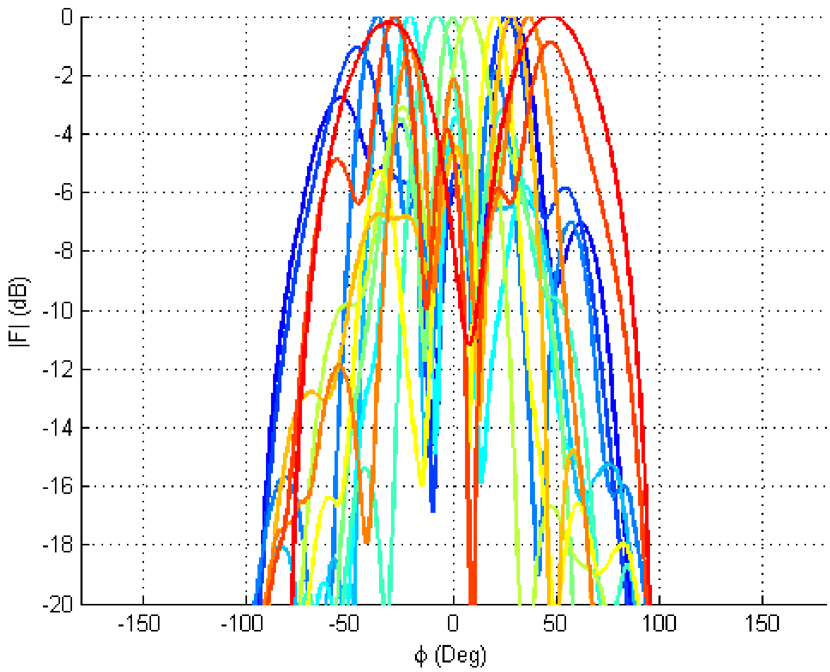

Figure 32. Normalized far fields for parabolic surface.

CHAPTER 4

PHYSICAL REALIZATION

The theoretical design of the conformal antenna requires validation through a functional prototype and experimental design. The focus of this chapter will be the physical realization of the system and the key components of the design which are required to achieve this. The system overview is demonstrated in Figure 33, which consists of an RF input signal fed into modified horn/sector antenna cavity. The aperture of this cavity is then covered with an optically tunable surface that is biased with a DC power supply and an optical projector to alter the radiation pattern. The resulting structure is shown in Figure 34.

Several design considerations must be taken with regard to each component in order to obtain a functional system. The optically tunable transmission surface must have a small enough unit cell to approximate an electrically small gap and be able to switch diode states based on the available illumination and power. The projector must be selected to illuminate and focus over the entire OT-MS. The antenna pattern and the masks must be designed to compensate for the curvature of the surface. The RF input, however, must be fed in such a way that it illuminates the surface evenly as well and is impedance matched to account for the reactance of the cavity. Lastly the horn must be design in such a way to fit these components into the prescribed form factor. These considerations will all be discussed in detail in this chapter.

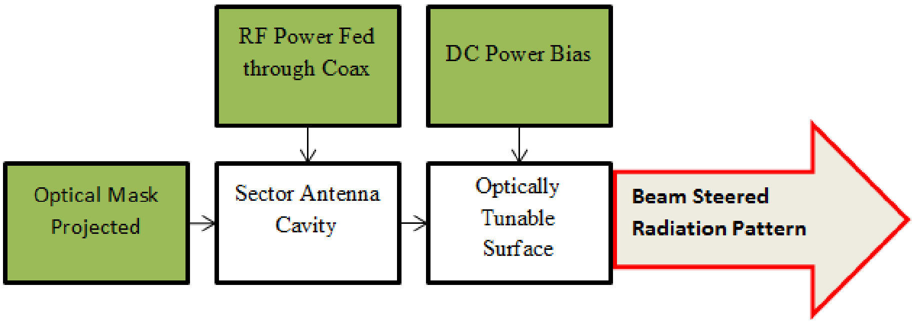

Figure 33. Block overview of the system.

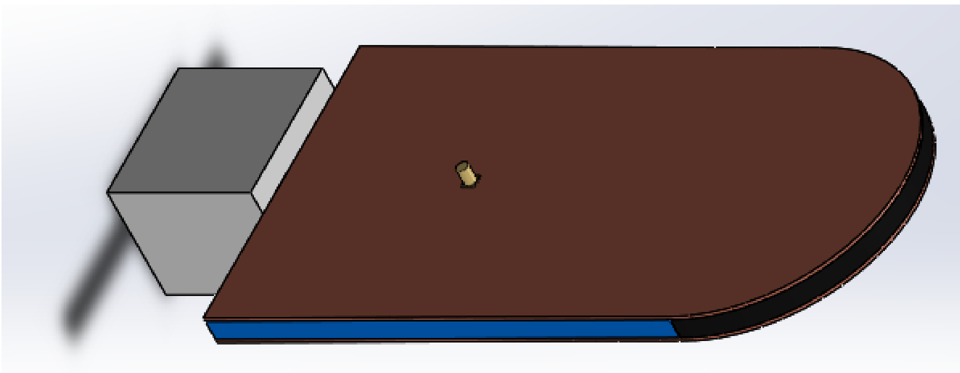

Figure 34. CAD model of system overview.

4.1 Tunable Surface

The first component of interest in the antenna system is the optically tunable transmission surface covering the aperture of the antenna [71]. This surface is designed based on a fundamental unit cell consisting of phototransistors and PIN diodes which are then tiled over the surface. The circuit schematic of this unit cell shown in Figure 35 utilizes KDT00030TR phototransistors which when illuminated, provide a 1 mA or greater current required to forward bias the SMP-1320 PIN diodes. The 100 $k\Omega$ resistors are then included to reverse bias the diodes when no current is flowing and thus reduce the junction capacitance. This system is powered by a 6V DC supply and the phototransistors allow the current to flow from this source when they are biased on but, block this current when not illuminated.

To the smaller RF signal, the non-linear components behave similarly to lumped elements and surface on which they are patterned also become associated with some level of reactance and resistance. As long as the unit cell remain electrically small, the key behavior may be modeled with a schematic that has three key components. The incident field from the RF_{in} port first encounters the impedance, Z_{pin}, which is associated with the PIN diode that follows either Figure 8 or Figure 9 based on whether or not the photodiodes are illuminated. Z_{surf} is the next impedance which is associated with the pattern of the copper surface of the periodic unit cell and is designed to optimize transmission at a given frequency or the tunability of the surface. Lastly, the system has a length of dielectric substrate L_{subs}, which acts as a transmission line with associated β and Z values before the RF signal is able to pass through the surface and transmit into the second region.

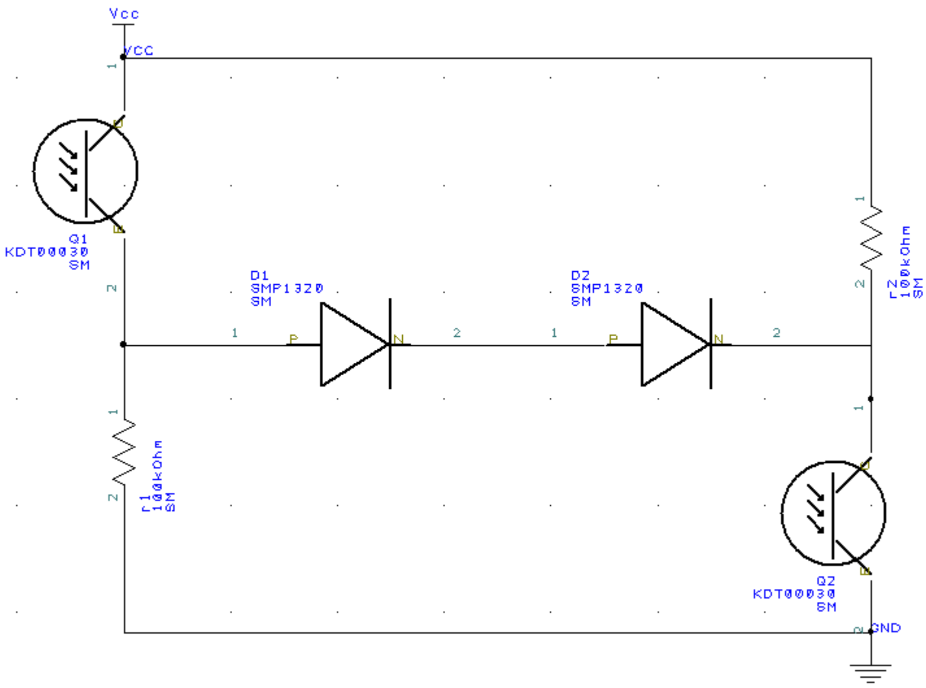

Figure 35. Schematic of mixed DC/optical biasing system per unit cell.

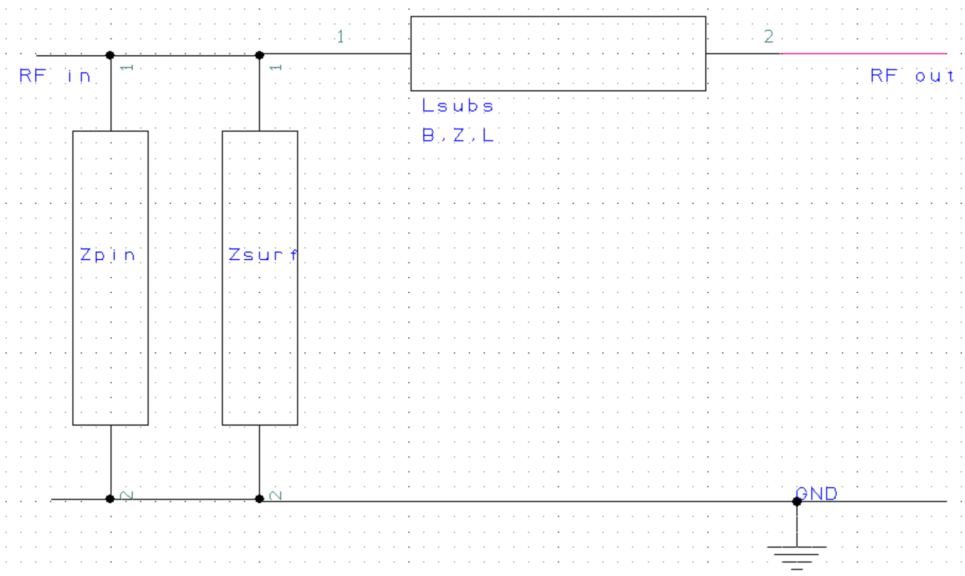

Figure 36. RF equivalent circuit of unit cell.

4.1.1 Simulation

The RF behavior of the tunable surface is modeled in HFSS [72] and the structure is patterned on .127mm thick RT6002 Duroid with a copper cladding thickness of 18μm. The periodic nature of the surface is modeled through the master/slave boundary condition and the structure is excited on either end using Floquet ports. The phototransistor, PIN diodes, and resistors are all modeled using the lumped element BC in HFSS with component values taken from the respective datasheets. For the SMP1320-079LF diode, the parameters are an on-state resistance of roughly 2Ω and an on-state inductance of 0.7nH. The off-state is modeled as a 1000kΩ resistance in parallel with a 0.33pF capacitance. These values are very important to the overall tunability of the system because they emulate the non-ideal behavior of the diode. The KDT00030TR phototransistor is modeled as a capacitance between 2 and 5pF for the ON and OFF states respectively, though these values are found to have less of an impact on the overall system performance due to the orientation of the transistor relative to the incident field. All lumped components are additionally modeled with blocks of silicon with the package dimensions and blocks of silver with the lead dimensions.

The system is model on .005" thick RT 6002 Duroid with 0.5 Oz (18μm) copper cladding. The board is patterned with the design shown in Figure 37 and the key dimensions are given in Table III. The structure is excited by an incident field traveling along the z-axis that is modeled via the Floquet port mode in HFSS in order to simulate the periodicity of the structure. The solder mask is included for aesthetic purposes but is left as a non-model component due to its relatively small impact on the overall structure. The simulation for the on and off states are

Label	Dimension	Description
W_{cell}	3.8 mm	Width of the unit cell
H_{cell}	10.18 mm	Height of the unit cell
W_{cen}	1.8 mm	Width of the center patch
H_{cen}	1.8 mm	Height of the center patch
H_{pin}	1.3 mm	Height of the pin diode
spc	0.1 mm	Gap between outer walls and pin diode leads for DC biasing

TABLE III

MODEL DIMENSIONS.

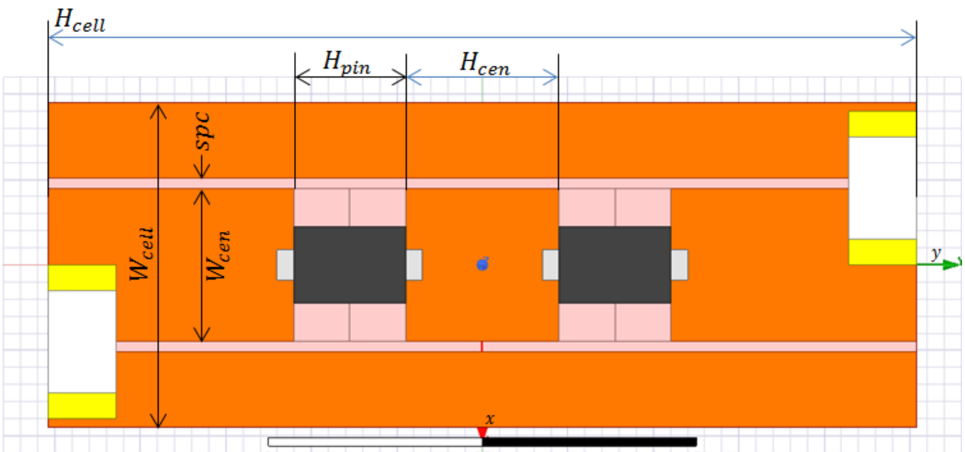

Figure 37. Unit cell model.

run separately in HFSS using three discrete frequencies at 8,10, and 12 GHz with a maximum delta S of 0.02 for two consecutive passes and a maximum number of fifteen passes with mixed order basis functions. The transmission and reflection parameters are then solved with an interpolating sweep from 8-12 GHz with 101 points.

Both the on and off-state simulations converge to the specified criteria in ten and twelve adaptive passes respectively. The resulting forward transmission through the surface for each state is shown in Figure 38 and the resulting tenability is shown in Figure 39. These charts show the system is very sensitive to the state of the PIN diode at 8 GHz with a resulting tunability of roughly 16 dB and the tunability goes down as the frequency increases and the non-ideal behavior of the diode becomes more of a factor. The system stil exhibits some tunability of around 5 dB at 10 GHz but at 12 GHz the diode switching is no longer sufficient to alter the forward transmission in a noticeable manner. This simulation also allows several other key parameters of the design to be extracted which will be discussed in the following subsections.

4.1.2 Oblique Incidence

The first key aspect of the unit cell structure is that since it will be curved to cover a conformal surface it will need to be relatively insensitive to oblique angles of incidence. The direction of propagation vector of the incident wave forms the angle θ_0 with the z-axis and propagates in the xz plane. Because the gap size in the surface is roughly 2 mm, it is on the order of $\lambda_0/20$ from 8 to 10 GHz, which meaning the transmitted field is expected to be roughly proportional to $\cos\theta_0$. The relative transmission over angles of incidence are shown for the PIN-OFF and PIN-ON cases in Figure 40 and Figure 41 respectively, with the dotted

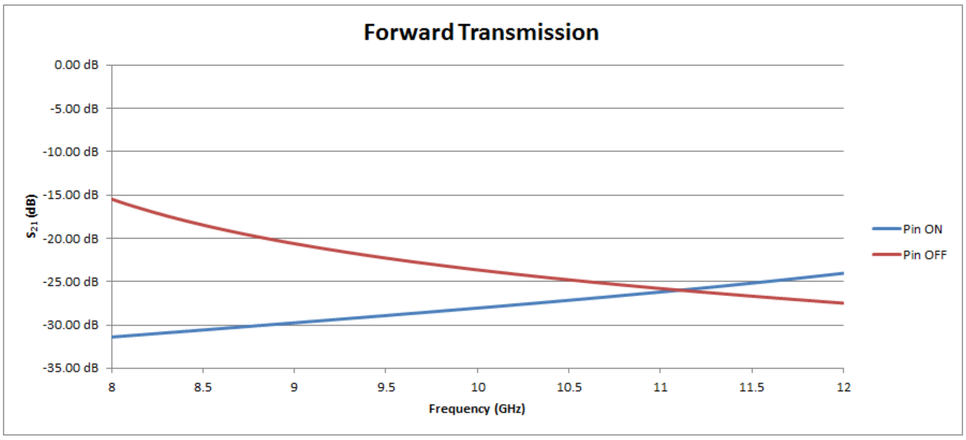

Figure 38. Forward transmission of the metasurface.

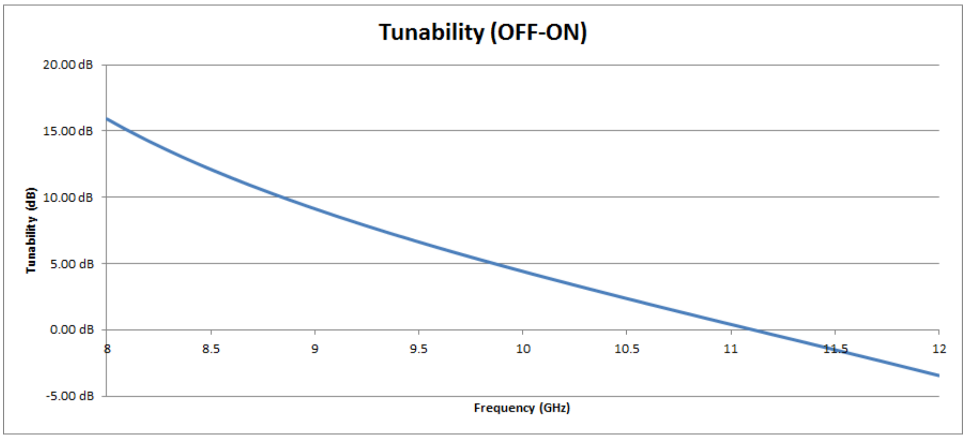

Figure 39. Forward transmission tunability.

lines representing the expected $\cos\theta_0$ value. The surface follows this $\cos\theta_0$ behavior over most frequencies in both the PIN-ON and PIN-OFF states except for around 8 GHz in the pin off state. At this frequency the system is near a resonance of the surface that allows for an increase in the transmission magnitude at the cost of some of the electrically small behaviors of the structure. This resonance however is partially responsible for the tunability of the system a 8 GHz so while the oblique behavior may be improved by making the structure smaller, this has a negative impact on the tunability of the surface. The dependence on $\cos\theta_0$ still roughly holds so the model is still usable. It should also be noted that relative errors on a linear scale have a larger effect on the simulation at oblique incidence due to the relatively smaller transmission coefficient.

4.1.3 Mutual Coupling

The next important parameter to extract from the simulation data is the mutual coupling between adjacent unit cells. The mutual coupling is particularly important for the conformal array design because if the coupling between adjacent diodes is small, then either one of the key assumptions of the CGA would be violated. Further limitations on the pattern selection would need to be imposed in order to ensure that the couling between cells does not alter the radiation pattern. Because of the electrically small nature of the cell, the coupling between adjacent cells may be assumed to decrease as cells move farther away from one another. This means that if the coupling between two adjacent cells is small enough, then further cells are a lower concern to violate the CGA assumptions.

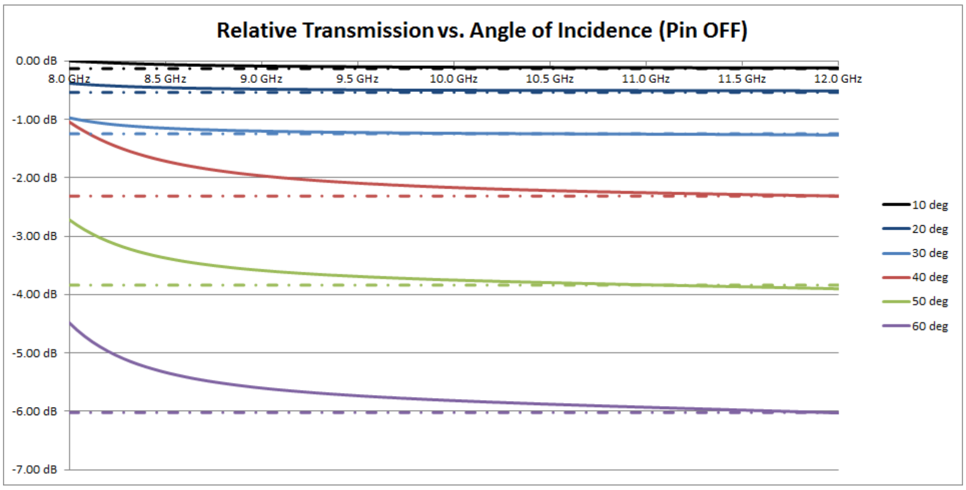

Figure 40. Forward transmission over oblique incidence with PIN-OFF (transmission allowed).

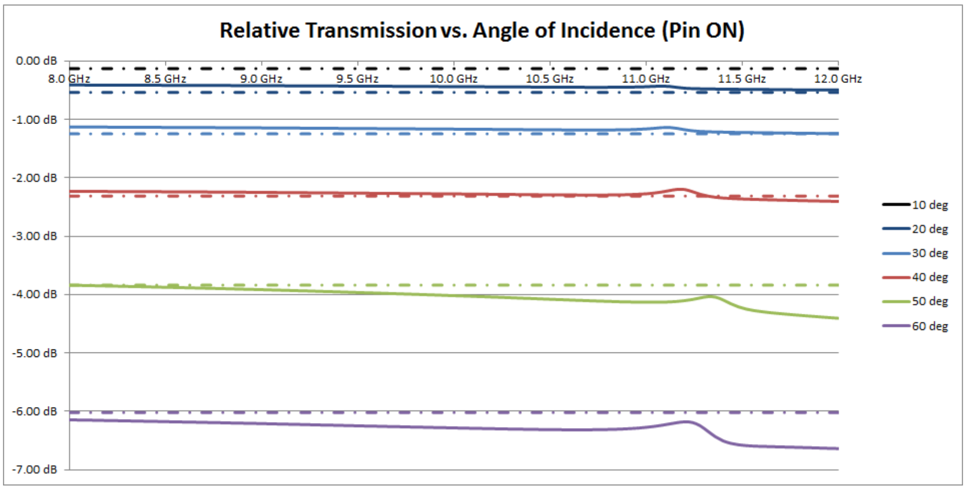

Figure 41. Forward transmission over oblique incidence with PIN-ON (transmission blocked).

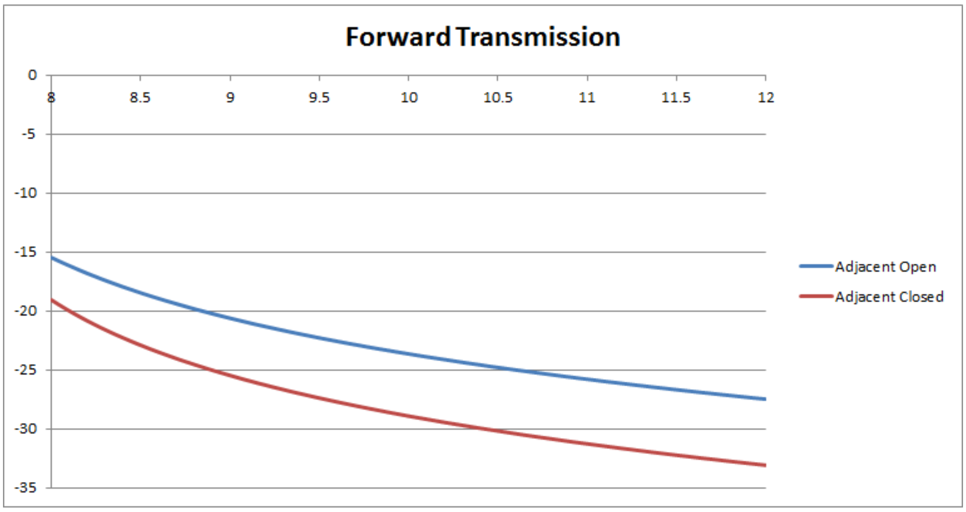

Figure 42. Forward transmission with varied cell size.

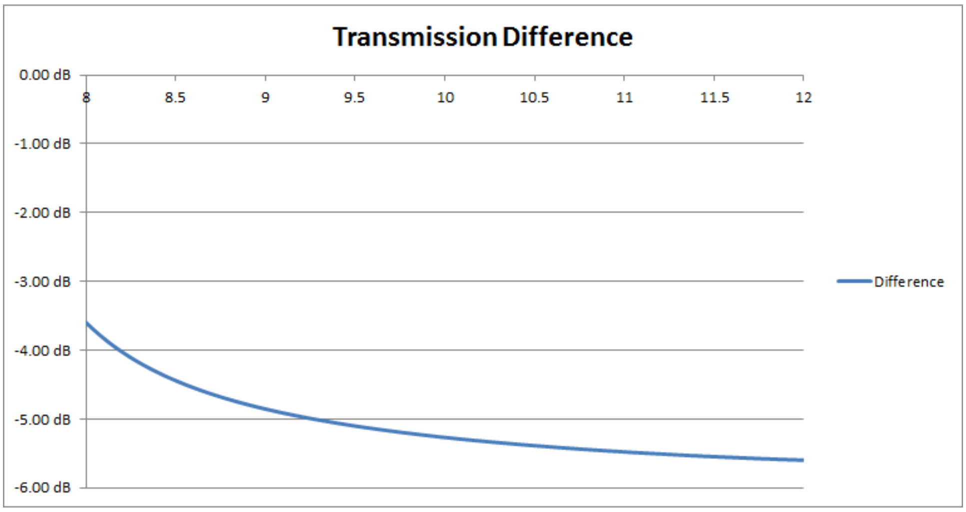

Figure 43. Difference in forward transmission.

The mutual coupling between cells may be validated through the HFSS simulation using the parametric analysis option. For this set up the W_{cell} parameter may be increased by powers of two, where the case $W^{*}_{cell} = 2^{n}W_{cell}$ models the coupling between the first $n-1$ cells on either side. If the mutual coupling between adjacent cells is small, then for every doubling of the cell spacing, it is expected that 6 dB is reduced in the forward transmission of the surface. The effect of doubling this spacing is shown in Figure 42 with the difference between the two shown in Figure 43. It can be seen that at 8 GHz there is still some coupling between the adjacent cells such that the forward transmission is only reduced by 3.5 rather than 6 dB. Since this reduction is still below the half power point, the overall effect on the maximum directivity pattern is neglegible. For cost functions where precision is a concern, such as side lobe reduction or null steering, the mutual coupling needs to be modeled in the CGA.

The reason that the mutual coupling is sizeable at 8 GHz and reduced at 12 GHz, may be seen in the surface currents shown in Figure 44. At 12 GHz the surface currents are tightly bound to the edges of the gap, meaning that the magnetic field present over the surface of adjacent cells is relatively small, while at 8 GHz, the field spreads further along the surface. When these surface currents are interrupted by gaps, they create notable equivalent sources which create the coupling effect defined in Equation 2.9.

4.2 Pin Diode Parameters

A number of limitations on the surface behaviors are primarily related to the non-ideal parameters of the SMP-1320-079 PIN diodes. These diodes function at exceptionally high frequencies for their relative costs, but they are also relatively ineffective above 10 GHz. For

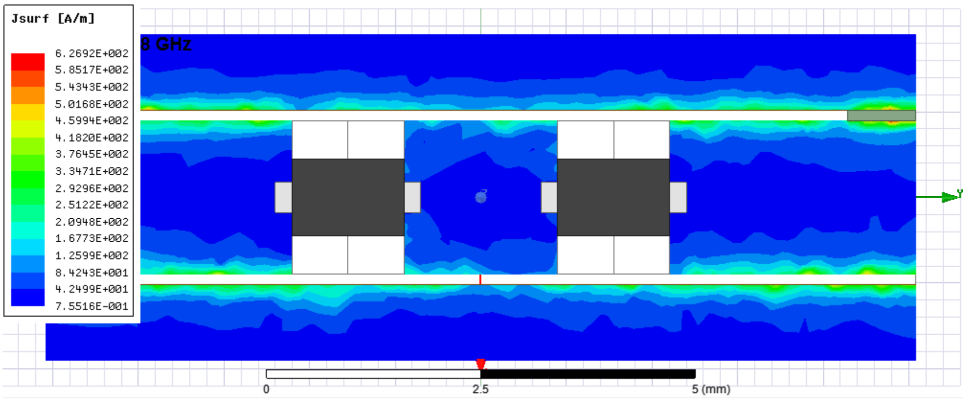

(a)

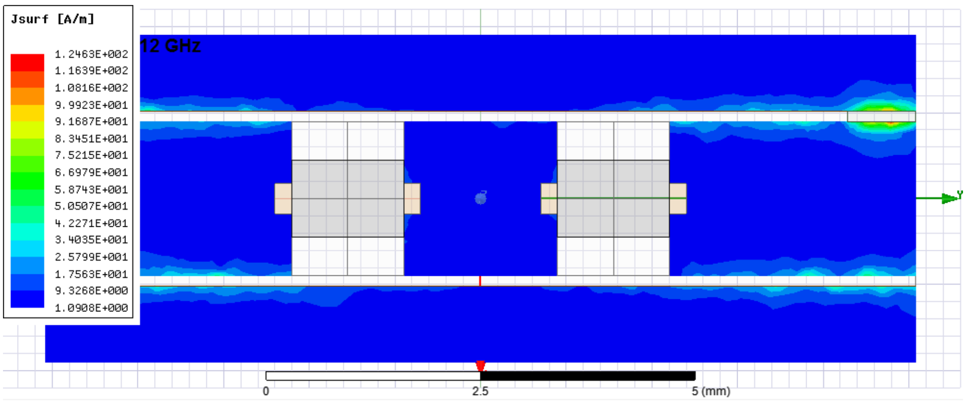

(b)

Figure 44. Surface currents on surface at (a) 8 GHz (b) 12 GHz.

more ideal behavior, high end PIN diodes may be used such as the MACOM MA4FCP200. This diode has a miniscule junction capacitance of .02 pF and a negligible series inductance at 12 GHz, which allow them to function effectively up to 40 GHz. The main drawback to these diodes, however, are that the MACOM diode costs $1.83 each while the SMP-1320 diodes are only $0.24 each. This means that a 64 element array of gaps requiring 2 pins each would cost $235 while the same surface with the SMP diodes is only $31. These diodes however can be simulated in HFSS by replacing the lumped element parameters in order to demonstrate the future potential of this surface as the cost of high frequency components are reduced. To this end, similar tests are run with the SMP diodes and the relative behavior is discussed.

The first significant improvement of the updated PIN diode is that the tunability of the surface is increased as shown in Figure 45. This tunability comes as a result of increased transmission magnitudes at higher frequencies because of the reduced capacitance as well as reduced transmission in the closed state at all frequencies due to the smaller inductance of the surface. The transmission is most improved near 10.2 GHz where the surface is resonant and becomes transparent to the incident wave. A high transmission coefficient is important for conventional transmitarrays where any reflected power is lost, but this is less of concern for the present system because of the enclosed nature of the structure which results in reflected power being stored as complex impedance. This large transmission magnitude results in the maximum tunability of the surface of 74dB at 10.2GHz . With the improved PIN diodes, the system is tunable to 60dB at 8 GHz and demonstrates this tunability throughout the 8-12 GHz frequency range. This range of the spectrum is common in satellite television applications, but

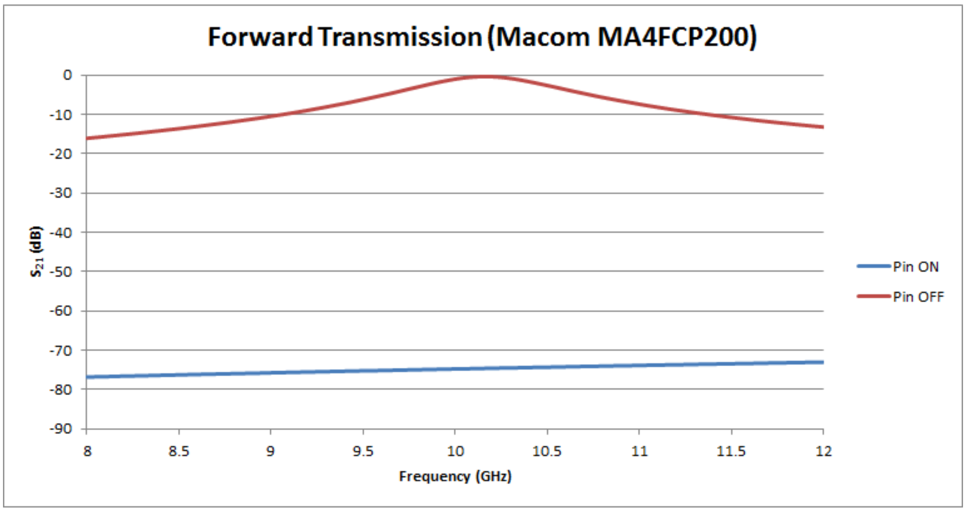

(a)

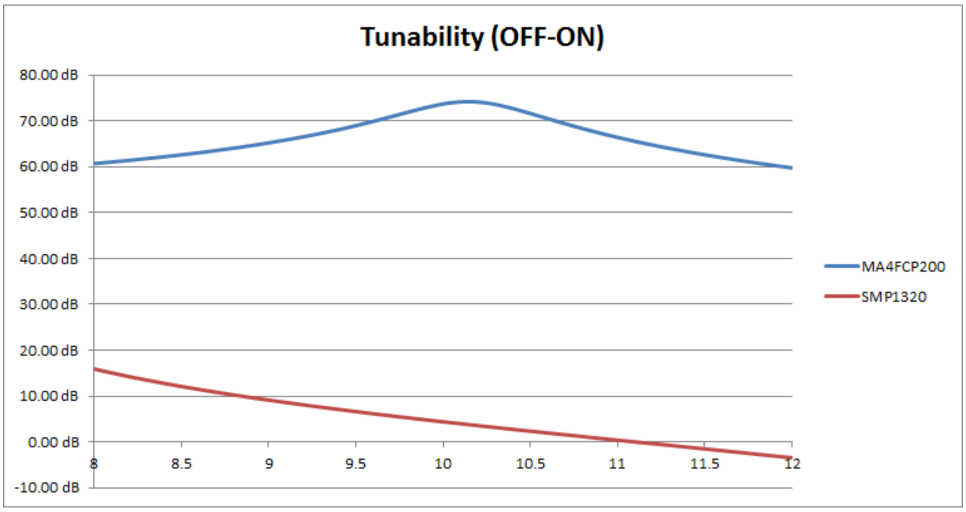

(b)

Figure 45. Surface transmission characteristics with updated diode: (a) forward transmission with Macom pin diode (b); surface tunability with Macom pin diode (SMP1320 shown for reference).

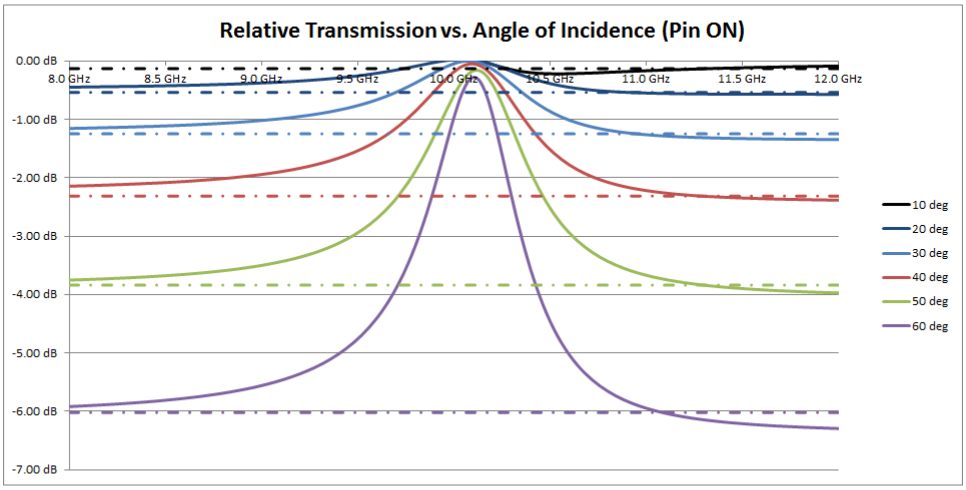

Figure 46. Forward transmission over angles of incidence.

also suggests that the surface may be adapted to higher or lower frequencies such as the 5-6GHz range for WLAN and 4G/5G communications base stations or up to 24 GHz for use in mm wave 5G systems.

The simulations with the improved PIN diodes are also useful to yield additional information on the non-ideal behaviors of the surface that are present with the lower cost diodes. The first noteworthy trend can be shown in the relative transmission at oblique angles of incidence. The behavior of the forward transmission coefficient vs. the angle of incidence is shown in Figure 46. This figure shows that the surface follows the $\cos\theta_0$ dependence at 8 and 12 GHz, where the surface is not resonant, but this dependence does not hold around 10 GHz where the surface is resonant and has near total transmission at 10.2 GHz. At this frequency, the transmission is nearly independent of the angle of incidence which would require a different model than that used by the CGA in 3.4.1.

The next phenomenon is will be further explored with the updated Macom Diodes is the mutual coupling between unit cells. A similar procedure to that described in 4.1.3 is implemented to study the mutual coupling between unit cells. Similar to the case of the SMP1320 PIN diode, the surface with the updated PIN diode demonstrates effective decoupling except near the resonant frequency of the surface. This relationship is shown in Figure 47, showing that the cells are somewhat decoupled, except near the resonant frequency of the structure. There is also a shift in the resonant frequency that causes the transmission to increase at 10.5 GHz when the PIN spacing is altered.

4.3 Experimental Design

The HFSS simulation results are verified through an experiment designed to test the transmission and optical tunability of the designed surface. To this end, a board is designed consisting of six unit cells arranged horizontally which is shown in Figure 48. This board has a total surface length of 22.86mm which may be placed over the surface of a WR-90 waveguide cross section. The surface is then placed over port 2 of a WR-90 directional coupler. An optical source (e.g. flashlight) is placed over port 1 and port 3 is left for an incident field to be generated. The system is tested by placing a VNA on port 2 and 3 to measure the transmission through the surface as a function of frequency. Additionally the surface is biased with a DC power supply

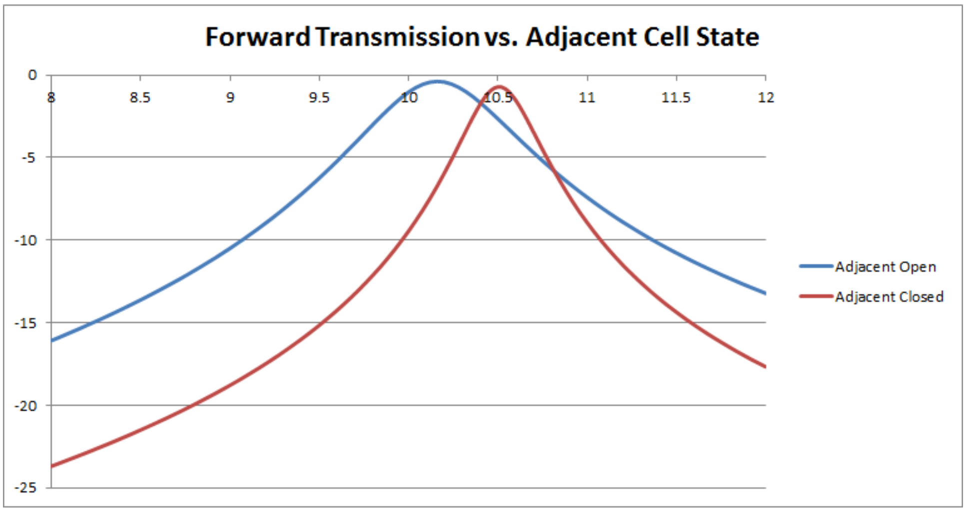

(a)

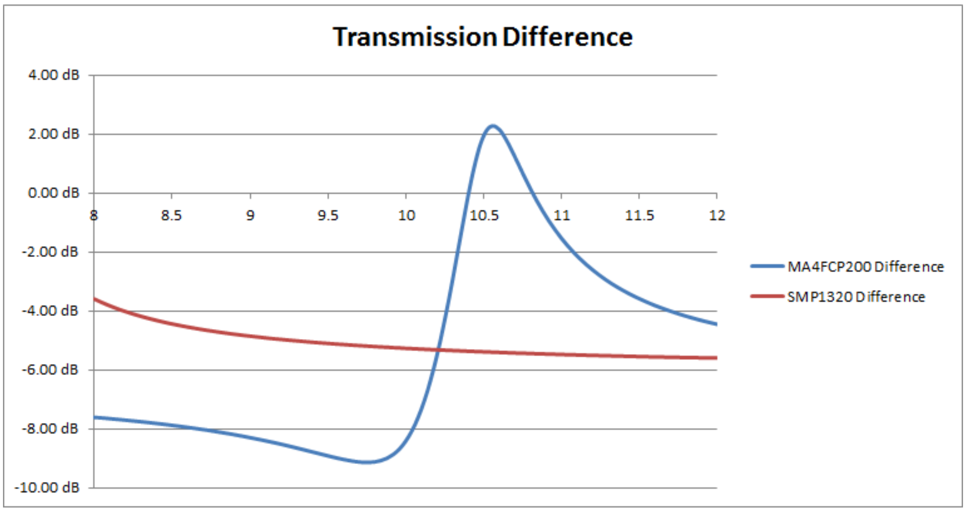

(b)

Figure 47. Forward transmission at varied pin cell spacing: (a) relative magnitudes; (b) comparison with SMP1320 surface.

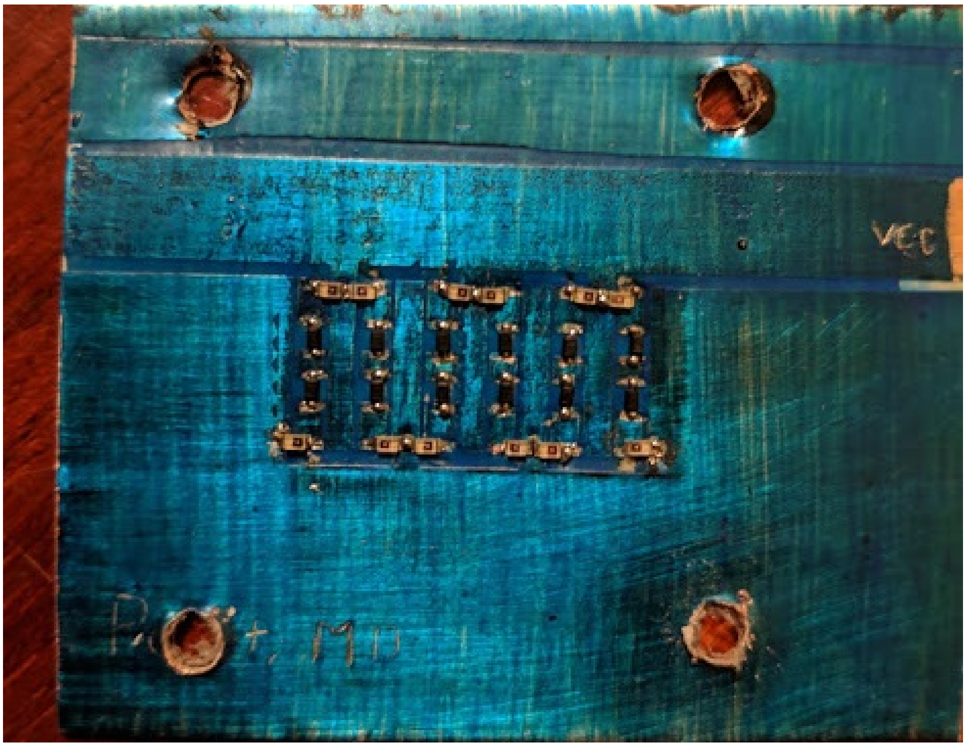

(a)

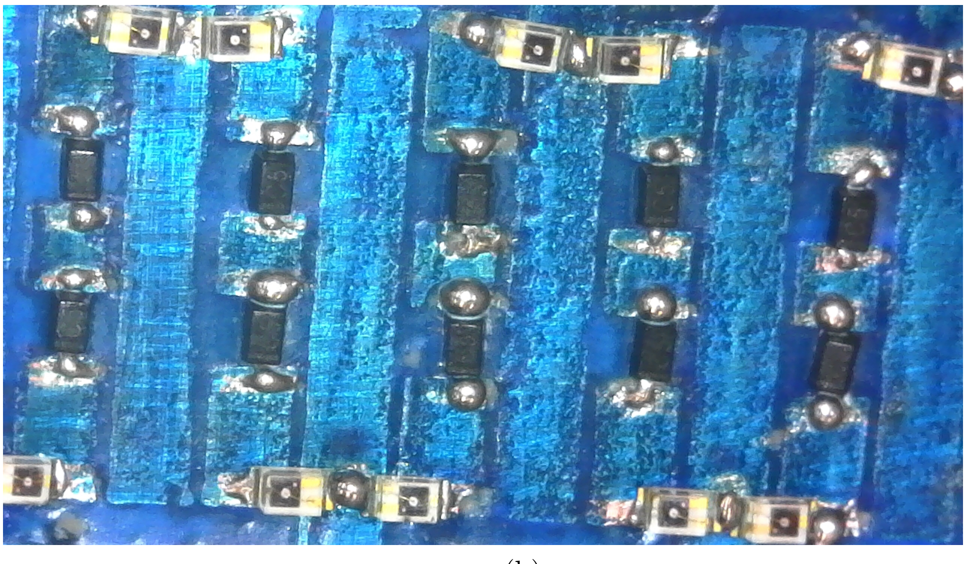

(b)

Figure 48. six-unit cell board to be placed over the WR-90 waveguide surface: (a) full board; (b) soldered components under microscope.

set to a voltage of 3.2V in order to be sufficiently large enough to bias the PIN diodes without applying excessive voltage across the phototransistor when the system is off.

This set up is shown in block diagram form and the physical set up is shown in Figure 49. The WR-90 directional coupler is operational beginning at 8.2 GHz, meaning this test does not effectively extract the tunability of the structure below this range. This lower frequency bound is set for a variety of reasons including, but not limited to, the fact that at lower frequencies the guided wavelength is relatively large which means that the isolation and directivity of the coupler are reduced to such an extent that near field effects can have a disproportionate effect on the structure. The guided wave in the WR-90 section can also be considered as the superposition of two obliquely incident plane waves on the tunable surface. The angle of incidence of these two plane waves may be computed from the equation

$$\theta_0 = \sin^{-1}\left(\frac{\lambda_0}{2a}\right), \tag{4.1}$$

where λ_0 is the free space wave length and $a = 22.86mm$ is the width of the waveguide cross section. At 8.2 GHz this results in an incident angle of roughly 53°which is within the expected range to show the sinusoidal dependence on the angle of incidence for both the transmission allowed and blocked-states of the surface. Towards the lower end of the frequency range, the variation in the sinusoidal dependence will cause some errors in the tunability measurement. Because this sinusoidal dependency is present in both states above 9 GHz and should not have a significant effect on the overall tunability measurement. It should also be noted that

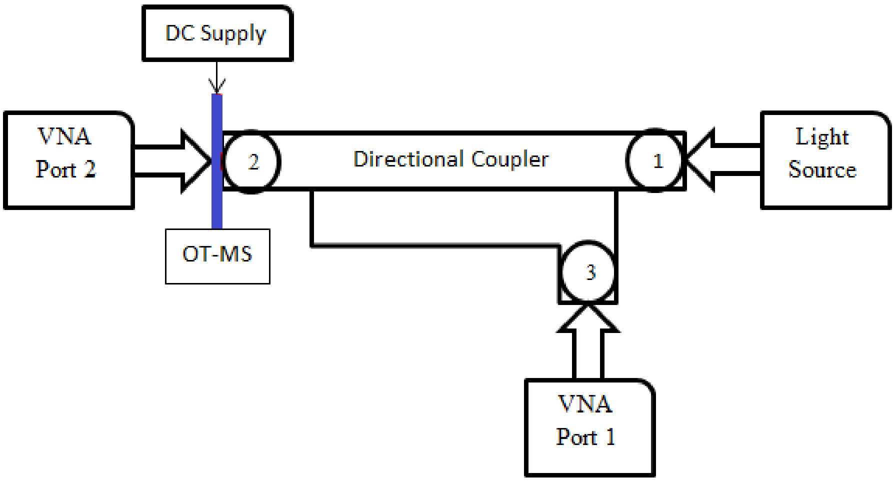

(a)

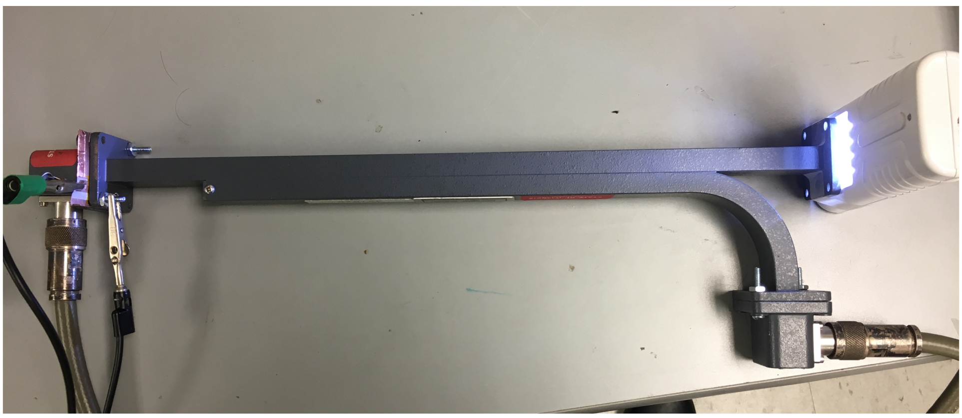

(b)

Figure 49. Optical tunability test set up: (a) block diagram; (b) physical set up.

at incident angles near 90°(i.e frequencies near the WR-90 cutoff frequency), the sinusoidal dependence may result in measurements that are too small for the VNA to measure or are masked by imperfections such as gaps between the tunable surface and the waveguide walls. In order to ensure that the small transmission values are not an issue, this experiment is only reported for frequencies from 8.2-12 GHz in the following section. All measurements are carried out in the Andrews Electromagnetics Laboratory on the UIC campus.

4.3.1 Experimental Results

The following procedure is carried out in order to obtain experimental data for the surface tunability. First, the set up is built using a Keysight N5222A VNA with type N to WR-90 adapters on either port. Then the surface is connected to an Agilent U8002A DC power supply that is set to a maximum voltage of 5.0 V and a maximum current of 100mA in order to bias the surface without risking damage to the PIN diodes or phototransistors. No calibration is carried out since the primary focus of the experimental measurement is on the difference in transmission rather than the absolute number.

To measure the difference in transmission, the set up is placed in a stable position with the light source switched off and the S_{12} measurement is taken with a RBW of 100 Hz, with an output power level of 20 dBm to reduce the noise on the screen due to external sources. The trace is then stored with the max store option. Next, the light source is switched on and shown on the same screen using a second trace in order to show the transmission on the same scale to demonstrate tunability. It should also be noted that when the light is switched on, the DC supply measures and output of 20mA, meaning that each PIN is biased with a roughly 3mA current. Next the process of switching the light on and of is repeated with an average taken over 50 measurements and the data for each case is exported to s2p files for processing.

The resulting quick transmission measurements are shown on the VNA screen in Figure 50 along with the processed tunability that may be compared with the simulation results. From these figures, it can be seen that the surface tunabilitty is slightly lower than expected towards the low end of the frequency range, but it performs better than expected from 9-10 GHz. The tunability also continues up to nearly 11 GHz which is in line with the simulation data. If more precise information is needed the simulation model may be updated with measured equivalent circuit values and updates of the photodiode model as well. For this system, the primary interest of the surface is to have a broadly tunable ON and OFF-state which this experimental result demonstrates and thus, it is sufficient for implementation.

4.4 Horn Construction

Following this validation, the next step is to construct and validate the overall system and the design results of the CGA. To this end, the overall horn system must be constructed. In order to reduce weight and cost, the horn structure will be constructed using polymers and coated with a layer of copper tape to create the conductive walls. The horn is split into four primary parts for this construction.

The first part of the construction is the top and bottom faces of the horn antenna, which are laser cut from acrylic sheets and the interiors, which are coated in copper foil. Next, the side walls of the horn are constructed using 3D printed PLA and also wrapped with copper tape. The third section is the 64 element OT-MS, which is etched on .005” RT6002 Duroid and

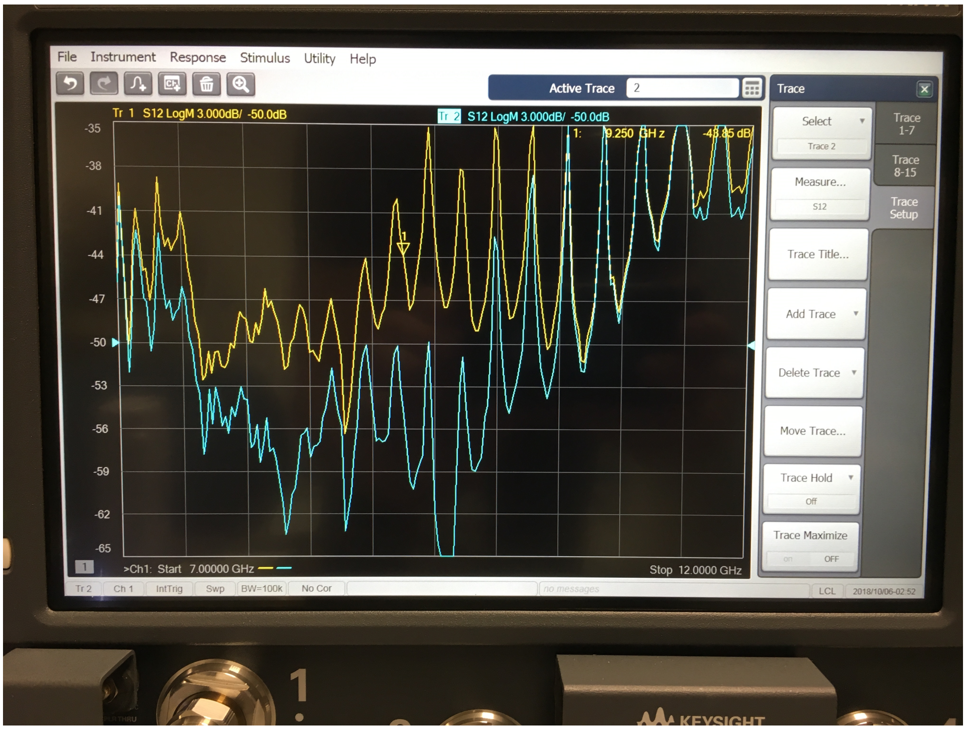

(a)

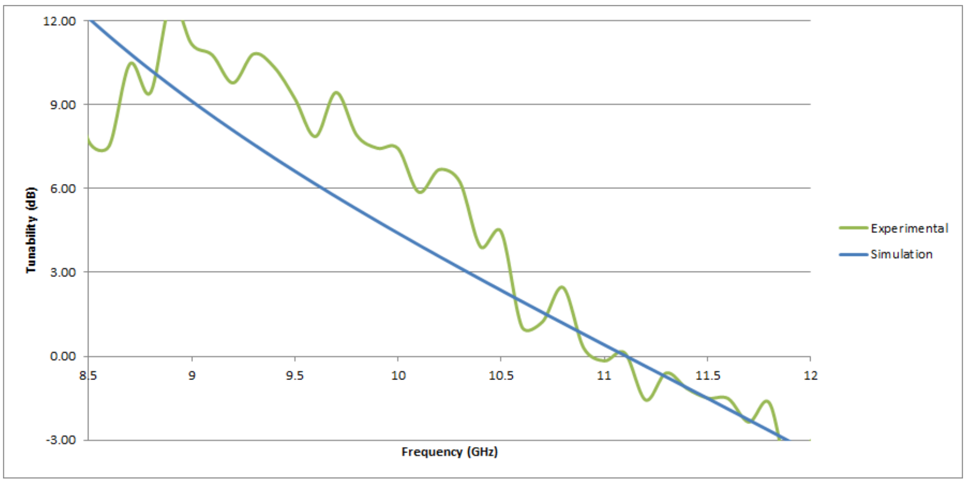

(b)

Figure 50. Transmission measurements: (a) on VNA screen; (b) tunability comparison between measured and simulated data.

soldered by hand. The last piece is the optical projector, which is placed on the back of the horn and mounted using a 3D printed PLA fixture.

4.4.1 Top and Bottom Sections

The top and bottom of the sector horn antenna are laser cut from .1” thick acrylic using a Universal Laser Systems VLS 60 laser cutter. These parts are modeled using Solidworks 2018 and the face to be cut is exported using the DXF export option in solidworks. The resulting DXF files for the top and botom sectors ref shown in Figure 51 and include holes for mounting an SMA plug as well as holes for number 8 machine bolts which are utilized to align the tops with the side walls. The resulting cut parts are shown in Figure 52. One drawback of coating the part rather than cutting it from a sheet directly is that air bubbles form between the copper and the acrylic. These bubbles however have a relatively low profile so they should not excessively perturb the vertically polarized incident field. The bubbles can, however, slightly alter the projected image.

4.4.2 Horn Edges

The next key features for construction are the corners of the horn antenna. These corners are designed with Solidworks 2016 and then exported to a STL file for 3D printing and sliced using Ultimaker Cura V. 3.2.1. The part is printed on a Creality CR-10 printer using PLA plastic on a heated bed to prevent warping. The interior is designed to be hollow except for two holes to attach the walls to the top and bottom of the structure. In order to save material, the outer walls of the PLA structure are coated with copper tape and affixed to the structure using number 8 bolts. The resulting product is shown in Figure 53.

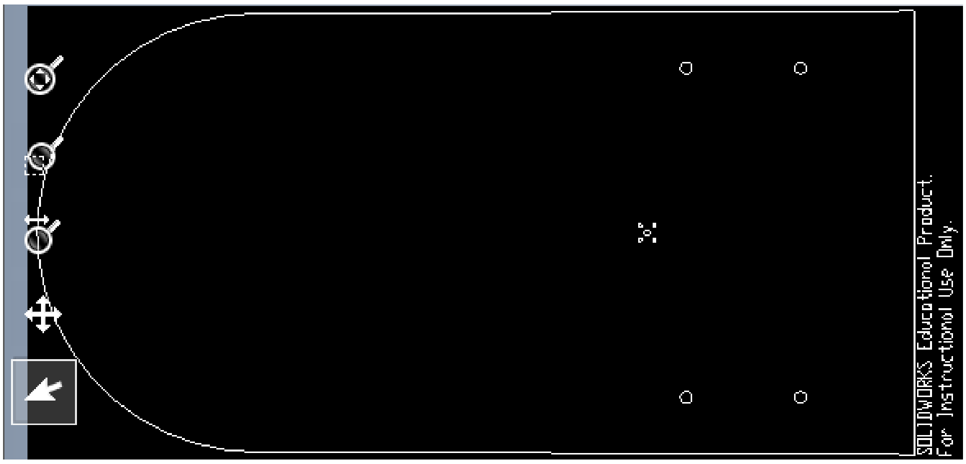

(a)

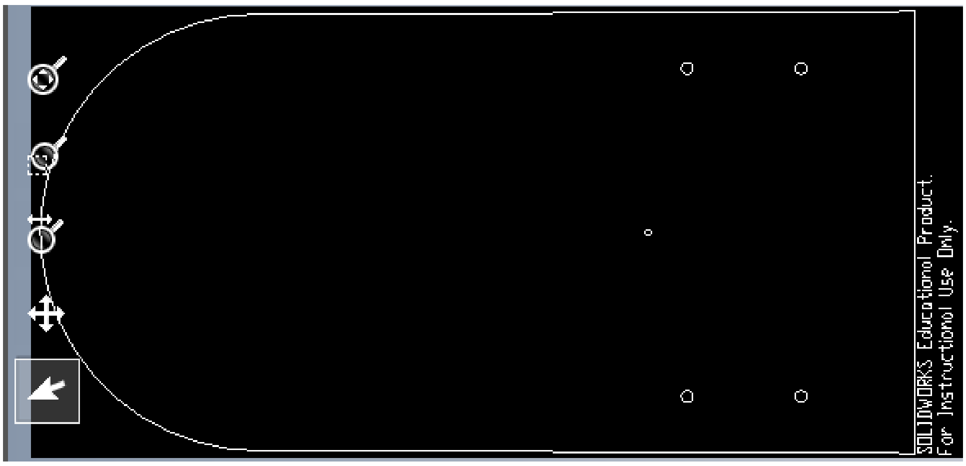

(b)

Figure 51. DXF files of sections for laser cutting: (a) top; (b) bottom.

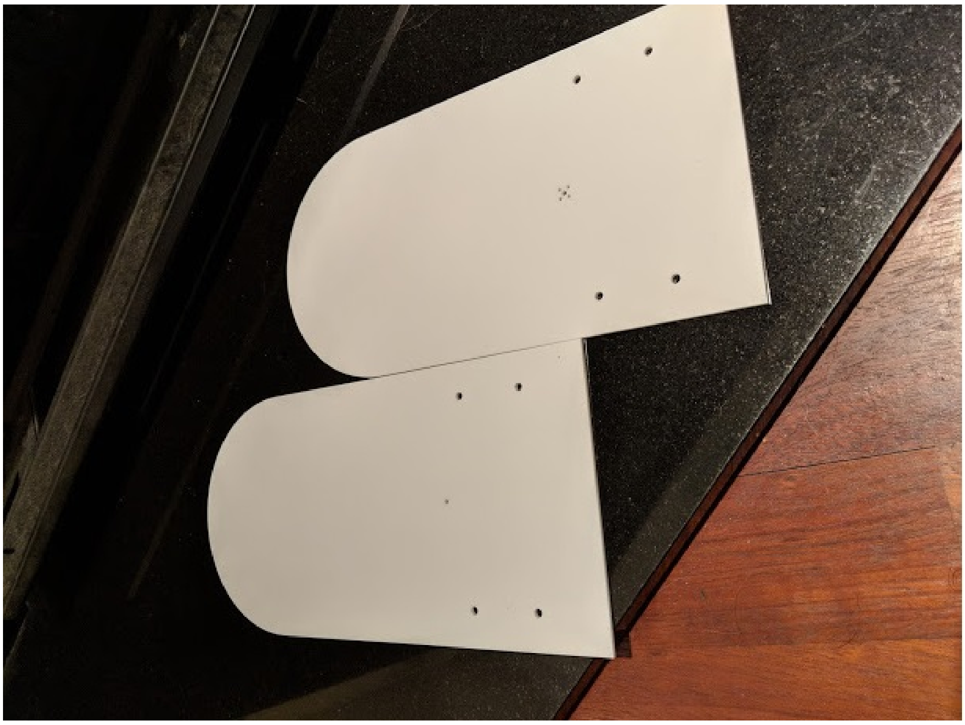

(a)

(b)

Figure 52. Laser cut horn top and bottom sections: (a) only acrylic; (b) coated with copper tape.

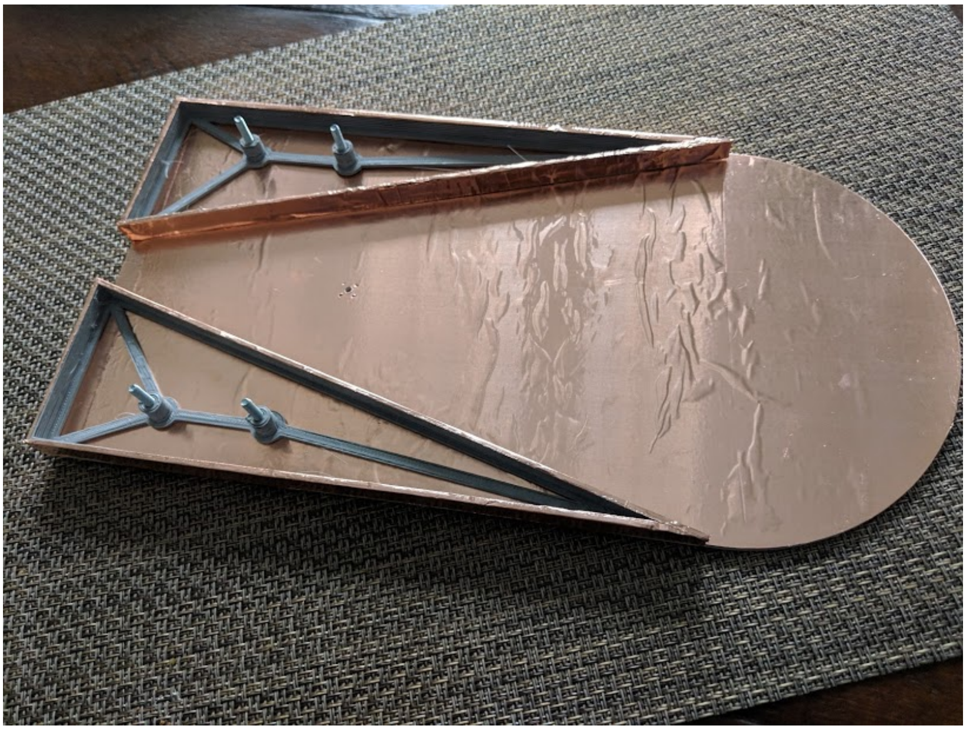

Figure 53. 3D printed walls affixed to top laser cut section.

4.4.3 Optically Tunable Surface

The major component of the fabrication process is the optically tunable surface which is patterned on a flexible substrate of .005" thick RT6002 Duroid. This fabrication must be competed in several key steps and then checked regularly to ensure that all of the unit cells are functioning properly. To this end, the board is designed using DesignSpark PCB 8.1 and is then transferred to a PDF, which is printed on overhead transparency paper using a Canon Laser Printer. This toner pattern is then transferred onto the copper clad RT6002 Duroid using a clothes iron. Errors in the toner transfer are remedied by hand with either a sharpie pen or scotch tape to add copper to the pattern or an exacto knife to remove toner. The board is then etched using ferric chloride and the excess toner is removed but some toner is left on areas which will not be soldered. A layer of UV curable solder mask is then applied to the board and the pattern for the PIN diodes and phototransistors are cut by hand using an exacto knife. Lastly, the 128 PIN diodes and 128 phototansistors are hand soldered to the board under a microscope. These steps are shown in order in Figure 54.

Because these steps are carried out by hand, it is important to test each cell to ensure each one is functioning properly. These checks are performed primarily with various functions of a DC multimeter to ensure that the cells may be biased properly. The first key test is for continuity between power and ground to ensure that no short circuit exists on the board. Then, each pair of diodes is tested with the diode test on the multimeter to ensure that current can flow. Lastly, the board is powered with a DC power supply set to a max voltage of 4V and a max current of 100mA. Light is then shined on each unit cell and the voltage across the

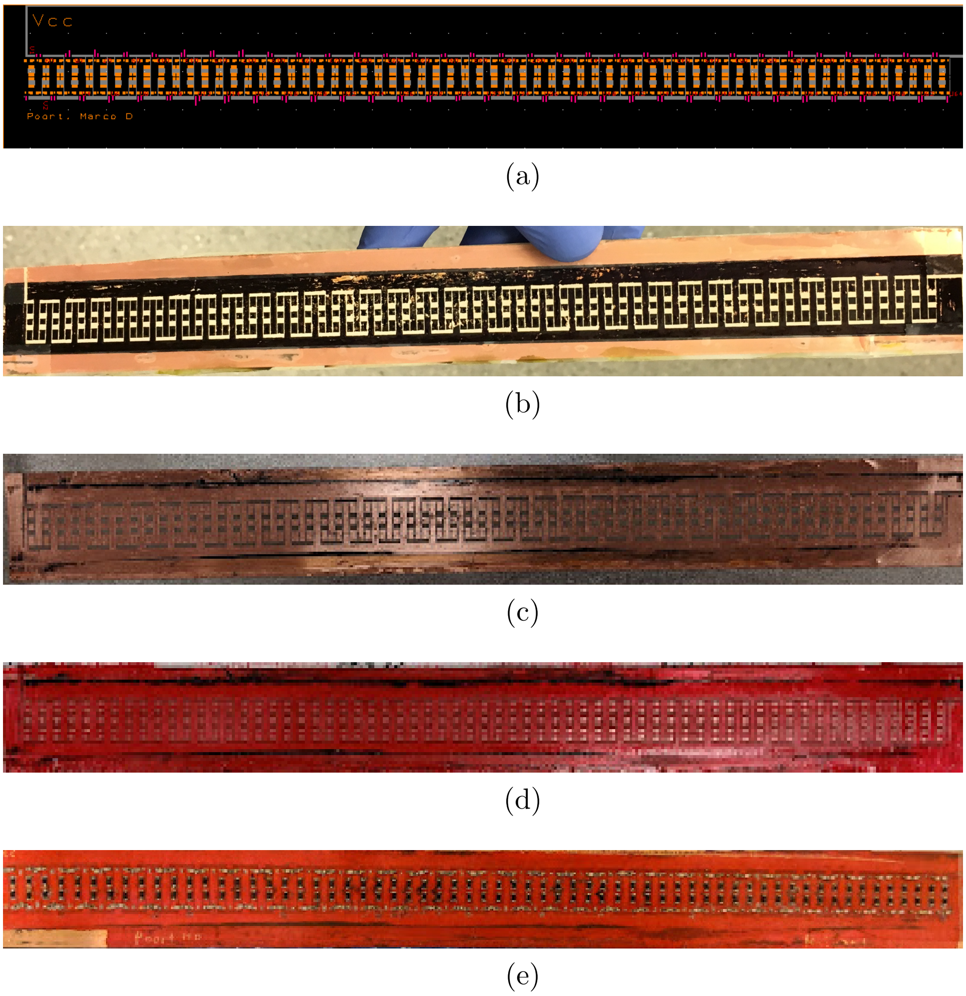

Figure 54. Optically tunable surface fabrication from top to bottom: (a) PCB layout on CAD software; (b) tone transfer; (c) etched board; (d) hand cut solder mask; (e) final soldered assembly.

pin diodes is measured to ensure that current is flowing properly through the cell. Any cells in which errors are found are marked with a wet erase marker and then examined under a microscope for repairs.

4.4.4 Projector and Optical Mask Design

The final major step of the fabrication process is to mount the AAXA P2-A pico projector to the sector antenna and design the optical masks. The projector is set to the maximum brightness and contrast in order to create a sharp light/dark pattern needed for tuning. The projector is then mounted and aligned using a 3D printed mount from PLA to ensure that a consistant placement is used. The projector mask is critical for the design of the optical masks as a shift in the location could alter whether or not the correct elements are active. Figure 55 displays how the projector is mounted to the system as well an internal view of the surface from the perspective of the projector.

The design of the optical mask is somewhat complicated by the throw ratio of the projector and the fact that the pattern must be projected onto a curved surface. The throw ratio of this specific projector is 1.2:1, meaning that for each mm of screen width, the projector must be 1.2mm away from the image. Because the projector is 230mm away from the surface, the maximum allowable image size of 191mm is sufficient to cover the 155mm opening of the sector antenna. The larger projector screen size means that the mask must be cropped appropriately to prevent unwanted reflections off the side walls.

(a)

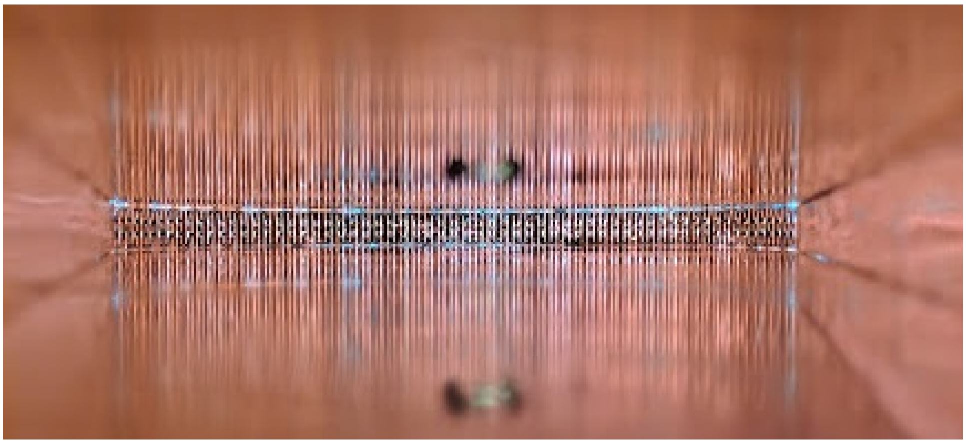

(b)

Figure 55. Projector on system: (a) mounted on antenna; (b) view of surface from projector (captured with Google Night Sight).

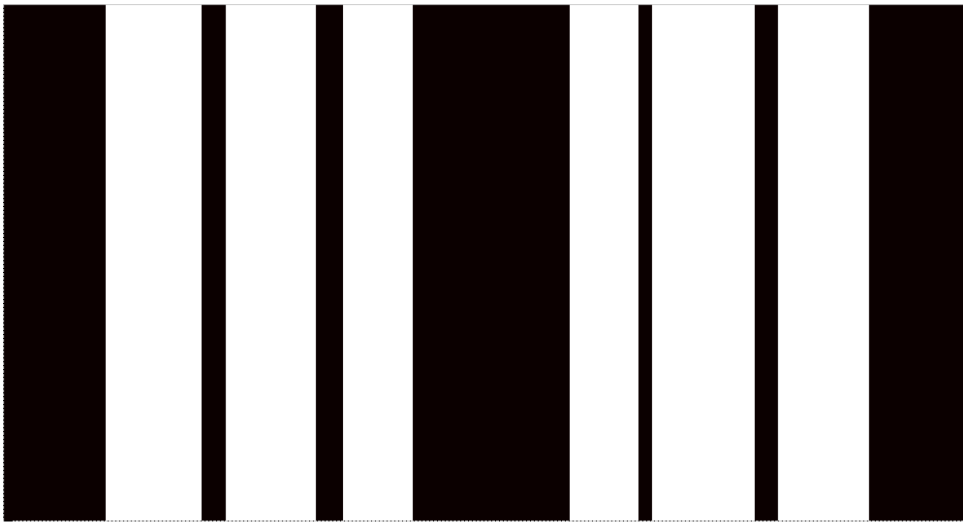

(a)

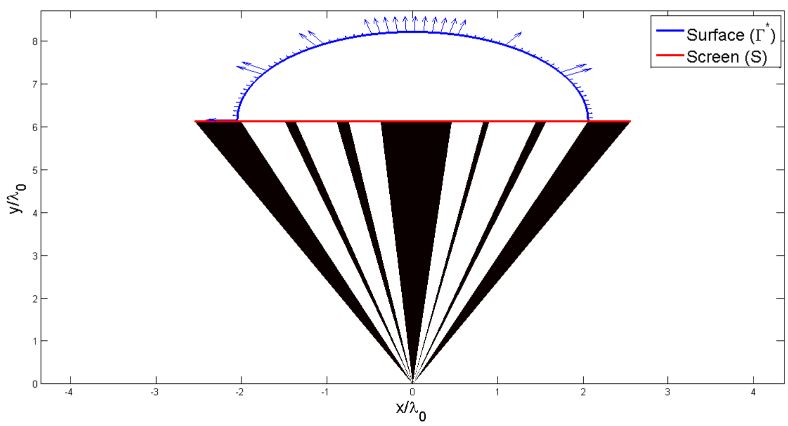

(b)

Figure 56. Mask to be projected: (a) image for projector screen; (b) top view of projection and resulting excitation pattern.

The mask design consists of identifying appropriate points on the surface Γ^* and projecting them onto a flat projector plane S defined by the plane

$$S(x) = y^*, \tag{4.2}$$

where $y^* = \min \Gamma^*$, $x \in \left(-\frac{y^*}{2T_r}, \frac{y^*}{2T_r}\right)$, and T_r is the projector throw ratio. The projection screen ensures that all of the points on Γ^* lay behind the surface of the screen. The width of the mask is determined to allow the projector to potentially illuminate any portion of S after accounting for the throw ratio. A point on Γ^* may then be projected onto the mathematical screen S using the transformation

$$\gamma = (x, y) \in \Gamma^* \to s(\gamma) = (x'(\gamma), y^*) \in S, \tag{4.3}$$

where

$$x' = \frac{y^*}{y} x. \tag{4.4}$$

Because the unit cells of the conformal surface are placed along the facets, it is important to identify the projection of facet onto the screen which is located along the interval (x_i', x_{i+1}') where

$$x_i' = \frac{y^*}{\Gamma(x_i)} x_i. \tag{4.5}$$

In order to turn a unit cell on or off, two subsequent facets must be illuminated or left dark. This mapping is critical for the image to avoid mistakenly activating incorrect unit cells. Figure 56

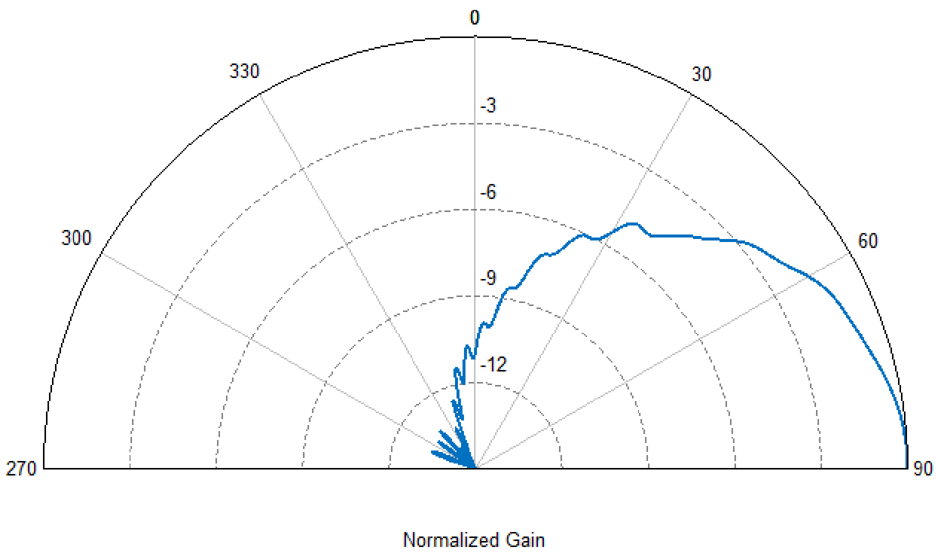

Figure 57. E-plane radiation pattern of individual gap.

demonstrates an example of a mask to be projected for a front steering beam and a top view of the projection.

4.5 Two-Dimensional Beam-Steering Potential

Because the vertical unit cell spacing is 10.18 mm, which is less than $\lambda_0/2$ at 8GHz, the antenna may be vertically arrayed in order to create a singly curved antenna system with both E- and H- plane steering. The E-plane steering is spatially possible because the electrically small unit cell has a relatively broad E-plane radiation pattern. This is exemplified by Figure 57,

Figure 58. Side view of system without projector.

which shows that E-plane radiation pattern of an individual gap simulated with FEKO. This pattern suggests that the system may be steered roughly $\pm 45°$ in the θ direction through a conventional phased array. This is in addition to the $\pm 60°$ of steerability with respect to ϕ.

In order to realize the E-plane steering without introducing grating lobes, the antenna must be less than $\lambda_0/2$ thick. At 8 GHz, a total thickness of less than 18.75 mm is possible because the unit cells are 10.18 mm. The acrylic sheets can be as small as 1mm each and the SMA connector is roughly 8.3 mm long, but SMA connectors may be placed slightly offset to each other to save space. A side view of these components is shown in Figure 58. While the current projector is not selected for a compact design, it could be redesigned to fit in a thin form factor, or lensed to illuminate multiple surfaces if desired. Because of the complexity required for the redesigned array method, the idea of vertically spacing the antenna elements is not tested in this work and will be left for potential future designs.

CHAPTER 5

EXPERIMENTAL VALIDATION

Due to the complexity of manufacturing and the potential errors that this may create, this experimentation is intended to be a proof of concept. The system manufactured in the previous chapter is examined through a number of experiments in order to determine the feasibility of both the optical tuning of the surface and the optimization of the design through the compact genetic algorithm (CGA). All experiments are carried out in the Andrew Electromagnetics Lab on the University of Illinois at Chicago (UIC) campus. Though the physically constructed antenna system is substantial to demonstrate the feasibility of the theoretical design, production ready systems would benefit from standardized manufacturing practices and specialized optical systems which would make the system more compact.

The experimental validation consists of several key phases. First, the change in the periodicity of the unit cell due to the finite height of the structure is examined as well as its effect on the ability to alter the amplitude of the radiated field. Next, this structure is illuminated with simple optical masks to demonstrate the ability of the masks to alter the pattern. Following this step, the masks will be designed using the CGA and the change in the pattern will be analyzed. Lastly, these patterns will also be examined over a range of frequencies in order to determine the system bandwidth.

5.1 Variation in Periodicity

The first step to test is to verify that the surface remains tunable with the change in the structure surrounding the surface. The surface placement in the waveguide experiment in section 4.3 behaves as a doubly periodic system due to the image of the surface across the reflecting walls of the waveguide. The new surface placement is simulated with Ansys HFSS to check that the surface maintains a tunable nature in the new configuration.

The simulation is constructed by using the same unit cell dimensions given in Table III, altering the boundary condition assignments surrounding the structure. The unit cell is located on the bottom of a 50mm tall box whith the faces above and below the unit cell being assigned as perfect electric conductor (PEC) plates to model the top and bottom of the antenna. The left and right walls of the box are then assigned as perfect megnetic conductor (PMC) plates to simulate the infinite periodicity along the x-axis of the model. The top of this box is then excited with a wave port excitation. The unit cell is centered in a larger surrounding box with the same width as the unit cell and with a height and length of 100mm. Once again the left and right faces are assigned as PMC plates to maintain the periodicity of the structure while the remaining faces of the box are assigned as radiating boundaries.

This simulation is run with a maximum delta of 0.02 with equally spaced frequencies from 8-12 GHz with a spacing of 500 MHz between frequencies. The solver is set to a maximum of fifteen passes with only one convergent pass required. This simulation converges for both the ON and OFF states of the PIN diode.

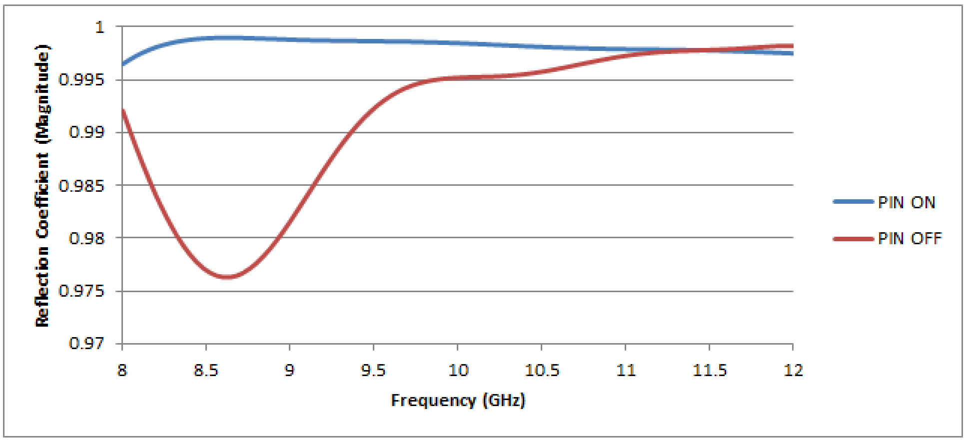

Figure 59. Reflection coefficient of surface in varying PIN diode states.

The magnitude of the reflection coefficient seen at the wave port is given on a linear scale in Figure 59 to show that the diode state alters the surface conditions with the new configuration. The reflection coefficient is used to calculate the total radiated power of the system from the conservation of power. This transmission coefficient is compared between the two states to determine the system tunability, which is shown in Figure 60. The tunability of the radiated power has a peak value of 13.55 dB at 8.65 GHz and maintains a tunability of greater than 10 dB from 8.25 to 9.25 GHz. The tunability magnitude in this range suggests that the surface is sufficient for beam steering in these frequency ranges.

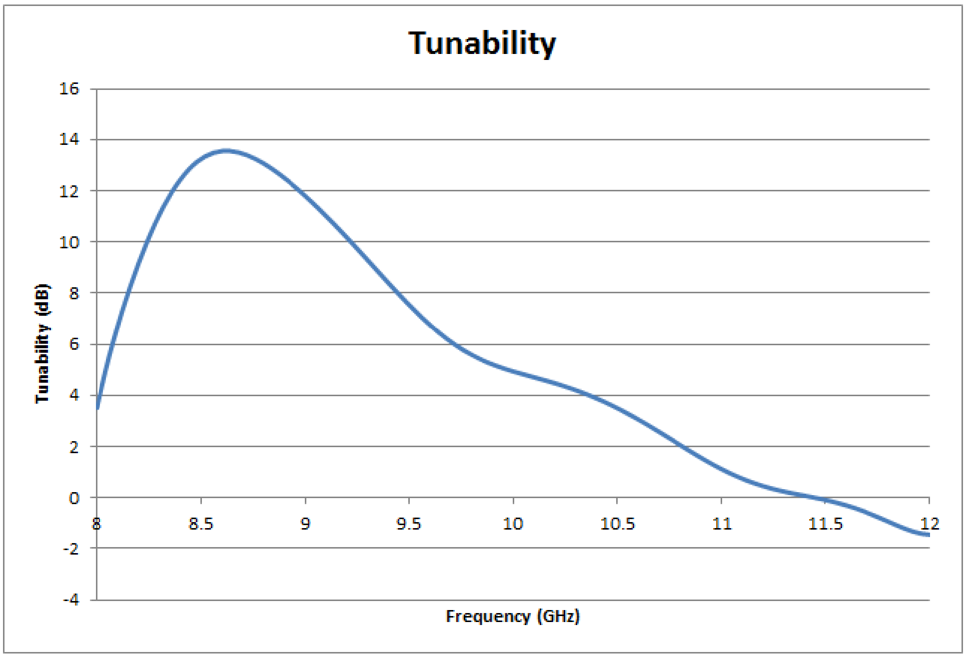

Figure 60. Tunability of total radiated power magnitude.

5.1.1 Magnitude Tunability

The simulated tunability is verified by testing the transmitted field between the experimental antenna and a standard horn antenna. To this end, the device under test (DUT) and the standard horn antenna are connected to the ports of a Keysight N5222A vector network analyzer (VNA) and the transmission is measured as the S_{21} parameter between the ports when the antennas are roughly 1 meter apart. The tunable surface of the DUT is powered through the USB port of a Lenovo Z40 laptop and the current and voltage are measured using a USB power monitor. The projector is connected to the laptop via an HDMI cable in order to control which mask is projected.

The surface is illuminated with a black screen in order to allow the field to be transmitted while a white screen is projected in order to block the transmission. The tunable surface draws a current of 40 mA from the USB port when illuminated with the white image and draws no current when illuminated with the black image. The transmission is measured from 8-12 GHz and the difference between the transmission coefficients in each state is reported as the tunability of the system. The measured tunability is compared to the simulated values in Figure 61. The simulated value is generally larger than the measured value and has a wider 10 dB bandwidth. Both the measured and simulated values have similar peak frequencies and magnitudes of around 14 dB at 8.6 GHz. This variation is likely due to both manufacturing errors as well as the curved nature of the surface which leads to uneven illumination.

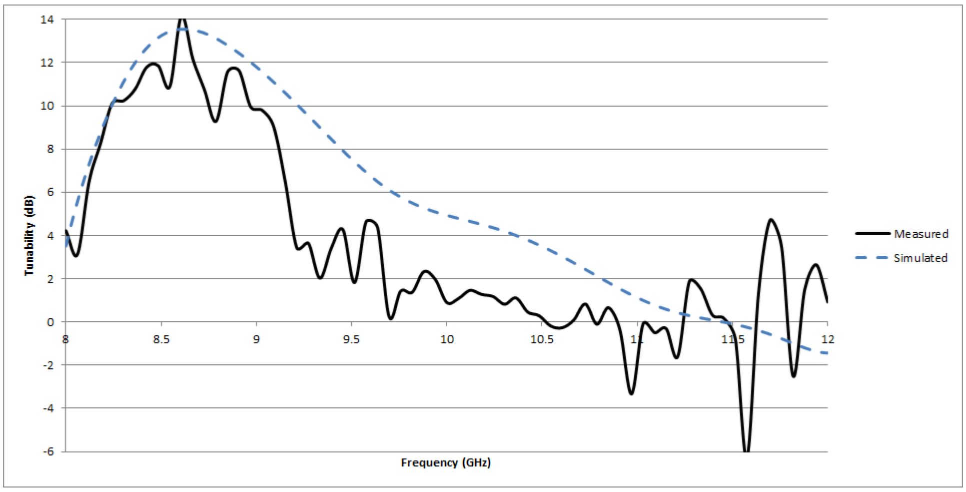

Figure 61. Measured and simulated tunability of transmitted power.

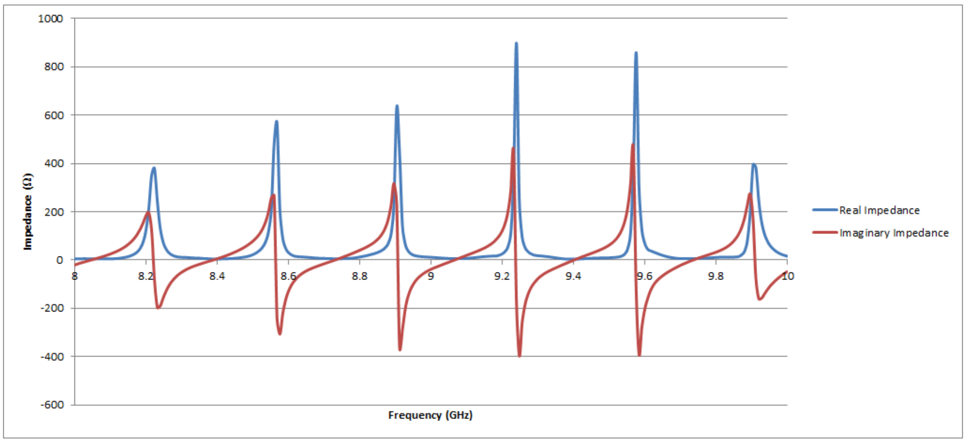

Figure 62. Input impedance at VNA port 1.

5.2 Input Impedance

The VNA is used to measure the input impedance of the antenna design which will be important for impedance matching. Port 1 of the VNA is connected to the DUT via a roughly 10” long SMA cable and the impedance is extracted from the S_{11} parameter of the VNA. The real and imaginary components of the input impedance seen at the input to the VNA is shown in Figure 62. The peaks in the real impedance are spaced roughly 336 MHz apart which is used to extract the parameter

$$k_l = 2\sqrt{\mu\epsilon}l = \frac{1}{f_s} = 2.97619 * 10^{-9}, \tag{5.1}$$

where l is the length of the transmission line. The parameter k_l is used to compute

$$\beta l = \pi k_l f, \tag{5.2}$$

where β is the propagation constant on the coaxial line. The product βl is important to determine the input impedance of the antenna from the equation

$$\frac{Z_{in}}{Z_0} = \frac{Z_L + jZ_0 \tan \beta l}{Z_0 + jZ_L \tan \beta l}, \tag{5.3}$$

where $Z_0 = 50\Omega$ is the impedance of the coaxial line and Z_L is the input impedance of the antenna [73]. This equation is manipulated to obtain

$$Z_L = Z_0 \frac{Z_{in} - jZ_0 \tan \beta l}{Z_0 - jZ_{in} \tan \beta l}. \tag{5.4}$$

The computed impedance of the antenna is shown in Figure 63, demonstrating the antenna is reactive (i.e. has a significant imaginary impedance), but has a notable real portion as well which is important for impedance matching. The input reactance also forms a downward trend with respect to frequency which suggests that the antenna is slightly capacitive. The combination of reactance with a small real impedance means that any impedance match is likely to be a narrow band match, but this is not a large concern because an active tuning circuit can be used to realize multiple narrow band matches at a variety of frequencies as

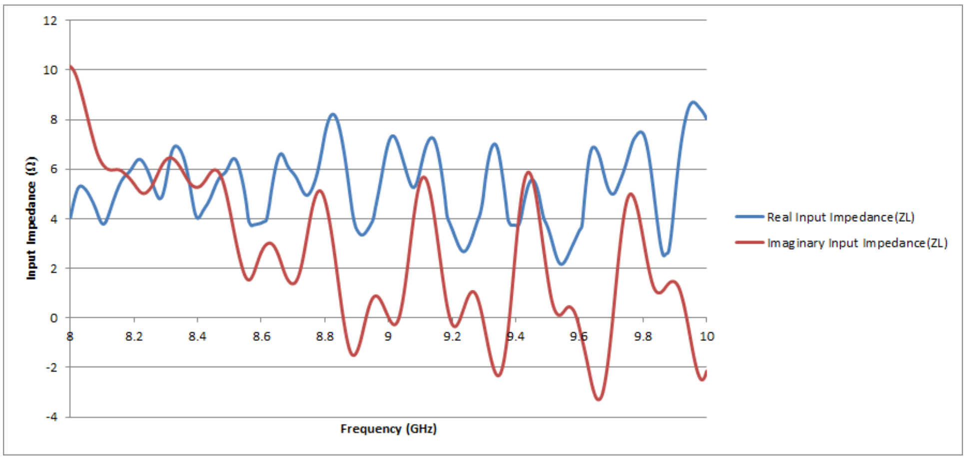

Figure 63. Antenna input impedance.

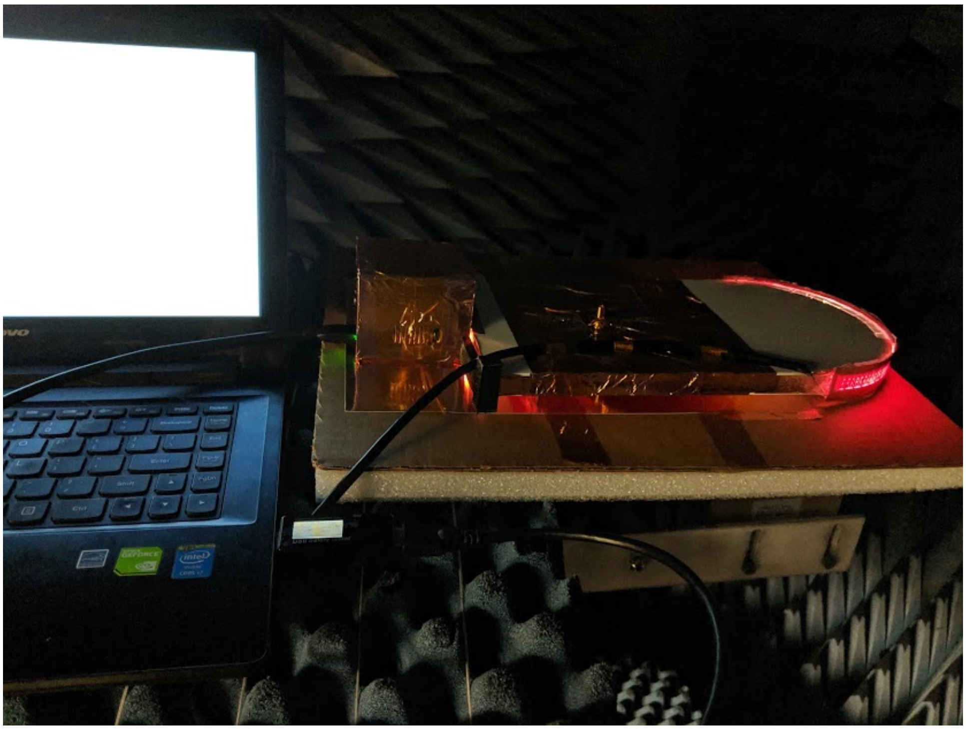

Figure 64. Antenna system in anechoic chamber.

needed. An active matching network is also important for this system because different masks can alter the radiated power and thus change the overall system impedance.

5.3 Pattern Measurements

The antenna radiation patterns are measured in the anechoic chamber at the Andrew Electromagnetics Lab at UIC. This chamber is controlled using the MI-3000 interface running on a

Windows computer, which controls a Keysight N5222A with Port 1 connected to the DUT and Port 2 connected to a standard gain antenna placed on the opposite side of the chamber. The reconfigurable antenna is accompanied in the chamber by a laptop computer which powers the tunable surface via a USB port and controls the projector. The setup of the antenna is shown in Figure 64 and the optical masks are loaded onto a PowerPoint presentation so the mask may be easily switched via a wireless mouse without disturbing the system.

The antenna is mounted on a turntable, which is controlled via the MI-3000 program. To measure the radiation pattern of the antenna, the turntable is rotated from 190° to 350° where 270° is aligned to the the broadside of the antenna. The measurement is constrained to this range of angles in order to avoid errors due to over rotating the system. Furthermore, the back-lobes are not a focus of the experiment and would be significantly reduced if the antenna were placed on a large structure. The MI-3000 program samples the S_{21} parameter of the VNA every 1° in order to obtain the radiation pattern of the antenna. This pattern is then exported to an Excel spreadsheet in order to normalize the patterns and plot the results.

5.3.1 On/Off Pattern Variation

The first pattern variation to test in the antenna chamber is the simple switching between the black and white screens as the optical mask. The test reveals whether the magnitude of the tuning is even throughout the pattern. Uneven tuning between the black and white screens may be due to a number of factors. The most likely reasons are either an inability to tune the surface due to elements not being sufficiently illuminated or construction errors such as a

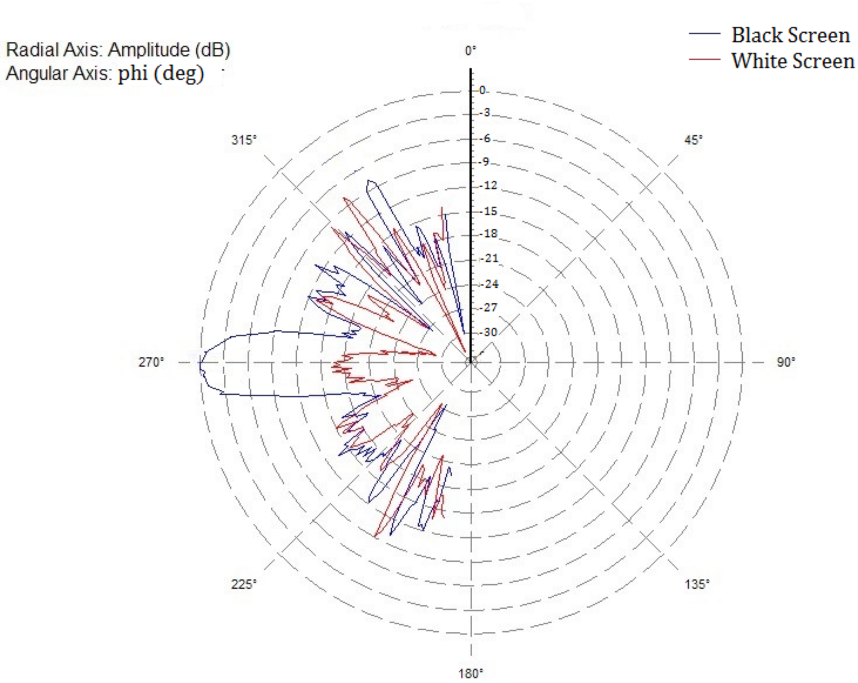

Figure 65. Variation in radiation pattern due to black and white screen masks.

gap in the surface. Either reason may lead to errors between the theoretical design and the experimental results.

For the black and white screen test, the radiation patterns are each measured at 8.6 GHz from 190 ° to 350° in 1° increments. The results are shown in Figure 65 and normalized to the peak of the radiation pattern associated with the black mask. Figure 65 confirms that the

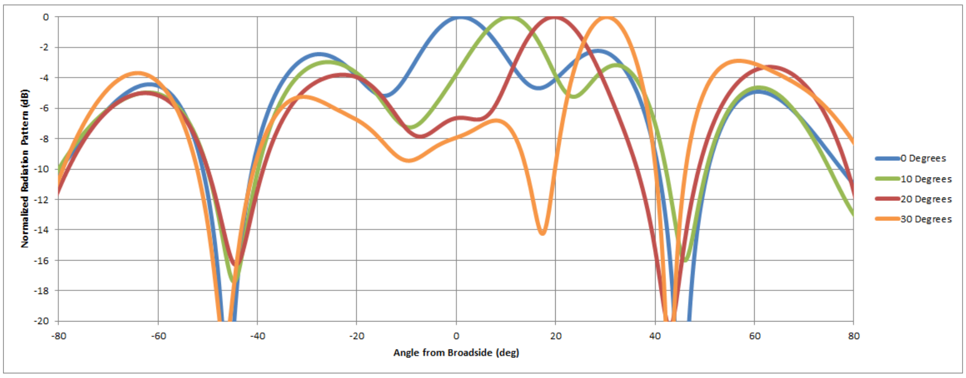

Figure 66. Theoretical radiation patterns designed by the CGA.

magnitude of the transmitted field is not tunable away from the broadside of the pattern, but is tunable towards the broadside angle. The shape of the beam is roughly the same for both the black and white mask. The magnitude of the transmitted field is altered by roughly 16 dB at the peak of the radiation pattern which is in line with the measured tunability of roughly 14 dB shown in Figure 61.

5.3.2 CGA Steering

Masks for the antenna system are designed to steer the main beam at 8.25 GHz from 0° to 30° in 10° increments. These masks are designed utilizing the CGA with a leakage factor of

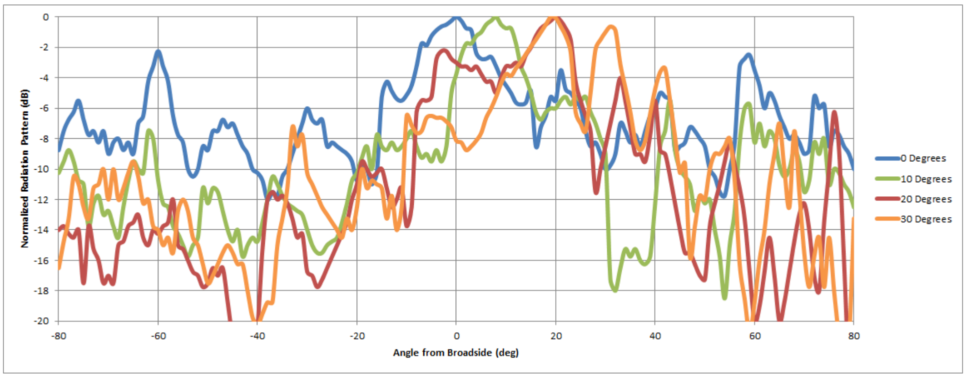

Figure 67. Measured radiation patterns of physical system with masks designed by the CGA.

12dB, a conversion rate multiplier of .5, and an extinction bound of 0.05. The CGA is continued to 500 generations with a population size of 2^9.

The expected patterns due to the CGA are shown in Figure 66 and demonstrate that all four of the patterns are expected to hit the desired target angle. The masks associated with each of the designed radiation patterns are projected onto the OT-MS in order to steer the beam in the physical system. The measured patterns in the anechoic chamber are shown in Figure 67. The experimental results show that the system is able to steer the main beam near all the target angles with the notable exception of the 30° beam which is smaller than a large side lobe at 20°.

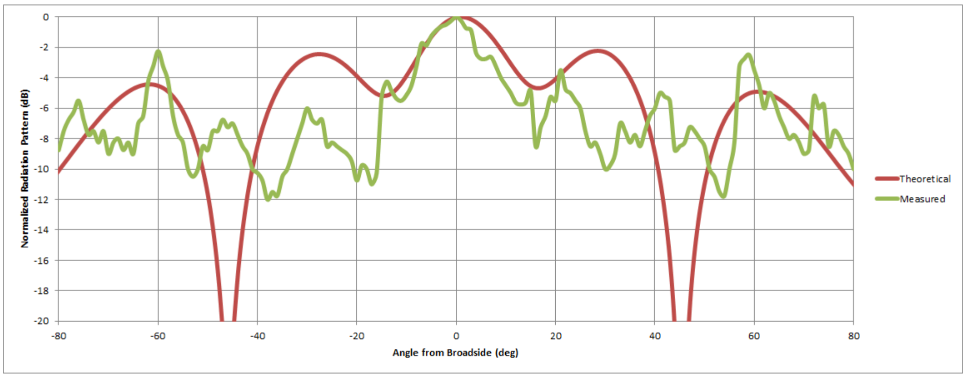

Figure 68. Experimental and measured radiation pattern associated with the broadside pattern.

The first three measured patterns roughly correlate with the theoretical pattern from the CGA in terms of the main beamwidth, but the side lobes differ significantly. This is demonstrated in Figure 68 which compares the theoretical and measured radiation patterns for the mask to steer the main beam to the broadside of the antenna. The theoretical design has a half-power beam-width of roughly 18°, which is very similar to the measured half power beam-width of 16°. There is no notable correlation however between the theoretical and measured side-lobes.

The difference in correlation is also present in the theoretical and measured radiation patterns for the beam steered to 10° and 20° from the broadside. This comparison is demonstrated

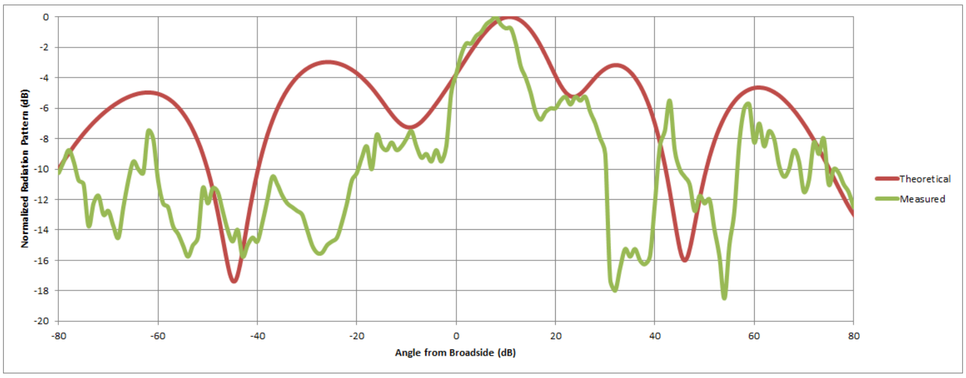

(a)

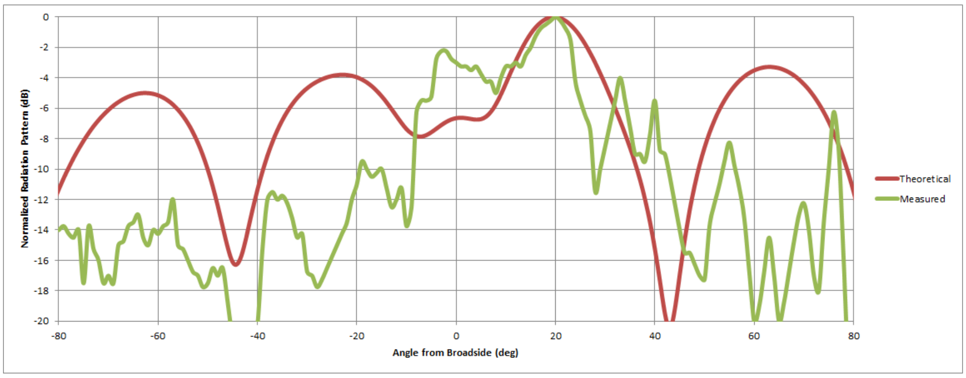

(b)

Figure 69. Experimental and measured radiation pattern associated with (a) 10° from broadside pattern (b) 20° from broadside pattern.

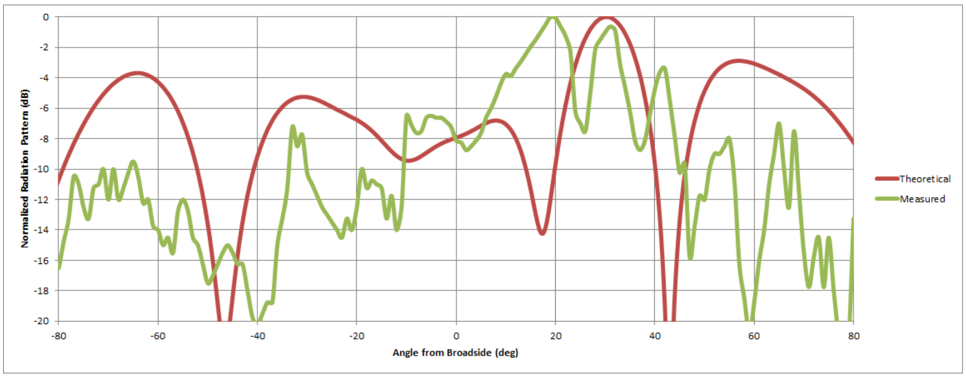

Figure 70. Experimental and measured radiation pattern associated with the 30° from broadside pattern.

in Figure 69 for the 10° and 20° target angle. The main beam at 10° has a measured half-power beam-width of 13°, while the theoretical beam-width is 16°. The peak of the main beam in the radiation pattern is at roughly 8° which slightly misses the target at 10°. Similarly, the measured half power beam-width for the target at 20° is 12° while the theoretical value is 15°, and this beam does hit the target angle.

The correlation in the main beam fails as the beam is steered to 30° from the broadside angle. At this angle, the beam at 30° is eclipsed by the larger beam at 20°. The larger beam is not predicted in the theoretical pattern and the difference between the two is shown in Figure 70. This difference could occur for a number of reasons, but one of the likeliest causes is that the

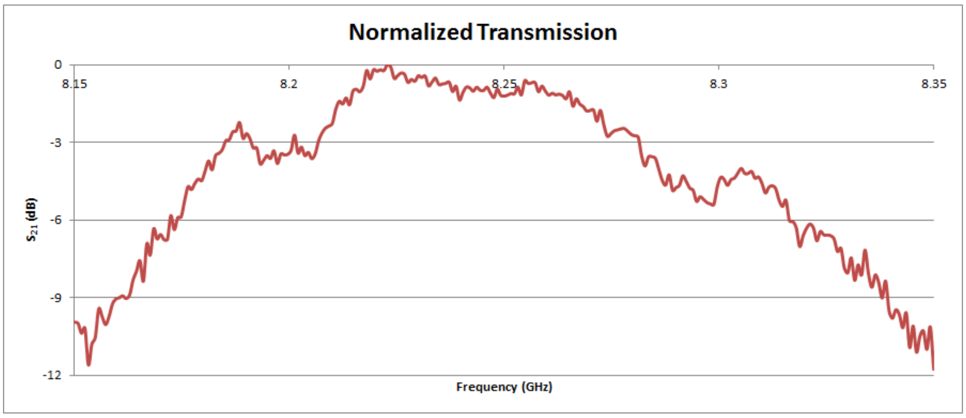

Figure 71. Measured transmission associated with broadside mask.

edges of the OT-MS are less tunable than expected. The tunability issues can be mitigated by using a more powerful projector or using additional photodiodes in parallel to increase the bias current.

5.4 Frequency Dependence

One important parameter of beam-steering designs is the operating bandwidth of the transmitted signal. In order to measure the bandwidth, the designed antenna is place in the anechoic chamber and the system is rotated such that the receiving antenna in the chamber is located at the peak of the radiation pattern associated with the given mask. Then, the VNA is set to measure the S_{21} parameter from 8.15-8.35 GHz.

The measured transmission coefficient associated with the broadside mask is normalized to the peak measured value as shown in Figure 71. The transmission coefficient varies by less than 3dB from 8.21-8.28 GHz which is a percentage bandwidth of only .835 percent, representing a very narrow band system. All of the masks have comparable bandwidths to the broadside mask. One benefit of high frequency systems is that narrow fractional bandwidths are sufficient for modern communications. For example, a 100 MHz bandwidth that is required in 5G systems is only a fractional bandwidth .833 percent at 12 GHz. Even though bandwidth is not a design criteria of the CGA, the designed masks are still viable in narrow band applications such as 5G base stations or imaging systems. Broadband applications, however, require more complex designs and a modified cost function for the CGA to account for bandwidth.

CHAPTER 6

CONCLUSION

The present work develops and demonstrates a novel method to create a conformal antenna with a reconfigurable radiation pattern. The main body and feed structure of the antenna is designed such that it can be placed behind a curved surface which is ideal for structures such as airlines or cars where drag is a concern. The conformal nature of the antenna is also useful for applications which require the antenna to be hidden from view, such as cell towers or internet of things devices.

A major benefit of the reconfigurable nature of the antenna is that it can be altered to operate in different frequency bands by designing a surface with broadband tunability. This frequency agility demonstrates that although an individual beam steering pattern can have a narrow bandwidth, the pattern can be altered as different communication channels and patterns are required. This broad range of usable frequencies are especially useful for 5G communications and vehicle to vehicle systems which operate in dynamic environments and in close proximity to other communications antennas. Issues created by these crowded environments such as poor signal strength and interference can be mitigated by altering the antenna pattern and operating frequency.

The antenna design explored in this work is laid out in four chapters. The first chapter is a review of the literature required to develop and model the system that is carried out in 2. The beginning of the literature review focuses on antenna array systems which form the basis of modern pattern synthesis and beam steering techniques. The literature review also examines metasurfaces and metamaterials, which are popular in numerous systems because they make unique material properties possible, not found in nature. Tunable matasurfaces are given particular attention as they are the primary mechanism for steering the beam in the designed antenna system. Lastly, the literature review details heuristic design methods and their applications to electromagnetic problems such as this.

The second body chapter details the methods for modeling and designing the antenna which is done in 3. The chapter analyzes a simplified radiating gap as the basis of the transmitarray surface and then places gaps to cover the length of a singley curved surface. In this chapter, a compact genetic algorithm (CGA) is developed to select which gaps should be allowed to radiate to steer the main bean of the TA radiation pattern to a desired angle. The patterns developed through the CGA are correlated with MoM simulations using FEKO to demonstrate the viability of the designed patterns. Furthermore the chapter discusses the importance of the cost function used to guide the CGA and its versatility for additional surfaces and design criteria.

The third body chapter focuses on the physical construction of the system, which is necessary to translate the CGA results to a usable system. The fundamental building block of the reconfigurable antenna array is the optically tunable metasurface , is then detailed in the first part of this chapter. The surface is designed using Ansys HFSS and then is validated through experiments in a WR-90 waveguide coupler. The simulation data is used to show non-ideal behavior in the surface such as a finite tunability and mutual coupling between the unit cells.

The tunability can be improved through high end PIN diodes, but the Skyworks SMP1320-079LF is selected due to its low cost and manageable package size. Following the surface design, the chapter details the construction steps of the larger structure such as the edges of the horn antenna and the method of integrating a projector to tune the surface.

The last major stage validates the theory and construction through measurements of the optically reconfigurable antenna carried out in 4. The first part of this chapter demonstrates that the surface can be modulated with a light source and that the modulation alters the radiated field from the antenna. The antenna is shown to steer the main beam using masks designed through the CGA, even though the theoretical and measured patterns vary significantly. The radiation patterns are also shown to have a roughly 80 MHz bandwidth which is sufficient for modern cellular communications channels, but is less than the 100 MHz bandwidth which is required for 5G systems.

Improvements such as increasing the bandwidth and magnitude of the optically tunable metasurface are still necessary before an optically tunable system is ready for production, but the methods behind the system show promise in beam steering applications. Beam steering is becoming increasingly important in modern communication systems such as 5G antennas where beam steering is important for improving the performance of cellular communication networks. Modern networks such as 5G systems will require a large number of antennas to be placed in a number of locations. Antennas on vehicles or in urban settings can benefit from the conformal nature of the antenna to reduce drag and conceal the antenna from view. The reconfigurable and conformal nature of this antenna have important benefits which can be useful in a broad range of applications.

CITED LITERATURE

1. Building the future of mobility. `https://peoriamagazines.com/ibi/2018/mar/building-future-mobility`. Accessed: 2019-2-2.

2. Baek, S. M., Ko, M. G., Kim, M. S., and Joo, Y. S.: Structural design of conformal load-bearing array antenna structure (claas). Advanced Composite Materials, 26(S1):29–42, March 2017.

3. Sievenpiper, D. F.: High-Impedance Electromagnetic Surfaces. Los Angeles, University of California Los Angeles, 1999. PhD Dissertation.

4. Josefsson, L. and Persson, P.: Conformal Array Antenna Theory and Design. Hoboken, New Jersey, Wiley-Interscience, 2006.

5. Chireix, H.: Antennes á rayonnement zénithal réduit. L'Onde Electrique, 15:440–456, 1936.

6. Knudsen, H.: Bidrag till teorien for Antennsystemer med hel eller delvis Rotationssymmetri. Copenhagen, Teknisk Forlag, 1953. PhD Dissertation.

7. Gething, P.: High-frequency direction finding. Proceedings of IEE, 113(1):49–61, January 1966.

8. Wait, J. R.: Electromagnetic Radiation from Cylindrical Structures. London, England, Pergamon Press, 1959.

9. Shapira, J., Felsen, L., and Hessel, A.: Ray analysis of conformal antenna arrays. IEEE Transactions on Antennas and Propagation, 22(1):46–63, January 1974.

10. Thiele, G. and Donn, C.: Design of a small conformal array. IEEE Transactions on Antennas and Propagation, 22(1):64–70, January 1974.

11. Gregorwich, W.: An electronically despun array flush-mounted on a cylindrical spacecraft. IEEE Transactions on Antennas and Propagation, 22(1):71–74, January 1974.

12. Munson, R.: Conformal microstrip antennas and microstrip phased arrays. IEEE Transactions on Antennas and Propagation, 22(1):74–78, January 1974.

13. Hsiao, J. and Cha, A.: Patterns and polarizations of simultaneously excited planar arrays on a conformal surface. IEEE Transactions on Antennas and Propagation, 22(1):81–84, January 1974.

14. Gobert, J. and Yang, R.: A theory of antenna array conformal to surfaces of revolution. IEEE Transactions on Antennas and Propagation, 22(1):87–91, January 1974.

15. Proceedings of first european workshop on conformal antennas. Karlsruhe, Germany. 29 October 1999.

16. Proceedings of second european workshop on conformal antennas. The Hague, The Netherlands. 24-25 April 2001.

17. Proceedings of third european workshop on conformal antennas. Bonn, Germany. 22-23 October 2003.

18. Proceedings of fourth european workshop on conformal antennas. Stockholm, Sweden. 23-24 May 2005.

19. Karthikeya, G., Agnihotri, N., S.S. Siddiq, K. M., and Thyagaraj, T.: A conformal uhf antenna for cargo helicopter belly. 2016 IEEE 5th Asia-Pacific Conference on Antennas and Propagation (APCAP), Kaohsiung, Taiwan, 3(2):285–286, July 2016.

20. Pelton, E. L. and Munk, B. A.: A streamlined metallic radome. IEEE Transactions on Antennas and Propagation, 22(6):799–803, November 1974.

21. Munger, A. D., Vaughn, G., Provencher, J. H., and Gladman, B. R.: Conical array studies. IEEE Transactions on Antennas and Propagation, 22(1):35–43, January 1974.

22. Christodoulou, C. G., Tawk, Y., Lane, S. A., and Erwin, S. R.: Reconfigurable antennas for wireless and space applications. Proceedings of the IEEE, 100(7):2250–2261, July 2012.

23. Costantine, J., Tawk, Y., Barbin, S. E., and Christodoulou, C. G.: Reconfigurable antennas: Design and applications. Proceedings of the IEEE, 103(3):424–437, July 2015.

24. Chu, L.: Physical limitations of omnidirectional antennas. Journal of Applied Physics, 19:1163–1175, 1948.

25. Zhang, Z.: Antenna Design for Mobile Devices. Singapore, John Wiley & Sons (Asia), 2011.

26. Chi, T., Park, J. S., Li, S., and Wang, H.: A millimeter-wave polarization-division-duplex transceiver front-end with an on-chip multifeed self-interference-canceling antenna and an all-passive reconfigurable canceller. IEEE Journal of Solid-state Circuits, 53(12):3628–3639, December 2018.

27. Venkatakrishnan, S. B., Alwan, E. E., and Volakis, J. L.: Wideband rf self-interference cancellation circuit for phased array simultaneous transmit and receive systems. IEEE Access, 6:3425–3432, January 2018.

28. Stutzman, W. L. and Thiele, G. A.: Antenna Theory and Design. Hobokken, New Jersey, John Wiley & Sons, Inc., 2013. 3rd. ed.

29. Balanis, C. A.: Advanced Engineering Electromagnetics. Hoboken, New Jersey, John Wiley & Sons, 2012. 2nd ed.

30. Project soli. `https://atap.google.com/soli/`. Accessed: 2019-2-2.

31. Sleasman, T., Boyarsky, M., Pulido-Mancera, L., Fromenteze, T., Imani, M. F., Reynolds, M. S., and Smith, D. R.: Experimental synthetic aperture radar with dynamic metasurfaces. IEEE Transactions on Antennas and Propagation, 65(12):6864–6877, Dec 2017.

32. Sleasman, T., Member, S., Boyarsky, M., Pulido-Mancera, L., Fromenteze, T., Mohammadreza, Imani, F., Reynolds, M. S., and Smith, D. R.: Experimental synthetic aperture radar with dynamic metasurfaces. IEEE Transactions on Antennas and Propagation, 65(12):6864–6877, December 2017.

33. Lo, Y.: A mathematical theory of antenna arrays with randomly spaced elements. IEEE Transactions on Antennas and Propagation, 12(3):257–268, May 1964.

34. Khalid, A., Shah, I. H., Mirza, H. A., and Sheikh, S. A.: Pattern synthesis of conformal antenna array to achieve optimized amplitude weights for null steering and psll reduction. Proceedings of 2017 14th International Bhurban Conference on Applied Sciences & Technology (IBCAST), Islamabad, Pakistan, pages 816–819, January 2017.

35. Hansen, R.: Conformal Antenna Array Design Handbook. 1982.

36. Hou, Y., Fu, J., and Zhang, Y.: A modified particle filter for mutual coupling correction of a conformal antenna array. 2016 IEEE International Conference on Electronic Information and Communication Technology (ICEICT 2016), Harbin , China, pages 536–539, August 2016.

37. Rhodes, D. R.: The optimum line source for the best mean-square approximation to a given radiation pattern. IEEE Transactions on Antennas and Propagation, 11(4):440–446, July 1963.

38. Chang, H.-P., Sarkar, T. K., and Pereira-Filho, O. M. C.: Antenna pattern synthesis utilizing spherical bessel functions. IEEE Transactions on Antennas and Propagation, 48(6):853–859, June 2000.

39. Bucci, O., Capozzoli, A., D'Elia, G., and Musto, S.: A new approach to the power pattern synthesis of reflectarrays. Proceedings of the 2004 URSI Electromagnetics Theory Symposium (URSI EMTS),, pages 1053–1055, May 2004.

40. Niccolai, A., Grimaccia, F., Mussetta, M., Pirinoli, P., Bui, V. H., and Zich, R. E.: Social network optimization for microwave circuits design. Progress In Electromagnetics Research, 58:51–60, June 2015.

41. Hansen, W. and Woodyard, J.: A new principle in directional antenna design. Proceedings of the Institute of Radio Engineers, 26(3):333–345, March 1938.

42. Lee, S., Song, S., Kim, Y., Lee, J., Cheon, C.-Y., Seo, K.-S., and Kwon, Y.: A v-band beam-steering antenna on a thin-film substrate with a flip-chip interconnection. IEEE Microwave and Wireless Components Letters, 18(4):287–289, April 2008.

43. Darvazehban, A., Manoochehri, O., Salari, M. A., Parisa Dehkhoda, M., and Tavakoli, A.: Ultra-wideband scanning antenna array with rotman lens. IEEE Transactions on Microwave Theory and Techniques, 65(9):3435–3442, 2017.

44. Abbaspour-Tamijani, A. and Sarabandi, K.: An affordable millimeter-wave beam-steerable antenna using interleaved planar subarrays. IEEE Transactions on Antennas and Propagation, 51(9):2193–2202, 2003.

45. Ouedraogo, R. O., Rothwell, E. J., and Greetis, B. J.: A reconfigurable microstrip leaky-wave antenna with a broadly steerable beam. IEEE Transactions on Antennas and Propagation, 59(3):3080–3083, August 2011.

46. Sievenpiper, D., Schaffner, J., Loo, R., Tangonan, G., Ontiveros, S., and Harold, R.: Device independent file format. IEEE Transactions on Antennas and Propagation, 50(3):384–390, March 2002.

47. Chen, X., Ge, Y., and Chen, L.: A folded reflectarray antenna at ka band. 2018 International Workshop on Antenna Technology (iWAT), Nanjing, China, March 2018.

48. Minatti, G., Faenzi, M., Martini, E., Caminita, F., Vita, P. D., Gonzlez-Ovejero, D., Sabbadini, M., and Maci, S.: Modulated metasurface antennas for space: Synthesis, analysis and realizations. IEEE Transactions on Antennas and Propagation, 63(4):1288–1300, April 2015.

49. Sazegar, M., Zheng, Y., Kohler, C., Maune, H., Nikfalazar, M., Binder, J. R., and Jakoby, R.: Beam steering transmitarray using tunable frequency selective surface with integrated ferroelectric varactors. IEEE Transactions on Antennas and Propagation, 60(12):5690–5699, December 2012.

50. Landy, N. I., Sajuyigbe, S., Mock, J. J., Smith, D. R., and Padilla, W. J.: A perfect metamaterial absorber. Physical Review Letters, 100(20):207402–207405, May 2008.

51. Valentine, J., Zhang, S., Zentgraf, T., Ulin-Avila, E., Genov, D. A., Bartal, G., and Zhang, X.: Three-dimensional optical metamaterial with a negative refractive index. Nature Letters, 455(18):376–380, September 2008.

52. Smith, D. R., Padilla, W. J., Vier, D. C., Nemat-Nasser, S. C., and Schultz, S.: Composite medium with simultaneously negative permeability and permittivity. Physical Review Letters, 84:4184–4187, May 2000.

53. Holloway, C. L., Kuester, E. F., Gordon, J. A., O'Hara, J., Booth, J., and Smith, D. R.: An overview of the theory and applications of metasurfaces: The two-dimensional equivalents of metamaterials. IEEE Antennas and Propagation Magazine, 54(2):10–35, April 2012.

54. Chen, C.-C.: Transmission of microwave through perforated flat plates of finite thickness. IEEE Transactions on Microwave Theory and Techniques, 21(1):1–6, Jan 1973.

55. Costa, F., Monorchio, A., and Manara, G.: An overview of equivalent circuit modeling techniques of frequency selective surfaces and metasurfaces. Applied Computational Electromagnetics Society Journal, 29:960–974, 12 2014.

56. Luo, Z., Zhao, L., Xue, C., and Sievenpiper, D.: An electrically tunable absorbing metasurface for surface waves and plane waves. In 2016 Asia-Pacific Microwave Conference (APMC), pages 1–4, Dec 2016.

57. Evaluation of a novel topology for mems programmable reflectarray antennas. IEEE Transactions on Microwave Theory and Techniques, 57(12):3333–3344, Dec 2009.

58. Fan, K., Strikwerda, A. C., Tao, H., Zhang, X., and Averitt, R. D.: A tunable 3d terahertz metamaterial. In 2011 International Conference on Infrared, Millimeter, and Terahertz Waves, pages 1–2, Oct 2011.

59. Kim, S., Li, A., and Sievenpiper, D. F.: Reconfigurable impedance ground plane for broadband antenna systems. In 2017 IEEE International Symposium on Antennas and Propagation USNC/URSI National Radio Science Meeting, pages 1503–1504, July 2017.

60. Palma, L. D.: Antennes Réseaux Transmetteurs Reconfigurables aux Fréquences Millimétriques. Rennes, Université De Rennes, 2015. PhD Dissertation.

61. Tao, H., Strikwerda, A. C., Fan, K., Padilla, W. J., Zhang, X., and Averitt, R. D.: Reconfigurable terahertz metamaterials. Phys. Rev. Lett., 103:147401–147404, Oct 2009.

62. Fan, K., Zhao, X., Zhang, J., Geng, K., Keiser, G. R., Seren, H. R., Metcalfe, G. D., Wraback, M., Zhang, X., and Averitt, R. D.: Optically tunable terahertz metamaterials on highly flexible substrates. IEEE Transactions on Terahertz Science and Technology, 3(6):702–708, Nov 2013.

63. Shen, N.-H., Massaouti, M., Gokkavas, M., Manceau, J.-M., Ozbay, E., Kafesaki, M., Koschny, T., Tzortzakis, S., and Soukoulis, C. M.: Optically implemented broadband blueshift switch in the terahertz regime. Phys. Rev. Lett., 106:037403–037406, Jan 2011.

64. Hoeh, M. A., Neu, J., Schmitt, K. M., and Rahm, M.: Silicon-based, ultra-thin, flexible optically tunable metamaterial-bandpass filter in the thz-regime. In 2014 39th International Conference on Infrared, Millimeter, and Terahertz waves (IRMMW-THz), pages 1–2, Sep. 2014.

65. Poort, M. D. and Uslenghi, P. L.: Scattering by a sheet impedance strip in a metal plane. In 2018 IEEE International Symposium on Antennas and Propagation and USNC-URSI Radio Science Meeting, Jul. 2018.

66. Stratton, J. A., Morse, P. M., Chu, L. J., Little, J. D. C., and Corbato, F. J.: Spheroidal Wave Functions: Including Tables of Separation Constants and Coefficients. Published jointly by the Technology Press of M.I.T. and Wiley, 1956.

67. General mathieu functions with arbitrary parameters v1.0. https://www.mathworks.com/matlabcentral/fileexchange/27101-general-mathieu-functions-with-arbitrary-parameters-v1-0. Accessed: 2018-06-10.

68. Uslenghi, P. L. E.: Exact penetration, radiation, and scattering for a slotted semielliptical channel filled with isorefractive material. IEEE Transactions on Antennas and Propagation, 52(6):1473–1480, June 2004.

69. Matlab. https://www.mathworks.com/products/matlab.html. Accessed: 2019-01-15.

70. Poort, M. D. and Uslenghi, P. L.: Conformal gap array design utilizing a compact genetic algorithm. In 2018 IEEE International Symposium on Antennas and Propagation and USNC-URSI Radio Science Meeting, Jul. 2018.

71. Poort, M. D. and Uslenghi, P. L.: A novel x-band optically tunable transmission surface based on lumped element optoelectonic components. In 2019 USNC-URSI National Radio Sciene Meeting, Jul. 2018.

72. Ansys hfss 3d electromagnetic field simulator for rf and wireless design. https://www.ansys.com/products/electronics/ansys-hfss. Accessed: 2019-02-10.

73. Pozar, D.: Microwave Engineering, 4th Edition. Wiley, 2011.

VITA

Marco David Poort

Education

University of Illinois at Chicago *August 2015 - August 2019*
Doctorate of Philosophy, Electrical and Computer Engineering
Department of Electrical and Computer Engineering

University of Illinois at Chicago *August 2015 - December 2017*
Masters of Science, Electrical and Computer Engineering
Department of Electrical and Computer Engineering

California State University Chico *August 2010 - May 2015*
Bachelors of Science, Electrical and Electronic Engineering
Department of Electrical and Computer Engineering

California State University Chico *August 2010 - May 2015*
Bachelors of Science, Appplied Mathematics
Department of Mathematics and Statistics

Awards

Provost Research Award
Funding to advance graduate reasearch at the University of Illinois at Chicago

National Academies Travel Fellowship
Travel assistance for students to attend URSI conferences

Experience

RF Desense Engineer *January 2019 - Present*
Google, Inc.

Teaching Assistant *August 2016 - December 2018*
University of Illinois at Chicago

Hardware Intern *January 2018 - Augustt 2018*
Google, Inc.

Research Assistant *August 2015 - May 2016*
University of Illinois at Chicago

Intern *August 2015 - May 2016*
Solutions Cubed

Publications and Presentations

M.D. Poort , V.G. Daniele, and P.L.E. Uslenghi, "Electromagnetic scattering by an infinite array of truncated metal plates", *Radio Sci.*, vol. 52, no. 4, pp. 490-497, Apr. 2017.

M.D. Poort, V.G. Daniele, and P.L.E. Uslenghi, "Electromagnetic scattering by a pair of semi-infinite metal plates perpendicularly truncated by a metal ground plane", *IEEE Trans. Antennas Propag.*, vol. 66, no. 5, pp. 2515-2521, Mar. 2018.

M.D. Poort and P.L.E. Uslenghi, "A Novel X-Band Optically Tunable Transmission Surface Based on Lumped Element Optoelectonic Components", in *National Radio Science Meeting*, Boulder, CO, United States, January 2019

M.D. Poort, V.G. Daniele, and P.L.E. Uslenghi, "Electromagnetic Scattering by Three Unevenly Spaced Parallel Half-planes Truncated by a Metal Plane", in *Intl. Conf. Electromagnetics Adv. Appl. (ICEAA 2018)*, Cartagena, Columbia, September 2018

S. Singh, M.D. Poort, and P.L.E. Uslenghi, "Scattering by a Quarter Sphere Located Inside a Dihedral Reflector", IEEE APS Symp. on Anttennas and Propag., Boston, MA, United States, July 2018

M.D. Poort and P.L.E. Uslenghi, "Design of Singly Curved Conformal Transmitarrays Using a Compact Genetic Algorithm", in *IEEE APS Symp. on Anttennas and Propag.*, Boston, MA, United States, July 2018

M.D. Poort and P.L.E. Uslenghi, "Scattering by a Sheet Impedance Strip in a Metal Plane", in *IEEE APS Symp. on Anttennas and Propag.*, Boston, MA, United States, July 2018

M.D. Poort, "Full Wave Analysis of Two-Dimensional Periodic Array of Dielectric-Filled Rectangular Windows", in *National Radio Science Meeting*, Boulder, CO, United States, January 2018

S. Singh, M.D. Poort, and P.L.E. Uslenghi, "Scattering by a Hemisphere on a Metallic Plate", in *National Radio Science Meeting*, Boulder, CO, United States, January 2018

A. Arora, M.D. Poort, and P.L.E. Uslenghi, "Scattering by Cylindrical Posts of Various Cross Sections Located Inside a Parallel-Plate Waveguide", in *National Radio Science Meeting*, Boulder, CO, United States, January 2018

M.D. Poort, and P.L.E. Uslenghi, "Scattering by a Coated Elliptic Cylinder Truncated by a Metal Plane", in *Intl. Conf. Electromagnetics Adv. Appl. (ICEAA 2017)*, Verona Italy, September 2017

M.D. Poort, V.G. Daniele, and P.L.E. Uslenghi, "Scattering by three parallel half-planes perpendicularly truncated by a metal plane", in *Intl. Conf. Electromagnetics Adv. Appl. (ICEAA 2017)*, Verona Italy, September 2017

M.D. Poort and P.L.E. Uslenghi, "radiation pattern synthesis for a prolate spheroidal antenna", in *IEEE APS Symp. on Anttennas and Propag.*, San Diego, CA, United States, July 2017

D. Erricolo, M.D. Poort, and P.L.E. Uslenghi, "Scattering by a Metallic Wedge Cylindrically Capped with Penetrable Materials", in *Asia Pacific Radio Science Conference*, Seoul, Korea, August 2016

M.D. Poort, V.G. Daniele, and P.L.E. Uslenghi, "Electromagnetic Scattering by an Array of Parallel Metallic Half-Planes Perpendicularly Truncated by a Metal Plane", in *URSI International Symposium on Electromagnetic Theory*, Espoo, Finland, August 2016

M.D. Poort and P.L.E. Uslenghi, "Electromagnetic Scattering by a Pair of Semi-infinite Parallel Plates Perpendicularly Truncated by a Metal Ground Plane", in *National Radio Science Meeting*, Boulder, CO, United States, January 2016